HYDROLOGIC REGIME DRIVES GREENHOUSE GAS EMISSIONS AND CROSS-ASSEMBLAGE CONVERGENCE OF SOIL PROTISTS AND PHOTOTROPHIC MICROBIOTA ALONG METHANE GRADIENTS IN CONSTRUCTED MINERAL-SOIL WETLANDS

by

Alexandra Haak

A thesis submitted in partial fulfilment of the

requirements for the degree of

Master of Science in Forestry

in the faculty of

Natural Resources Management

Committee Members:
Dr. I. Florin Pendea (Supervisor)
Dr. Nathan Basiliko (Committee Member)
Dr. Jian Wang (Committee Member)
Dr. Patrick Levasseur (External Examiner)

Abstract

Constructed wetlands are increasingly implemented as nature-based solutions for flood management, habitat creation, and climate mitigation. However, greenhouse gas (GHG) dynamics in these systems remain uncertain, particularly in mineral-soil wetlands where hydrologic conditions strongly influence carbon cycling processes. Understanding how hydrologic regime shapes greenhouse gas emissions and microbial community structure is therefore important for evaluating the climatic implications of wetland construction and management.

Greenhouse gas fluxes and soil microbiota were examined across three emergent-vegetation wetlands in southern Ontario, Canada, including two constructed wetlands established on mineral soils with contrasting hydrologic regimes—one permanently flooded and one seasonally flooded—and a natural comparison marsh developed on organic soil. Carbon dioxide (CO_2), methane (CH_4), and nitrous oxide (N_2O) fluxes were measured using static chambers over three years (2023–2025). Soil surface microbiota assemblages were characterized from samples containing heterotrophic protists - primarily testate amoebae - and phototrophic microorganisms including diatoms, green algae, and cyanobacteria.

Carbon dioxide fluxes exhibited strong seasonal patterns across all sites, increasing with temperature and peaking during summer months. In contrast, methane emissions were strongly structured by hydrologic regime. The permanently flooded constructed wetland exhibited sustained methane emissions throughout the year, including winter, whereas the seasonally flooded wetland maintained near-zero methane flux even during peak summer conditions. The natural comparison marsh showed intermediate methane emissions despite its organic substrate, reflecting shallower and more variable inundation. When expressed as CO_2-equivalent fluxes, methane accounted for most radiative forcing at the permanently flooded site but contributed minimally at the seasonally flooded site, indicating that hydroperiod exerts stronger control on climatic impact than wetland origin or substrate type.

Microbial community analyses revealed that heterotrophic protist and phototrophic microbiota assemblages were structured along shared environmental gradients. Co-inertia analysis indicated significant cross-assemblage coupling, suggesting that both groups respond to integrated hydrologic and biogeochemical conditions within the wetlands. The dominant community gradient was positively associated with methane flux, indicating that microbial community organization reflects ecosystem states linked to methane production and transport, whereas no comparable relationship was observed with carbon dioxide flux.

Together, the results demonstrate that hydrologic regime is a primary control on methane emissions and overall warming potential in mineral-soil constructed wetlands, while microbial community structure reflects underlying biogeochemical gradients associated with methane dynamics. These findings highlight the importance of hydroperiod in wetland design and management and contribute to understanding the climatic implications of constructed wetlands as nature-based solutions.

Keywords: hydrologic regime, greenhouse gas fluxes, methane (CH_4), constructed wetlands, mineral-soil wetlands, carbon dioxide (CO_2), nitrous oxide (N_2O), testate amoebae, diatoms, co-inertia analysis, soil surface microbiota, variation partitioning

Acknowledgements

First, I want to thank my supervisor, Dr. Florin Pendea. Without your unwavering trust in me, I would not have gained the experience and life skills completing this master's degree has given me. Thank you for your guidance, support and encouragement over the last two years.

I would also like to thank all volunteers and work-study students at Lakehead University who contributed their time in the field for sample collection and laboratory for processing the samples. Specifically thank you to Lily Edmunds, Evelyn McCloy, Samantha Mitchell, Hannah Stones, Brin Schat and Shaylyn Jordan. You all helped with not only field and lab work but in being true friends and emotional support through the ups and downs that is graduate work.

Thank you to Dr. Gail Chmura and the McGill University laboratory staff in particular Moshe (Mike) Dalva and Nathalie Tremblay for their assistance with processing gas samples. I thank my committee members Dr. Nathan Basiliko and Dr. Jian Wang for their feedback on the draft thesis manuscript.

Lastly, thank you to my family. My mom and dad for being true support systems and to my husband for believing in me and encouraging me to pursue graduate work.

I recognize that this project was funded through the Mitacs Accelerate program, Lake Simcoe Region Conservation Authority and the Ontario Graduate Scholarship.

I respectfully acknowledge that this research was conducted on lands that are the traditional territory of the Anishinaabeg peoples. The study areas located in Orillia, King Township, Innisfil, and Brock Township lie within the lands covered by the Williams Treaties and are closely connected to the territory of the Chippewas of Rama First Nation, Mississaugas of the Credit First Nation, Beausoleil First Nation, and Chippewas of Georgina Island First Nation. I recognize and respect the enduring relationships that Indigenous peoples have with these lands and waters, including the wetlands and ecosystems that form the focus of this research. I acknowledge the generations of stewardship and knowledge that have shaped these landscapes and am grateful for the opportunity to conduct research on these lands.

I acknowledge that this thesis presents original work and that no part of this thesis has been published or submitted for publication. Any ideas, techniques, or any other material from the work of other people included in my thesis, are cited in accordance with American Psychological Association 7th edition.

GenAi (ChatGPT, Claude, and Gemini) was used to summarize each manuscript to highlight the main findings for the combined abstract and conclusion, find repetitive or unclear sections, identify mistakes in grammar and references, and diagnose errors within R code.

Table of Contents

List of Tables

List of Figures

Figure 12. Plates of some testate amoebae, green algae and diatoms observed across sites. (1) *Trinema* spp. type (2) *Ditrema mikrous* (3) *Arcella discoides* type (4) *Arcella hemisphaerica* (5) *Paraquadrula irregularis* (6) *Staurastrum* spp. (7) Mesotaeniaceae (8) *Trochiscia reticularis* (9) *Cyphoderia ampull*a (10) *Hyalospenia elegans* (11) *Euglypha rotunda* (12) *Centropyxis aculeata* (13) *Euglypha spinosa* (14) *Galeripora catinus* (15) *Centropyxis cassis* (16) *Rhopalodia* spp. (diatom) (17) *Centropyxis discoides* (18) *Difflugia umbilicata.*

Figure 13. Statistical workflow used in Chapter 3. Community matrices were first transformed and analyzed using co-inertia analysis to quantify shared structure between heterotrophic protist and phototrophic assemblages. Compromise axes were then related to greenhouse gas fluxes to test functional relevance. Redundancy analysis and partial redundancy analysis were used to identify environmental gradients structuring each assemblage, while variation partitioning quantified the unique and shared contributions of dissolved gases, dissolved carbon/nitrogen pools, hydrologic variability, and site identity. Permutation tests and sensitivity analyses were used to evaluate robustness throughout the workflow.

Figure 14. Partial redundancy analysis (RDA) biplot of the heterotrophic protist assemblage, conditioned on site identity. Points represent taxa (top 20 by vector length labeled); arrows represent environmental predictor gradients (scaling 2). RDA1 and RDA2 explain 13.6% and 11.0% of constrained variation, respectively. Dissolved CH_4 and CO_2 project strongly along the primary axis, with large-bodied testate amoeba taxa (*Centropyxis platystoma*, *Difflugia difficilis ecornis*, *Phryganella acropodia*) oriented toward elevated dissolved gas conditions, and *Ditrema mikrous* and *Trinema* sp. in the opposing direction. DOC projects opposite to dissolved gases along RDA1, while DN and dissolved N_2O load on RDA2. Arrow direction and length indicate each predictor's correlation with the constrained axes — not its unique statistical contribution.

Figure 15. Partial redundancy analysis (RDA) biplot of the phototrophic assemblage, conditioned on site identity. Hydrologic predictors (water-table SD and water-table maximum) project prominently along the primary axis, with dissolved N_2O loading strongly on the secondary axis. *Pediastrum* and diatoms are associated with higher water-table conditions; *Microspora* sp. and *Tribonema* sp. orient in the opposing direction, and *Trochiscia reticularis* loads on the N_2O-associated secondary axis.

Figure 16. Four-way variation partitioning of the heterotrophic protist assemblage. Venn diagram shows adjusted R^2 fractions for dissolved gases (CH_4, CO_2, N_2O), dissolved carbon/nitrogen pools (DOC, DN), hydrologic variability (water-table SD), and site identity. Values < 0 not shown. Unique environmental fractions are uniformly small (dissolved gases: 0.00; DOC/DN: 0.01; WT variability: 0.02; nonsignificant at $p < 0.05$). The largest fractions are unique site (0.16) and shared environment × site intersections (dissolved gases × site = 0.09; dissolved gases × DOC/DN × site = 0.10). Residuals = 0.59.

Figure 17. Four-way variation partitioning of the phototrophic assemblage. Unique environmental fractions are larger and more evenly distributed than for the protist assemblage: dissolved gases = 0.07 ($p = 0.066$), WT variability = 0.07 ($p = 0.015$), DOC/DN = 0.04 ($p = 0.140$). Residuals = 0.68.

Figure 18. Relationship between the primary co-inertia compromise axis (CoI1) and atmospheric methane flux (growing season mean). Points are colored by site (CM = Cawthra Mulock, green;

CP = Circle Park, blue; CW = Beaver River, red). The line and shaded region show the linear regression fit ± 95% confidence interval. Spearman rank correlation confirmed a significant positive monotonic association ($\rho = 0.57$, $p = 0.005$). Note that CoI1 scores are derived entirely from community composition data via co-inertia analysis, independent of flux measurements, making this an unconstrained community–ecosystem association.

List of Abbreviations

BRW Beaver River Wetland

CM Cawthra Mulock

CO_2e Carbon dioxide–equivalent

CP Circle Park

CW Comparison wetland

DOC Dissolved organic carbon

DN Dissolved nitrogen

ECD Electron capture detector

FID Flame ionisation detector

GHG Greenhouse gas(es)

NbCS Nature-based climate solution

PVC Polyvinyl chloride

RDA Redundancy analysis

SD Standard deviation

SE Standard error

SFGWP Sustained flux-weighted global warming potential

VIF Variance inflation factor

WT Water table

CHAPTER 1: THESIS INTRODUCTION

1.1 Wetlands in the Global Carbon Cycle

The global carbon cycle operates through fluxes of carbon among reservoirs such as the atmosphere, oceans, wetlands, soils, and plants that are controlled by a series of mechanisms, including photosynthesis, respiration, organic matter decomposition, weathering, sedimentation, volcanic activity, and anthropogenic activities (U.S. Department of Energy, 1985; Sundquist et al., 2009). Wetlands are a major pool of carbon that hold about one third of terrestrial soil carbon due to the saturated conditions that slow the decomposition of organic material by anaerobic soil microbes (Keller, 2011; Schuster et al., 2024). However, anaerobic microbial processes also make wetlands a source of nitrous oxide and one of the world's largest natural sources of methane (Keller, 2011; Ma et al., 2024; Schuster et al., 2024). On a 100-year time scale, methane and nitrous oxide have a radiative force 27 and 273 times higher than carbon dioxide, respectively (Muñoz et al., 2024). Between the sequestration of carbon and source of other greenhouse gases, wetlands are an important factor in the global carbon cycle.

1.2 Biogeochemical Pathways of Greenhouse Gas Fluxes in Wetlands

Greenhouse gas fluxes are controlled by many pathways within wetlands. Soil environments and properties strongly influence the capacity of wetlands to store carbon and regulate greenhouse gas production. Carbon stocks are typically concentrated in surface soils for mineral-soil wetlands, particularly within the upper 15 cm of the soil profile where organic inputs and microbial activity are greatest and can be meters deep for peatlands because of the large accumulation of organic peat (Tangen et al., 2020; Poulter et al., 2021). The production and decomposition of this organic matter strongly influence greenhouse gas dynamics. Carbon dioxide (CO_2) fluxes in wetlands are controlled by the balance between photosynthetic carbon

uptake and microbial respiration. Plants and algae assimilate atmospheric CO_2 through photosynthesis, storing carbon in plant biomass and soils and microbial decomposition of organic matter releases CO_2 through aerobic respiration and anerobic processes depending on redox conditions where soils become more oxygenated during periods of lower water levels or oxygen levels decrease due to prolonged high-water levels, respectively (Hassett et al., 2024; Mitsch et al., 2013; Paul & Frey, 2023, pp. 34).

Vegetation strongly influences carbon cycling in wetlands by contributing organic inputs and regulating soil conditions. Carbon enters soils through root growth, root exudates, and the decomposition of plant litter (Berhongaray et al., 2019; Forfora et al., 2024). Below-ground biomass can contribute substantially to soil carbon storage, with approximately 76% of below-ground biomass converted to soil carbon compared to only 9% of above-ground biomass (Berhongaray et al., 2019). Vegetation also affects methane dynamics by modifying oxygen availability and gas transport pathways (Bansal et al., 2020).

Methanogenesis is an anaerobic microbial process that occurs in waterlogged sediments where oxygen is limited (Boon & Mitchell, 1995). Some methane may be oxidized by methanotrophic bacteria in oxygenated surface soils before reaching the atmosphere (Segers, 1998). Methane can be emitted through diffusion, ebullition, or plant-mediated transport through vascular plant tissues (Bridgham et al., 2013). Plant species can influence methane emissions by altering rhizosphere oxygen conditions and providing pathways for gas movement. For example, dense stands of *Phragmites australis* have been shown to reduce methane emissions relative to unvegetated areas, partly due to internal plant ventilation that transports oxygen to root zones (Dušek et al., 2023). Differences in methane flux among plant species are often linked to variations in root morphology and rhizosphere processes (Villa et al., 2020).

Nitrous oxide (N_2O) production in wetlands is primarily associated with microbial nitrogen cycling. Nitrification occurs under oxygenated conditions when ammonium is oxidized to nitrate, producing N_2O as a by-product (Butterbach-Bahl et al., 2013). Denitrification occurs under anaerobic conditions when nitrate is reduced to dinitrogen gas, although incomplete, denitrification can release N_2O (Reay et al., 2018; Van Cleemput et al., 2007). Since these processes require both aerobic and anaerobic environments, N_2O emissions often occur in zones where water tables fluctuate and redox conditions vary (Schuster et al., 2024).

Hydrology is a primary control on greenhouse gas production and emissions in wetlands because it regulates oxygen availability and microbial activity (Creed et al., 2013; Mander et al., 2010; Pennock et al., 2010). Permanent inundation promotes anaerobic conditions that favor methane production, while drying soils increase oxygen availability and stimulate CO_2 production through aerobic respiration. Water table fluctuations can also increase N_2O emissions by creating alternating aerobic and anaerobic conditions that support both nitrification and denitrification (Pennock et al., 2010).

1.3 Constructing Wetlands as Nature-based Climate Solutions

Wetlands are increasingly being constructed as nature-based solutions for water management, ecological restoration, and climate mitigation. Wetlands provide multiple ecosystem services that contribute to climate change mitigation. In addition to storing carbon, they help regulate hydrology by reducing flood and storm impacts, support biodiversity, remove pollutants, and improve water and air quality (Barman et al., 2024). Protecting existing wetlands therefore represents a major opportunity for climate mitigation. Drever et al. (2021) estimated that avoiding peatland disturbance and preventing the conversion of freshwater mineral soil wetlands could offset approximately 2.2–29.7 Tg CO_2e yr^{-1} and 0.5–5.7 Tg CO_2e yr^{-1}, respectively,

representing emissions equivalent to millions of Canadian households. Given natural wetlands have accumulated carbon over long timescales, they can exert a substantial radiative cooling effect, further emphasizing the importance of wetland conservation (Schuster et al., 2024). Although natural wetlands represent long-established carbon sinks, restored and constructed wetlands can also contribute to carbon sequestration efforts. Evidence suggests that restored wetlands can begin reducing net greenhouse forcing relatively quickly, while their greatest cooling benefits occur over longer timescales as soils and ecological processes develop (Ma et al., 2024; Schuster et al., 2024). However, important differences remain between natural and constructed wetlands. Natural wetlands have typically accumulated organic soils and stable microbial communities, whereas constructed wetlands often begin with mineral substrates and relatively undeveloped microbial communities (Bruland & Richardson, 2006; Ansola et al., 2014). These differences create uncertainty regarding greenhouse gas dynamics in constructed wetlands. While wetlands are recognized as one of the largest natural sources of methane, it remains unclear whether carbon sequestration in constructed wetlands consistently offsets methane emissions at ecosystem scales (Reay et al., 2018; Van Amstel, 2012; Ma et al., 2024). This uncertainty is especially pronounced for temperate mineral-soil wetlands.

1.4 Microbial Communities as Bioindicators

Microbial communities, specifically testate amoebae and diatoms, green algae, cyanobacteria, and xanthophytes respectively, are well known bioindicators of environmental conditions (Wanner et al., 2020). The morphology of testate amoebae's test (shell) composition, formation, size, aperture shape and position can all indicate different environmental factors (Silva et al., 2022). Their short lifespan allows them to respond quickly to changes in the environment (Silva et al., 2022). A recent study assessing testate amoebae as bioindicators in freshwater systems

showed that these organisms can distinguish river order, lentic and lotic environments with specific chemical, physical, and biological conditions based on what species are present (Bredariol et al., 2026).

Along with being drivers for biogeochemical cycling within freshwater systems, phototrophic microbiota like diatoms, green algae, cyanobacteria, and xanthophytes are also strong bioindicators. Diatoms have been used to detect changes in pH, organic pollution, and salinity (Astuti et al., 2026; Frau & Pineda, 2024). Green algae and cyanobacteria respond to the increased availability of nitrogen and phosphorus while xanthophytes are found in shallow, low-nutrient environments (Bellinger & Sigee, 2015; Wallace et al., 2015). Whether heterotrophic protists and phototrophic microbiota can serve as bioindicators of greenhouse gas gradients and environmental drivers in mineral-soil constructed ecosystems remains inadequately constrained.

1.5 Knowledge Gaps

Research on wetlands as nature-based climate solutions (NbCS) focuses predominantly on peatlands. Schuster et al. (2024) found that approximately 76% of studies examining the climate mitigation potential of freshwater wetlands have focused on peatlands, leaving a significant knowledge gap regarding mineral soil wetlands. Moreover, most mineral soil wetland literature focuses on restored wetlands rather than constructed. Current literature shows mineral soil wetlands are mainly constructed for wastewater treatment in municipal settings, agricultural and stormwater runoff (Ingrao et al., 2020; Zhi, W., & Ji, G. 2012). In these systems, GHG emissions can be 2–10 times higher than in natural wetlands, driven by elevated substrate availability and redox fluctuations associated with pollutant loading compounding this uncertainty on constructing wetlands as NbCS (Mander et al., 2014). Furthermore, the coupling between microbiota, greenhouse gas emissions and environmental drivers in constructed wetlands is also

lacking when it comes to NbCS. As microbiota, especially protists like testate amoebae, can be strong bioindicators, research on their correlation to greenhouse gas emissions and environmental drivers like hydrologic regime and soil temperature in these systems needs to be further explored (Bredariol et al., 2026).

1.6 Research Objectives and Questions

As constructed wetlands become more attractive as nature-based climate solutions, the main questions this research aims to answer are: (a) what environmental drivers (hydrologic regime, soil temperature, and water depth) influence CO_2, CH_4, and N_2O fluxes in constructed mineral soil wetlands? b) what is the integrated climatic forcing of these wetlands? and c) do heterotrophic protist and phototrophic microbial communities correspond with environmental conditions and methane, carbon dioxide, and nitrous oxide fluxes in mineral soil constructed wetlands?

1.6.1 Chapter 2 Constructed Mineral Soil Wetland Greenhouse Gas Emissions

To answer questions a and b, this thesis aims to address the following objectives:

- quantify seasonal and interannual variability in CO_2, CH_4, and N_2O fluxes across wetlands;
- assess how hydrologic regime influences individual gas fluxes and integrated climatic forcing; and
- evaluate the extent to which environmental drivers—particularly soil temperature and water depth—explain observed variability in greenhouse gas exchange.

By explicitly separating hydrologic controls from wetland origin and substrate type, this study provides a process-based assessment of the climatic performance of habitat-oriented constructed mineral-soil wetlands and informs their design and management as NbCS in temperate regions.

1.6.2 Chapter 3 Protists and Phototrophic Microbiota Correlation to Greenhouse Gas Flux and Environmental Drivers

To answer question c, the objectives of this study were to:

- quantify environmental structuring of heterotrophic protist and phototroph-dominated microbial assemblages using partial redundancy analysis conditioned on wetland type;
- assess cross-assemblage coupling using co-inertia analysis; and
- test whether shared community gradients align with atmospheric methane, carbon dioxide, and nitrous oxide fluxes.

CHAPTER 2: HYDROLOGIC REGIME CONTROLS GREENHOUSE GAS EMISSIONS IN CONSTRUCTED MINERAL-SOIL WETLANDS DOMINATED BY EMERGENT VEGETATION

2.1 Introduction

Wetlands occupy a paradoxical position in the global carbon cycle. They rank among the most effective ecosystems for long-term carbon sequestration, yet they are also the single largest natural source of atmospheric methane (CH_4), a potent greenhouse gas with strong short-term radiative forcing (Reay et al., 2018; Van Amstel, 2012). The net climatic role of any wetland therefore depends on the balance among carbon dioxide (CO_2) uptake and release, CH_4 emissions, and, to a lesser extent, nitrous oxide (N_2O) fluxes (Ma et al., 2024; Schuster et al., 2024). Understanding how this balance varies across wetland types, hydrologic regimes, and stages of development is central to evaluating wetlands as nature-based climate solutions (NbCS), particularly in temperate systems increasingly targeted for construction and restoration.

In Canada, extensive wetland loss driven by urbanization and agricultural conversion has reduced ecosystem carbon stocks and diminished a suite of ecosystem services including flood attenuation, water quality improvement, and biodiversity support (Creed et al., 2022; Trettin et al., 2020). Recent national assessments suggest that avoiding further wetland conversion and restoring degraded systems could contribute substantially to climate mitigation targets, while also delivering hydrologic and ecological co-benefits (Drever et al., 2021). However, much of the existing literature on wetland climate forcing centers on peatlands, which differ fundamentally from mineral-soil wetlands in carbon stocks, vegetation, microbial community composition, and hydrologic controls (Schuster et al., 2024; Ma et al., 2024). As a result, the greenhouse gas dynamics of constructed and restored mineral-soil wetlands—particularly those embedded in managed or urbanizing landscapes—remain poorly constrained. Constructed mineral-soil wetlands often differ from natural systems in their soil development, hydrologic design, and microbial community structure, which may influence greenhouse gas fluxes during early stages of ecosystem development (Nahlik & Mitsch, 2010; Ma et al., 2024).

Hydrology is widely recognized as a first-order control on wetland greenhouse gas fluxes (Creed et al., 2013; Mander et al., 2011; Pennock et al., 2010). Differences in water level management, substrate type, and vegetation establishment may therefore lead to contrasting greenhouse gas fluxes among constructed wetlands and nearby natural comparison systems (Dušek et al., 2023; Schuster et al., 2024; Pennock et al., 2010; Tangen & Bansal, 2020).

Few studies address constructed wetlands designed for habitat creation, stormwater management, or ecological restoration—systems that more closely resemble natural wetlands in their nutrient regime and organic matter dynamics but that differ in soil development, microtopography, and hydrologic design. This distinction is critical because the GHG performance of habitat-oriented

constructed wetlands on mineral soils cannot be reliably inferred from either the wastewater treatment wetland literature or the peatland literature. Moreover, few studies directly compare constructed wetlands with contrasting hydrologic designs against nearby natural comparison systems sharing similar vegetation, using multi-year measurements that capture both seasonal and interannual variability. Such comparisons are necessary to disentangle the effects of hydrologic regime from those of wetland origin and substrate type on greenhouse gas fluxes.

Here, we evaluate greenhouse gas fluxes (CO_2, CH_4, and N_2O) from two constructed mineral-soil wetlands with contrasting hydrologic regimes—a permanently flooded system and a seasonally flooded system—and a natural comparison marsh with organic soil, all within the Lake Simcoe watershed, Ontario, Canada. All three sites are dominated by *Typha latifolia*. The inclusion of a natural organic-soil comparison site alongside two constructed mineral-soil sites provides a framework for assessing the relative importance of hydrologic regime versus both wetland origin and substrate type. Because each hydrologic regime is represented by a single wetland, this study constitutes an unreplicated natural experiment in which site identity, hydrologic design, and substrate type are inherently confounded (sensu Oksanen, 2001). Mechanistic inferences therefore rest not on formal factorial hypothesis testing but on the convergence of multiple lines of evidence, including multi-year consistency, within-site environmental regressions, and diurnal patterns. The natural comparison site (BRW) provides ecological context for interpreting constructed wetland performance, though it differs from the constructed sites in both substrate and hydrologic regulation and therefore does not serve as an experimental control in the strict sense.

2.2 Materials and Methods

2.2.1 Study Sites

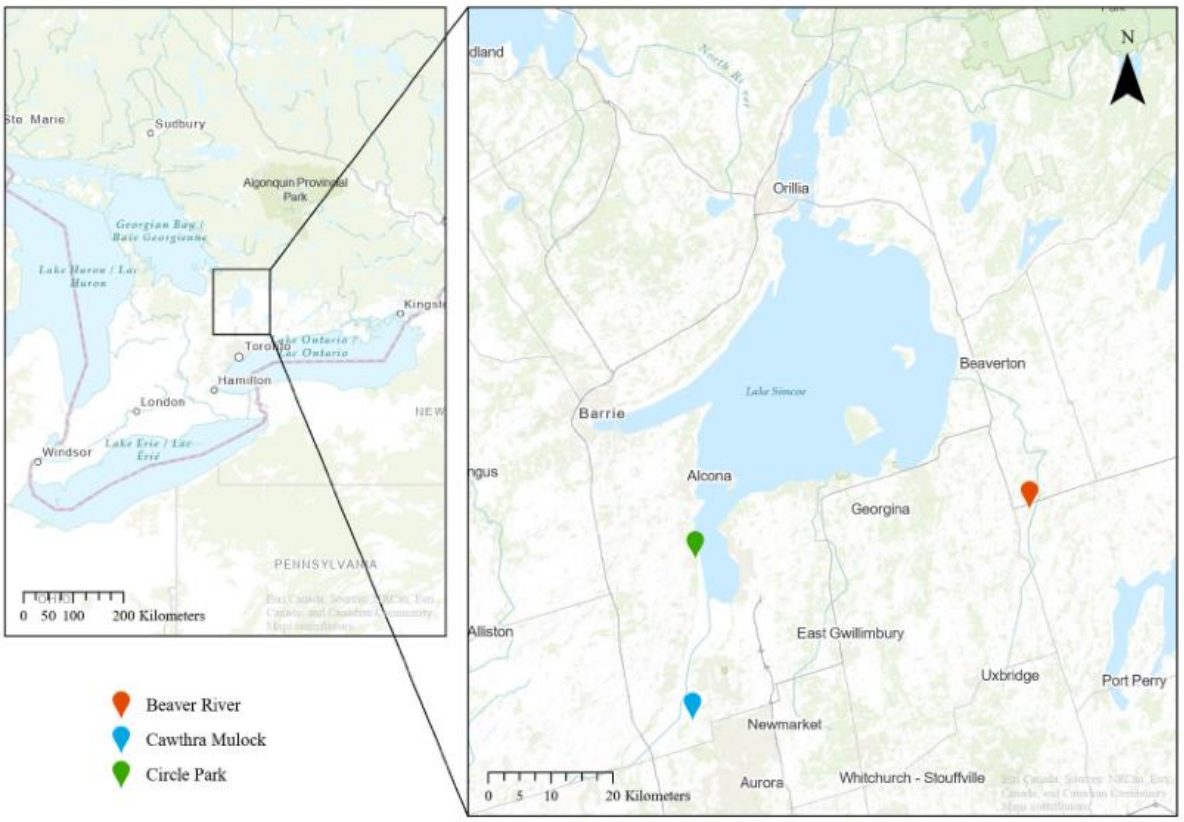

Figure 1. Circle Park (CP; constructed, permanently flooded), Cawthra Mulock (CM; constructed, seasonally flooded), and Beaver River Wetland (BRW; natural, permanently flooded) within Ontario, Canada.

All study sites are located in the southern region of Ontario, Canada (Figure 1), within a humid continental climate (Köppen *Dfb*) characterized by warm summers, cold winters, and year-round precipitation moderated by the proximity of the Great Lakes. The region is underlain by Paleozoic sedimentary bedrock, predominantly limestone. Two constructed wetlands on mineral soils and one natural wetland on organic soil were selected to represent contrasting hydrologic regimes and substrate types under similar vegetation cover, with *Typha latifolia* dominating all three sites.

Circle Park (CP) is a 1.5-ha constructed wetland in the Township of Innisfil (Gilford), Ontario, approximately 200 m west of Lake Simcoe. Created in 2021 as part of an urban park

development, CP is permanently flooded and dominated by cattail (*Typha latifolia*), with some areas of open water. The wetland is developed on mineral soil and is designed as a stormwater management and habitat feature. Native trees and shrubs have been recently planted in the adjacent upland. Cawthra Mulock (CM) is a 107-ha nature reserve in King Township that features a diversity of habitats including swamp and non-native meadow. Within the reserve, several basins (ranging from approximately 150 m^2 to over 3,000 m^2) were excavated in mineral soil and subsequently flooded. The study basins are seasonally flooded and colonized by cattails (*Typha latifolia*) along with a mix of invasive and ruderal species. The Beaver River Wetland (BRW) is a natural permanently flooded marsh dominated by *Typha latifolia*, situated within the floodplain of the Beaver River—a slow-flowing, meandering, and shallow (predominantly ≤1 m deep) system. BRW has developed on organic soil with approximately 37% organic carbon, consistent with long-term organic matter accumulation in a natural floodplain marsh, though lower in organic content than typical peatlands (>40 cm surface organic matter; Ma et al., 2024). Although permanently inundated, water depths at BRW vary more widely over the growing season in response to river stage and precipitation and are generally shallower than at CP.

2.2.2 Field Methods

Greenhouse gas fluxes were measured using a dark, static chamber method (Magenheimer et al., 1996; Chmura et al., 2016). Chambers were constructed from 50-L acrylic cylinders (27 cm diameter) wrapped in aluminum foil to insulate and block sunlight. Where cattails exceeded the chamber height, a second chamber was fitted on top using an airtight acrylic connector, yielding a total volume of 100 L. Chambers were sealed at the top with an acrylic platform equipped with a Bev-a-Line sampling tube, a one-way copper pressure-relief vent (“pigtail”), and a 12-V battery-powered fan mounted inside to mix headspace air during sampling. Internal air

temperature was logged with a HOBO Temperature Data Logger (Onset, Bourne, Massachusetts, USA).

Chambers were placed onto PVC collars inserted 2.5 cm into the marsh soil at least two weeks prior to gas sampling. A 0.5-cm groove in the collar rim, filled with water, ensured an airtight seal. A 25-mL gas sample was drawn with a syringe fitted with a Luer lock and two-way stopcock, then expelled into a pre-evacuated exetainer (Labco, UK). Samples were collected at 0, 20, 40, and 60 minutes.

Chamber placement followed a randomized design constrained along transects established within each site. Positions along transects from minimum to maximum water table depth were selected randomly while maintaining a minimum spacing of 2 m between chambers to reduce spatial dependence. At Circle Park, this approach was combined with stratified random placement across vegetated and open water surfaces. We placed eleven chambers at CM, nine at CP, and four at BRW. The lower replication at BRW reflects logistical constraints on site access; site-level estimates for BRW consequently carry greater uncertainty and this imbalance is considered in the interpretation of inferential results. Seasonal sampling campaigns were conducted during winter (February), spring (April), summer (July), and fall (October) in 2023 and 2024. In 2025, sampling frequency increased to monthly measurements from February through October to better resolve growing-season dynamics. A diurnal campaign (measurements at 08:00, 16:00, and 00:00) was conducted in July 2025 at four representative chambers per site.

Environmental measurements were recorded within 1 m of each collar after the final gas sample. Soil temperature was measured at 15 cm depth using a soil thermometer inserted vertically. At flooded sites this depth was below standing water, whereas at CM during seasonal drawdown it was within aerated soil. Water table gauges were inserted near each collar to measure water table

depth at the time of sampling. Average daily air temperatures were obtained from Environment Canada meteorological stations at Barrie and Newmarket. Water samples for dissolved organic carbon (DOC) and dissolved nitrogen (DN) were collected at each collar location during each seasonal campaign, but these data will be presented in a companion manuscript focusing on dissolved gases and nutrients.

2.2.3 Laboratory Methods

2.2.3.1 Gas Concentration and Flux Analysis

Gas samples were analyzed on a gas chromatograph (GC-14, Shimadzu, Kyoto, Japan) fitted with a methanizer to convert CO_2 to CH_4, a flame ionization detector (FID) for CH_4, and an electron capture detector (ECD) for N_2O. The FID operated at 250°C and the ECD at 325°C. Standards of N_2O (21.9 ppm), CH_4 (5.1 ppm), and CO_2 (5,000 ppm) yielded accuracies and precisions of ±0.3 ppm, ±0.4 ppm, and ±78 ppm, respectively. Headspace gas concentrations were converted to mass fluxes (mg m^{-2} h^{-1}) using the ideal gas law, chamber volume, and incubation time.

Because chambers were opaque, measured CO_2 fluxes represent ecosystem respiration (ER) rather than net ecosystem CO_2 exchange. As such, fluxes were calculated primarily from linear regressions of CO_2 concentration against time. Linear fits were accepted when the coefficient of determination for CO_2 exceeded 0.7 ($R^2 \geq 0.70$), the only gas where linear fits are expected. When linear fits did not meet acceptance criteria, but concentration changes were directionally consistent, alternate flux estimates based on the difference between initial and final headspace concentrations (T_{60}–T_0) were used to minimize data loss. Of the total flux measurements, approximately 56% were estimated using the linear regression method and 34 % using the T_{60}–T_0

method. Approximately 8% of measurements had an $R^2 \geq 0.30$ representing chambers where the CO_2 flux decreased from T_0 to T_{60} or was strongly non-linear; these were excluded from the analysis. Fluxes not significantly different from zero were retained for descriptive analyses but were considered less robust when drawing conclusions.

2.2.3.2 Calculation of CO_2-Equivalent Fluxes

To evaluate the relative climatic influence of measured greenhouse gas fluxes, annual mean fluxes of CO_2, CH_4, and N_2O were converted to carbon dioxide–equivalent (CO_2e) fluxes using 100-year sustained-flux global warming potentials (SFGWP) principles following Neubauer and Megonigal (2015), but with radiative efficiency values (GWP_{100}) from the IPCC Sixth Assessment Report (IPCC, 2021). The GWP_{100} values applied were: $CH_4 = 27.2$ and $N_2O = 273$; CO_2 was assigned a GWP of 1.

For each site and year, integrated CO_2-equivalent flux was calculated as:

$$CO_2e\ flux\ (mg\ m^{-2}\ h^{-1}) = F_{CO_2} + (27.2 \times F_{CH_4}) + (273 \times F_{N_2O})$$

where F_{CO_2}, F_{CH_4}, and F_{N_2O} represent annual mean fluxes (mg m^{-2} h^{-1}) for each gas. This formulation expresses the combined radiative forcing of measured gaseous fluxes (ER + CH_4 + N_2O) as an instantaneous CO_2-equivalent flux per unit area.

2.2.4 Data Analyses

Greenhouse gas fluxes were analyzed at multiple temporal scales to account for differences in sampling frequency among years. Descriptive statistics, including arithmetic means and standard deviations, were calculated for all fluxes and are reported in mg m^{-2} h^{-1}.

For interannual comparisons, data from 2023, 2024 and 2025 were summarized using seasonal averages based on matched sampling periods (February, April, July, and October). This data was used to evaluate broad interannual patterns and site-level contrasts but were not subjected to formal inferential statistics due to limited temporal resolution.

Statistical analyses were conducted primarily on the 2025 dataset, which comprised eight sampling events in February and April through October. Linear mixed-effects models were used to evaluate the effects of site and sampling period (fixed effects) on greenhouse gas fluxes, with chamber identity as a random intercept to account for repeated measurements. Environmental controls on fluxes were assessed using mixed-effects regression models relating fluxes to soil temperature and water depth, evaluated individually and in combination. Model residuals were inspected visually (residuals versus fitted values and normal Q–Q plots) to confirm approximate normality and homoscedasticity; no major violations were detected.

Due to the episodic and low-magnitude nature of N_2O fluxes, statistical inference for this gas was interpreted cautiously, emphasizing descriptive patterns over predictive relationships. All analyses and visualizations were performed in R with packages readxl, janitor, dplyr, stringr, forcats, lme4, lmerTest, broom.mixed, performance, readr, MASS, tidyr, tibble, ggplot2, vegan, openxlsx, permute, ade4, grid.

2.3 Results

2.3.1 Environmental Conditions and Hydrologic Variability

Soil temperature followed expected temperate seasonal cycles across all three sites, with rapid warming through spring, peak temperatures in July–August, and cooling into fall (Figure 2).

Seasonal temperature patterns were broadly similar among sites, with slight differences in absolute values reflecting variation in inundation depth and exposure.

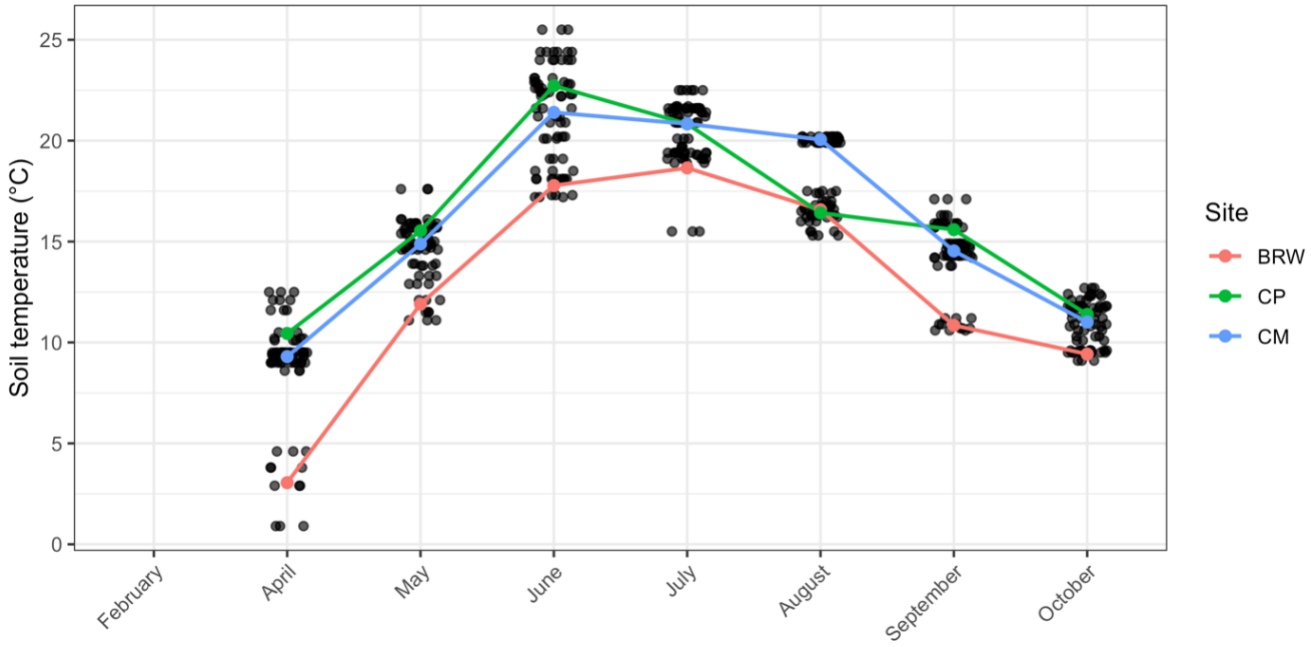

Figure 2. Seasonal soil temperature variation across two constructed wetlands (Circle Park—CP and Cawthra Mulock—CM) and a natural comparison site (Beaver River Wetlands—BRW). From July 2023 to February 2025, soil temperature measurements were taken seasonally in April, July, and October. In 2025, measurements were taken monthly from April through October.

Hydrologic conditions differed markedly among sites but were consistent with site design (Figure 3). Circle Park (CP), the permanently flooded constructed wetland, maintained water levels above the soil surface throughout the study period with relatively small seasonal fluctuations. The Beaver River Wetland (BRW) was also permanently inundated, though water depths varied more widely in response to river stage and precipitation, and were generally shallower than at CP.

In contrast, Cawthra Mulock (CM) experienced pronounced drawdown following spring inundation. Water levels were typically highest in spring and declined rapidly during late spring and summer, frequently falling below the soil surface for much of the growing season. This hydrologic divergence between CP and CM was consistent across all three years, providing a

robust contrast between permanently and seasonally flooded conditions. Interannual differences in hydrologic conditions were present but secondary to site-level contrasts; while the timing and magnitude of peak water levels varied among years, relative differences among sites were preserved.

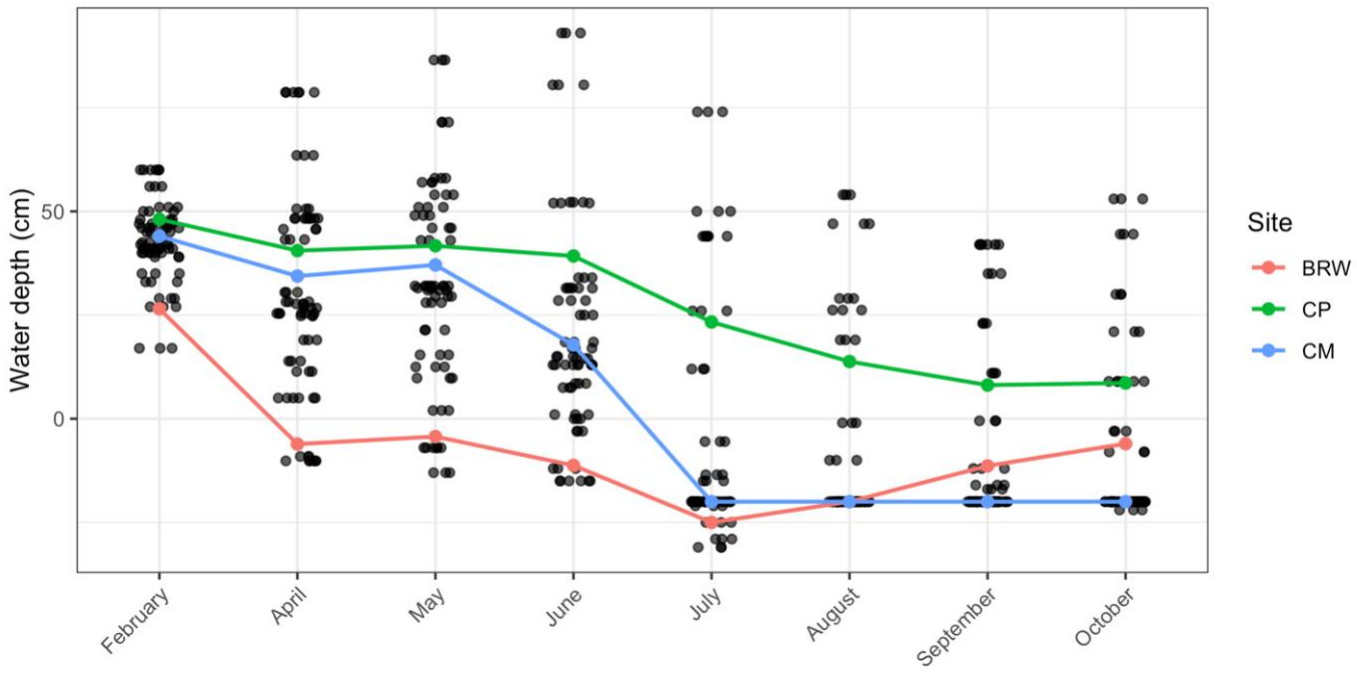

Figure 3. Water depth variation across growing seasons (2023–2025) for two constructed wetlands (Circle Park—CP and Cawthra Mulock—CM) and a natural comparison site (Beaver River Wetlands—BRW). February values represent snowpack thickness above the surface, not water table measurements. From July 2023 to February 2025, measurements were taken seasonally in April, July, and October. In 2025, measurements were taken monthly from April through October.

2.3.2 Site-Specific Seasonal Greenhouse Gas Fluxes (2025)

Monthly sampling in 2025 revealed pronounced site-specific seasonal trajectories for CO_2, CH_4, and N_2O (Figure 4–6). The following subsections describe these patterns for each site.

2.3.2.1 Circle Park (CP; Permanently Flooded Constructed Wetland)

CO_2 fluxes at CP increased steadily from winter into early summer (Figure 4). Mean fluxes rose from 29.3 ± 16.2 mg m^{-2} h^{-1} in February to 229.7 ± 127.8 in May, reaching a peak in June (845.7

± 860.6). Fluxes remained elevated through mid-summer (July: 642.8 ± 207.2; August: 550.8 ± 286.9) before declining into fall (October: 266.1 ± 153.9). Large standard deviations during summer reflect substantial spatial variability under peak biological activity.

CH_4 fluxes at CP exhibited the strongest seasonal amplitude observed across all sites and gases (Figure 4). Winter and early spring fluxes were low but positive (February: 2.33 ± 1.92; April: 1.73 ± 10.47), increasing markedly in late spring (May: 14.2 ± 11.2) and peaking in June (135.4 ± 139.7). Fluxes remained positive but highly variable through summer and early fall (July: 56.9 ± 55.1; September: 55.4 ± 83.2), declining in late summer and fall (August: 6.95 ± 34.1; October: 14.0 ± 17.3). This pattern indicates sustained methane production under permanently flooded conditions, including outside the peak growing season.

N_2O fluxes at CP were consistently small and clustered near zero throughout the year (Figure 4), with values ranging from −0.021 ± 0.023 (July) to 0.005 ± 0.029 (April).

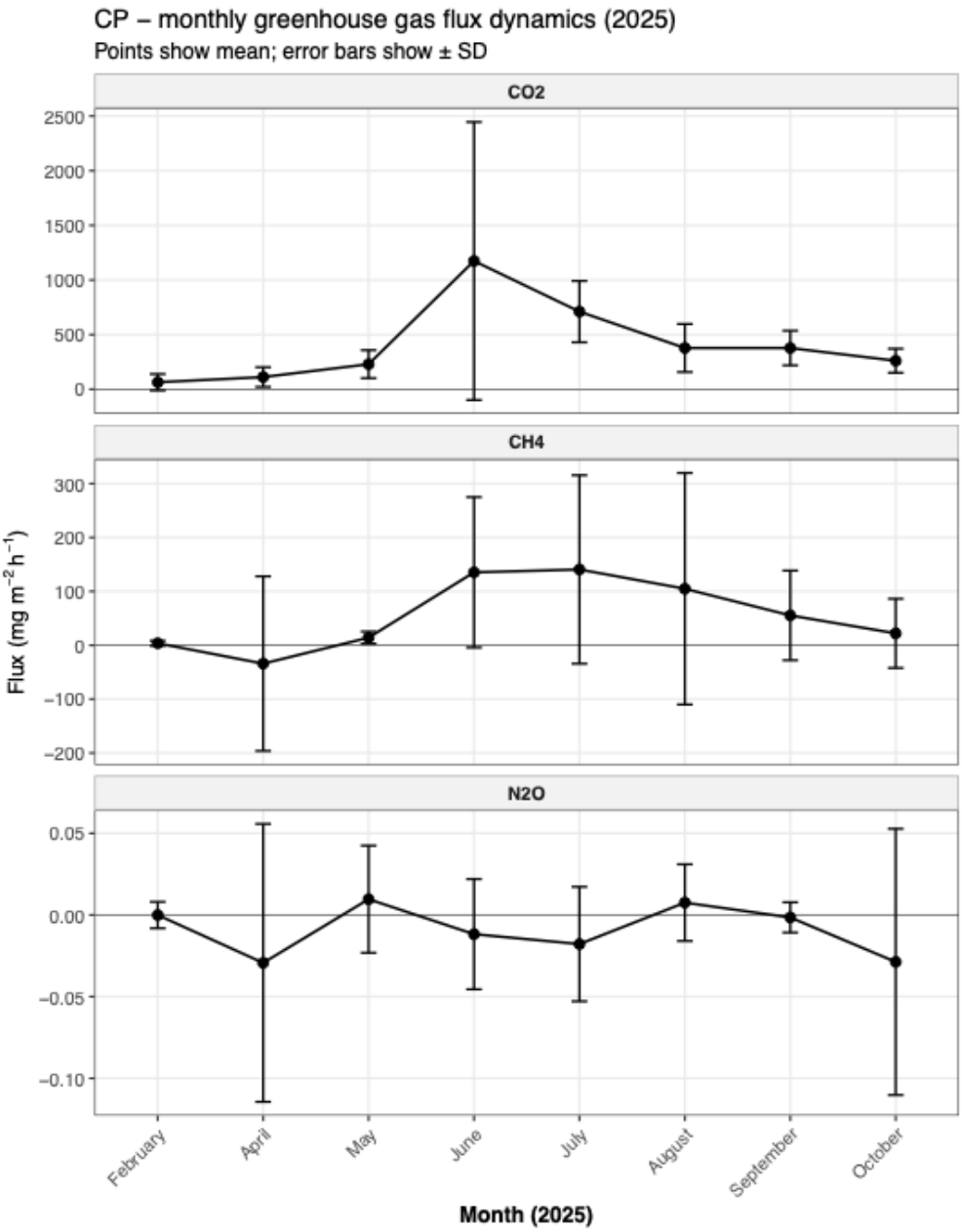

Figure 4. Monthly greenhouse gas fluxes at Circle Park (CP), a permanently flooded constructed wetland, during 2025. Points and lines represent monthly mean fluxes (mg m^{-2} h^{-1}) for CO_2, CH_4, and N_2O, with error bars showing ±1 SD.

2.3.2.2 Cawthra Mulock (CM; Seasonally Flooded Constructed Wetland)

CO_2 fluxes at CM followed a pronounced seasonal cycle (Figure 5). Mean winter fluxes were low (February: 13.1 ± 19.8), increased through spring (May: 249.7 ± 148.8), and peaked in July (951.7 ± 453.4). Elevated fluxes persisted in June (604.2 ± 300.2) and August (649.6 ± 394.5) before declining into fall. The large within-season variability is consistent with fluctuating soil moisture during seasonal drawdown.

In marked contrast to CP, CH_4 fluxes at CM remained strongly suppressed throughout the year (Figure 5). Mean fluxes were near zero from winter through spring (February: 0.27 ± 0.37; April: 0.49 ± 1.80; May: 0.67 ± 0.85). The highest monthly mean occurred in June (3.46 ± 2.67), but CH_4 fluxes otherwise remained negligible during summer (July: 0.31 ± 0.45) and early fall (September: 0.04 ± 0.11), turning slightly negative in October (−0.058 ± 0.113).

N_2O fluxes at CM were low and variable, with mean values near zero across most months (Figure 5). Summer and fall values remained small and showed no consistent temporal pattern.

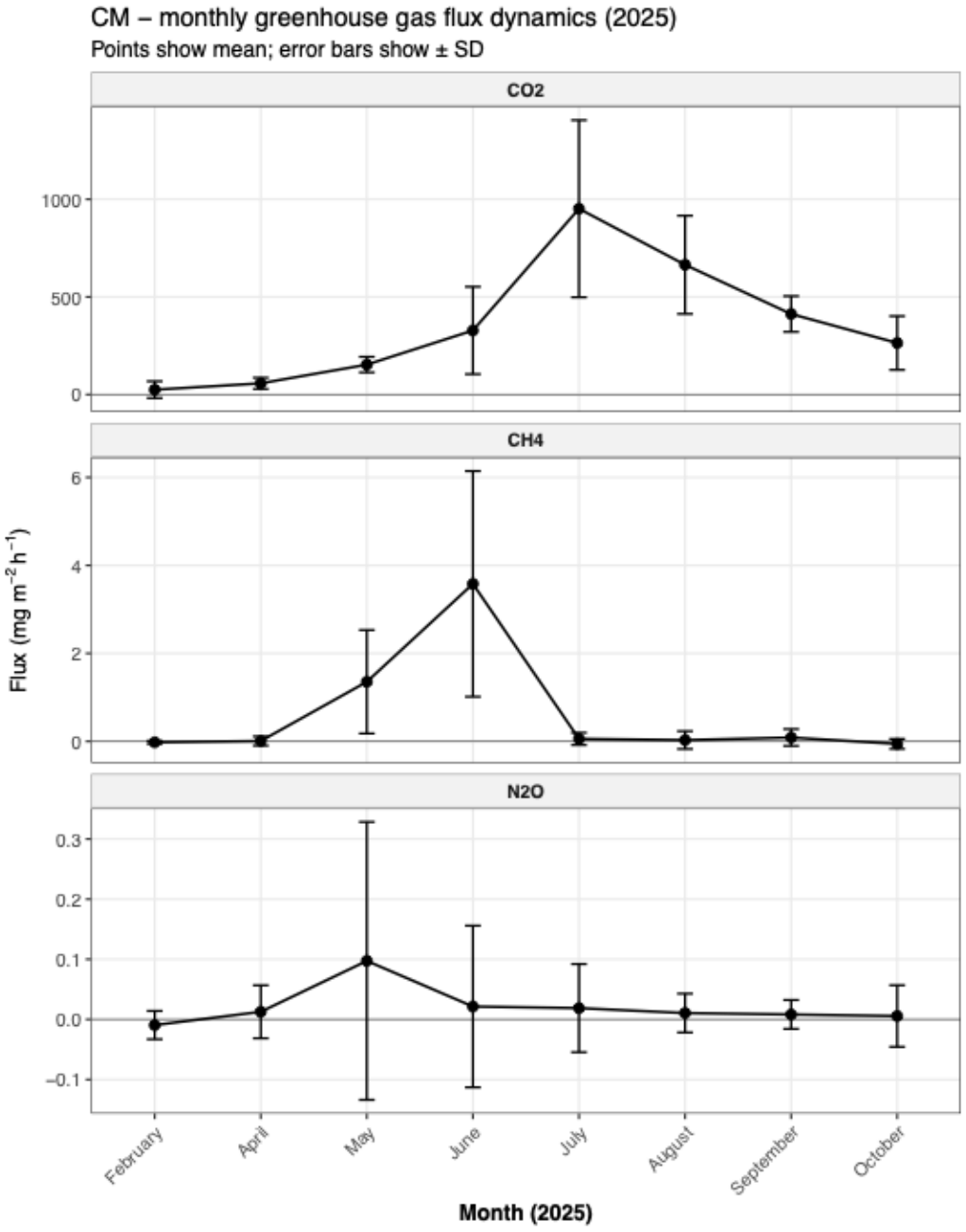

Figure 5. Monthly greenhouse gas fluxes at Cawthra Mulock (CM), a seasonally flooded constructed wetland, during 2025. Monthly mean fluxes (mg m^{-2} h^{-1}) ±1 SD are shown for CO_2, CH_4, and N_2O.

2.3.2.3 Beaver River Wetland (BRW; Natural Comparison Marsh)

CO_2 fluxes at BRW followed a strong seasonal trajectory similar to CM (Figure 6), with low winter values (February: 3.91 ± 3.86) increasing through spring (May: 316.7 ± 191.7) and peaking in July (826.4 ± 375.5). Fluxes declined sharply into fall (October: 80.3 ± 53.2).

CH_4 fluxes at BRW were consistently positive but low in magnitude relative to CP (Figure 6). The highest mean occurred in June (2.03 ± 3.16), followed by modest fluxes through summer (July: 1.40 ± 1.36; August: 0.61 ± 0.67) and near-zero values in fall. Despite permanent inundation and organic-rich substrate (~37% OC), CH_4 emissions at BRW were substantially lower than at CP, consistent with the shallower and more variable water depths at the natural site.

N_2O fluxes at BRW showed episodic behavior, with a relatively elevated mean in May (0.052 ± 0.105) compared with other months (Figure 6). Outside this period, mean N_2O fluxes remained close to zero.

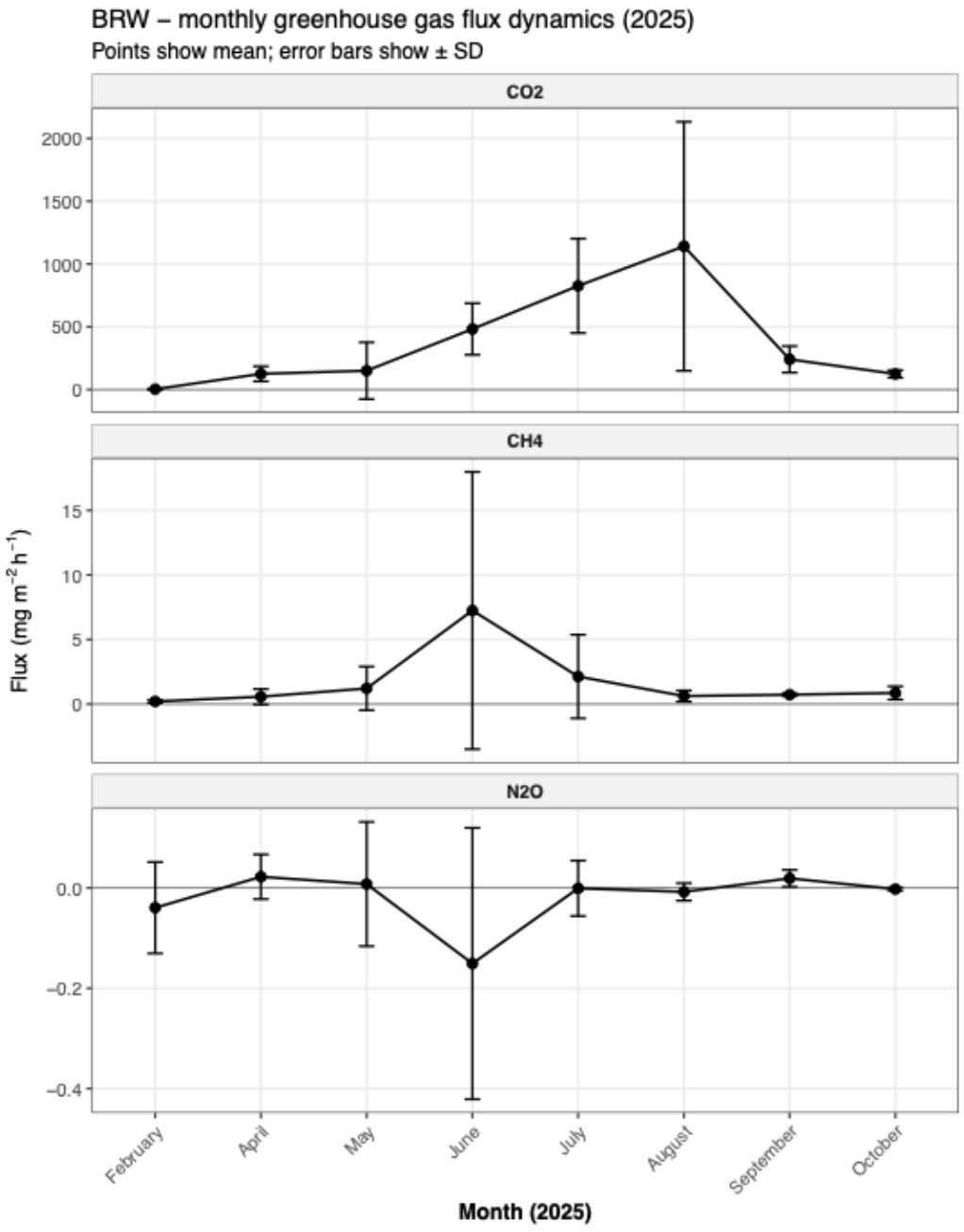

Figure 6. Monthly greenhouse gas fluxes at Beaver River Wetland (BRW), a natural comparison marsh on organic soil, during 2025. Monthly means (mg m^{-2} h^{-1}) ±1 SD for CO_2, CH_4, and N_2O.

2.3.3 Seasonal Summaries Across Sites (2025)

Seasonal aggregation of 2025 fluxes highlights systematic differences among sites for CH_4 but broadly similar patterns for CO_2 and N_2O (Figure 7).

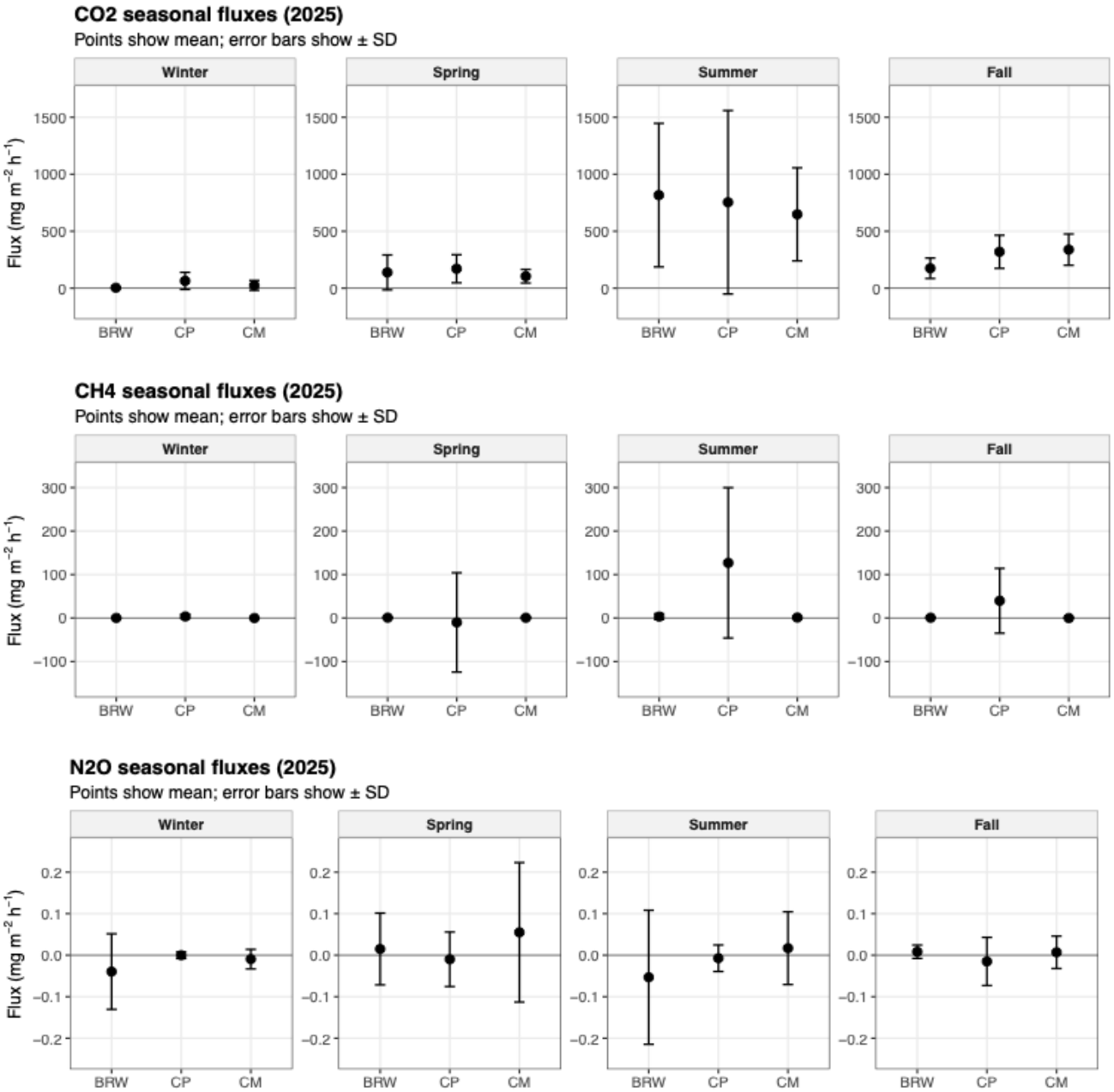

Figure 7. Seasonal greenhouse gas flux summaries (mg m^{-2} h^{-1}) for CO_2, CH_4, and N_2O at Circle Park (CP; permanently flooded constructed, mineral soil), Cawthra Mulock (CM; seasonally flooded constructed, mineral soil), and Beaver River Wetland (BRW; natural permanently flooded, organic soil)

CO_2 fluxes were low during winter across all sites, increased modestly in spring (100–200 mg m^{-2} h^{-1}), and peaked in summer, when mean values exceeded several hundred mg m^{-2} h^{-1}. Summer CO_2 fluxes were highest at BRW and CP, with CM exhibiting slightly lower means but comparable variability. Fall fluxes declined at all sites.

CH_4 fluxes showed pronounced site-level contrasts. Winter and spring fluxes were near zero at the constructed, seasonally flooded (CM) and comparison (BRW) sites, while at the constructed permanently flooded CP they were low but not trivial (2.33 ± 1.92 mg m^{-2} h^{-1}). In summer, CP exhibited mean CH_4 fluxes exceeding 100 mg m^{-2} h^{-1} with large variability, while CM maintained near-zero summer fluxes despite comparable temperatures. BRW showed intermediate behavior—modest positive summer CH_4 fluxes substantially lower than CP despite its organic-rich substrate. Fall CH_4 fluxes declined at all sites but remained elevated at CP relative to CM and BRW.

N_2O fluxes were consistently low across all sites and seasons (typically within ±0.1 mg m^{-2} h^{-1}), with no clear seasonal pattern and both positive and negative values observed.

2.3.4 Interannual Variability (2023–2025)

Interannual comparisons based on matched seasonal sampling (February, April, July, October) revealed variability in flux magnitudes but preserved relative site-level differences (Figure 8).

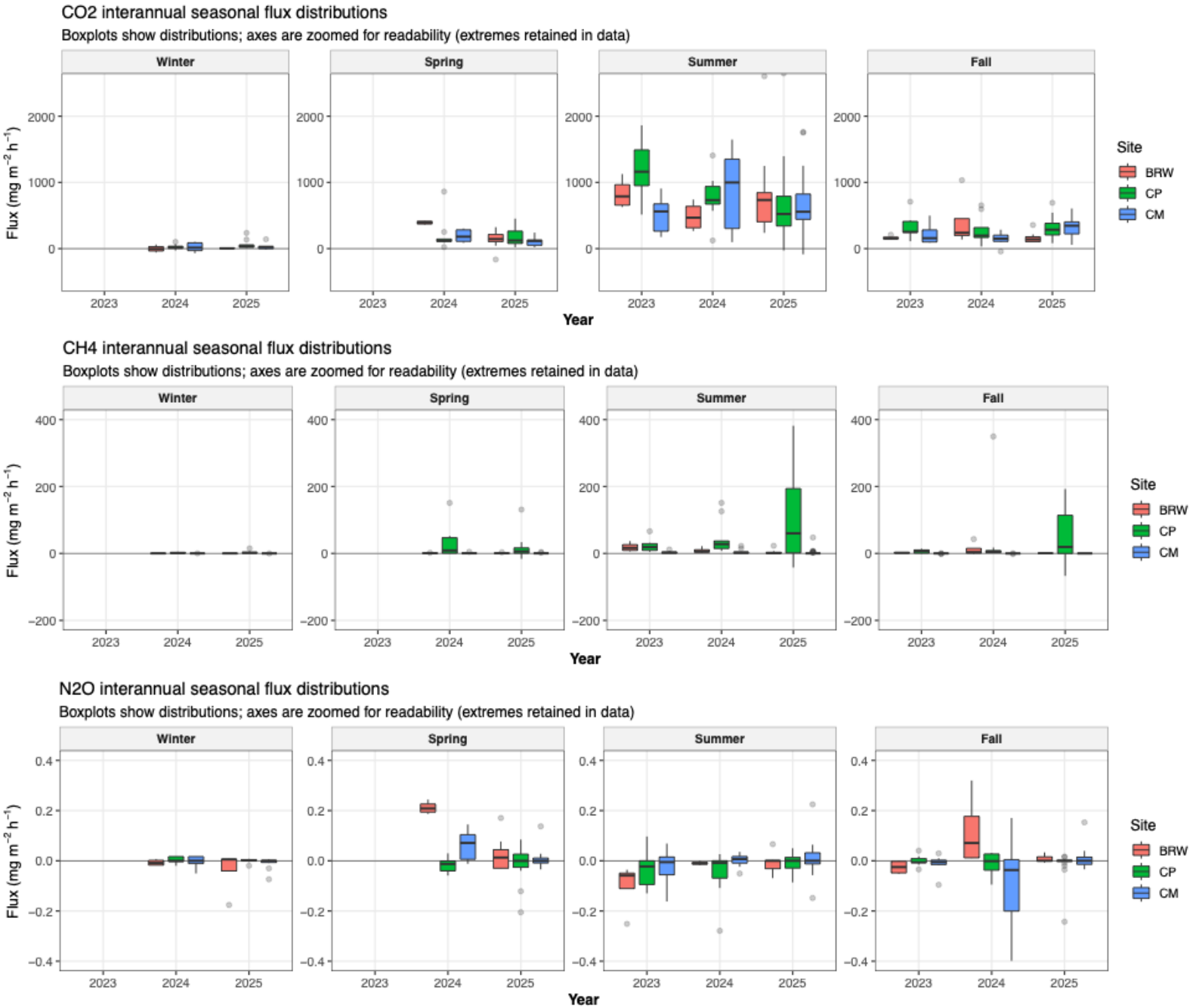

Figure 8. Interannual seasonal flux (mg m^{-2} h^{-1}) distributions for CO_2 (upper panel), CH_4 (middle panel) and N_2O (lower panel) at Circle Park (CP), Cawthra Mulock (CM), and Beaver River Wetland (BRW).

Summer CO_2 fluxes varied among years, with 2025 generally exhibiting higher mean values and greater variability than 2023 and 2024. Despite this variation, the relative ranking of sites was broadly consistent (BRW ≥ CP > CM in summer).

CH_4 fluxes exhibited greater interannual variability than CO_2, particularly during summer. Across all years, the permanently flooded constructed wetland (CP) consistently produced the highest summer CH_4 emissions, followed by BRW, with CM remaining near zero. The suppression of CH_4 at CM relative to CP was robust across years, even as absolute magnitudes varied. The multiannual winter average CH_4 flux at CP (n=18) was 2.78 ±3.6 mg m^{-2} h^{-1}, a value comparable with summer fluxes at CM (n=55; 2.45 ±4.09 mg m^{-2} h^{-1}).

N_2O fluxes showed no clear interannual trends, with seasonal means near zero in all years and variability dominated by episodic events. Overall, interannual variability did not obscure the dominant influence of hydrologic regime on GHG fluxes.

2.3.5 Environmental Controls on Greenhouse Gas Fluxes (2025)

Mixed-effects models were used to assess the influence of site, season, soil temperature, and water table depth on greenhouse gas fluxes in 2025, with plot/chamber identity included as a random intercept. Model performance is summarized using marginal R^2 (fixed effects only) and conditional R^2 (fixed + random effects).

Carbon dioxide

CO_2 fluxes were strongly influenced by soil temperature (Figure 9). Warmer soils were associated with significantly higher CO_2 emissions ($\beta = 47.00$, SE = 12.05, df = 146.81, $p < 0.001$), indicating a pronounced thermal control on ecosystem respiration. In contrast, water table depth showed a marginal negative effect ($\beta = -3.14$, SE = 1.61, df = 69.07, $p = 0.056$), suggesting reduced CO_2 efflux under deeper inundation, although this relationship did not meet

the $\alpha = 0.05$ threshold. Site differences were not significant (CP: $\beta = -27.00$, SE = 136.71, $p = 0.845$; CM: $\beta = -153.98$, SE = 122.46, $p = 0.219$), and season did not improve model performance and was therefore excluded from the final model. Fixed effects explained 34.0% of the variance in CO_2 fluxes (marginal $R^2 = 0.340$), increasing to 40.8% when chamber-level random effects were included (conditional $R^2 = 0.408$), indicating that persistent among-chamber differences account for additional structured variation beyond the measured environmental predictors.

Methane

Methane fluxes exhibited clear seasonal and hydrological controls (Figure 10). Relative to winter, emissions increased significantly in summer ($\beta = 81.24$, SE = 14.87, df = 159, $p = 0.002$) and remained elevated into fall ($\beta = 65.77$, SE = 19.98, df = 159, $p = 0.050$). Water table depth exerted a strong positive influence on CH_4 flux ($\beta = 1.22$, SE = 0.30, df = 159, $p < 0.001$), consistent with enhanced methanogenesis under wetter conditions. In contrast, soil temperature was not a significant predictor ($\beta = 0.58$, SE = 2.60, df = 159, $p = 0.823$). Site effects were not significant in the full model (CP: $\beta = 13.90$, SE = 23.68, $p = 0.558$; CM: $\beta = -19.90$, SE = 20.91, $p = 0.343$), suggesting that the combined environmental covariates—particularly water table depth and season—account for much of the among-site variability in CH_4 flux. However, a targeted mediation analysis (see Section 2.4.1) indicated that instantaneous water table depth alone only partially mediates the site contrast, with residual site effects likely reflecting cumulative hydrologic regime properties not captured by single-point measurements. Environmental predictors accounted for 24.3% of methane flux variance (marginal $R^2 = 0.243$). The random intercept for chamber identity was estimated at zero variance (singular fit), indicating that CH_4 variability is structured primarily at the site and season level rather than by

persistent among-chamber differences within sites. Fixed-effect estimates remain valid under singularity.

Nitrous oxide

Nitrous oxide fluxes showed limited environmental structuring (Figure 9 and 10). Neither soil temperature ($\beta = -0.00019$, SE = 0.00282, df = 148.52, $p = 0.946$) nor water table depth ($\beta = -4.38 \times 10^{-5}$, SE = 3.71×10^{-4}, df = 68.28, $p = 0.906$) significantly influenced N_2O emissions. Seasonal contrasts were also non-significant (Summer: $\beta = -0.0283$, SE = 0.0166, df = 153.24, $p = 0.259$; Fall: $\beta = -0.0275$, SE = 0.0217, df = 152.03, $p = 0.595$), as were site effects (CP: $\beta = 0.00895$, SE = 0.0309, $p = 0.793$; CM: $\beta = 0.0426$, SE = 0.0276, $p = 0.137$).

Fixed effects explained only 5.2% of the variance in N_2O fluxes (marginal $R^2 = 0.052$), increasing to 13.7% with chamber-level random effects (conditional $R^2 = 0.137$), reflecting substantial unexplained variability and weak coupling to the measured environmental gradients.

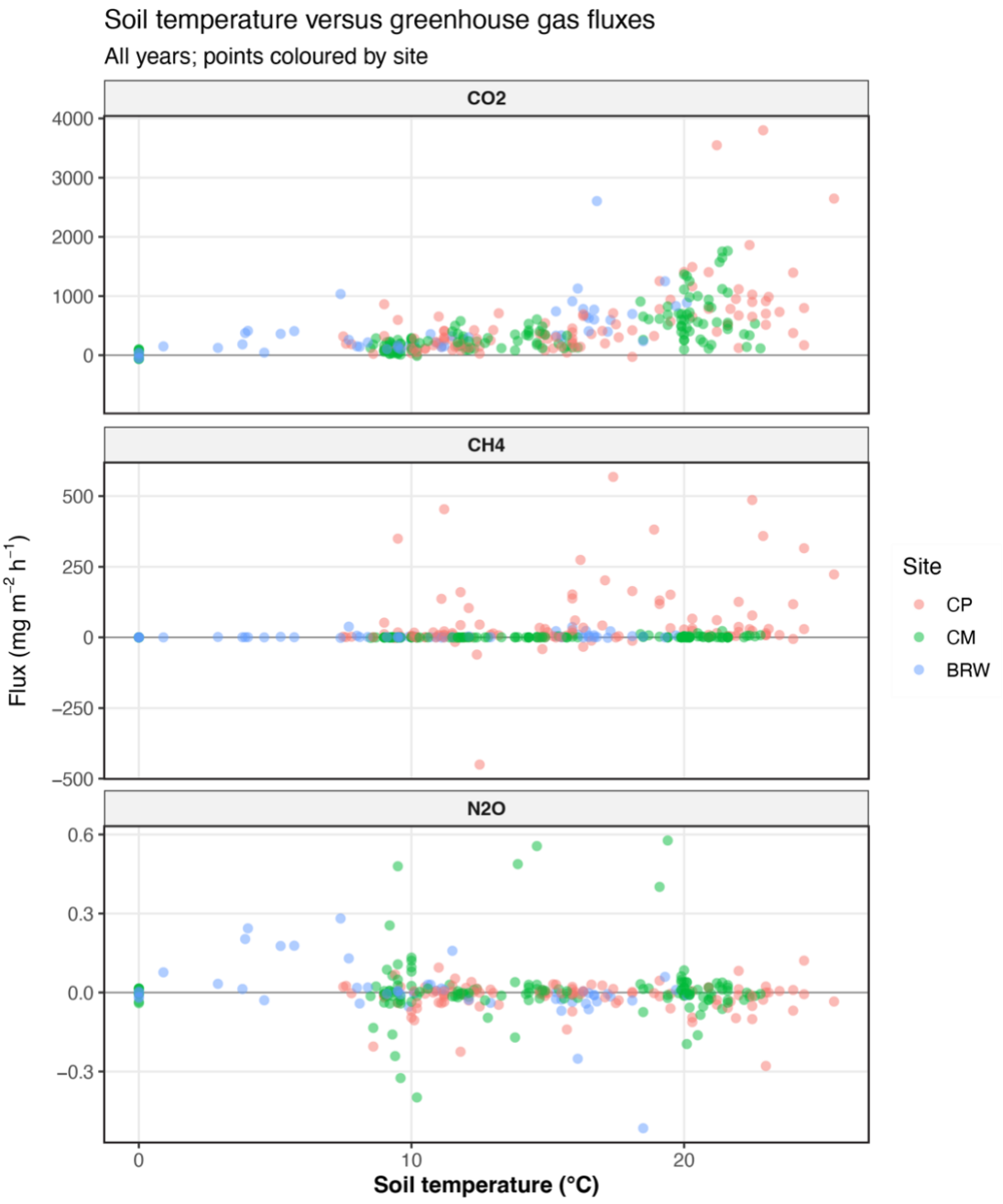

Figure 9. Relationship between soil temperature and greenhouse gas fluxes across all sites and sampling periods. Points represent individual chamber measurements; colours indicate site.

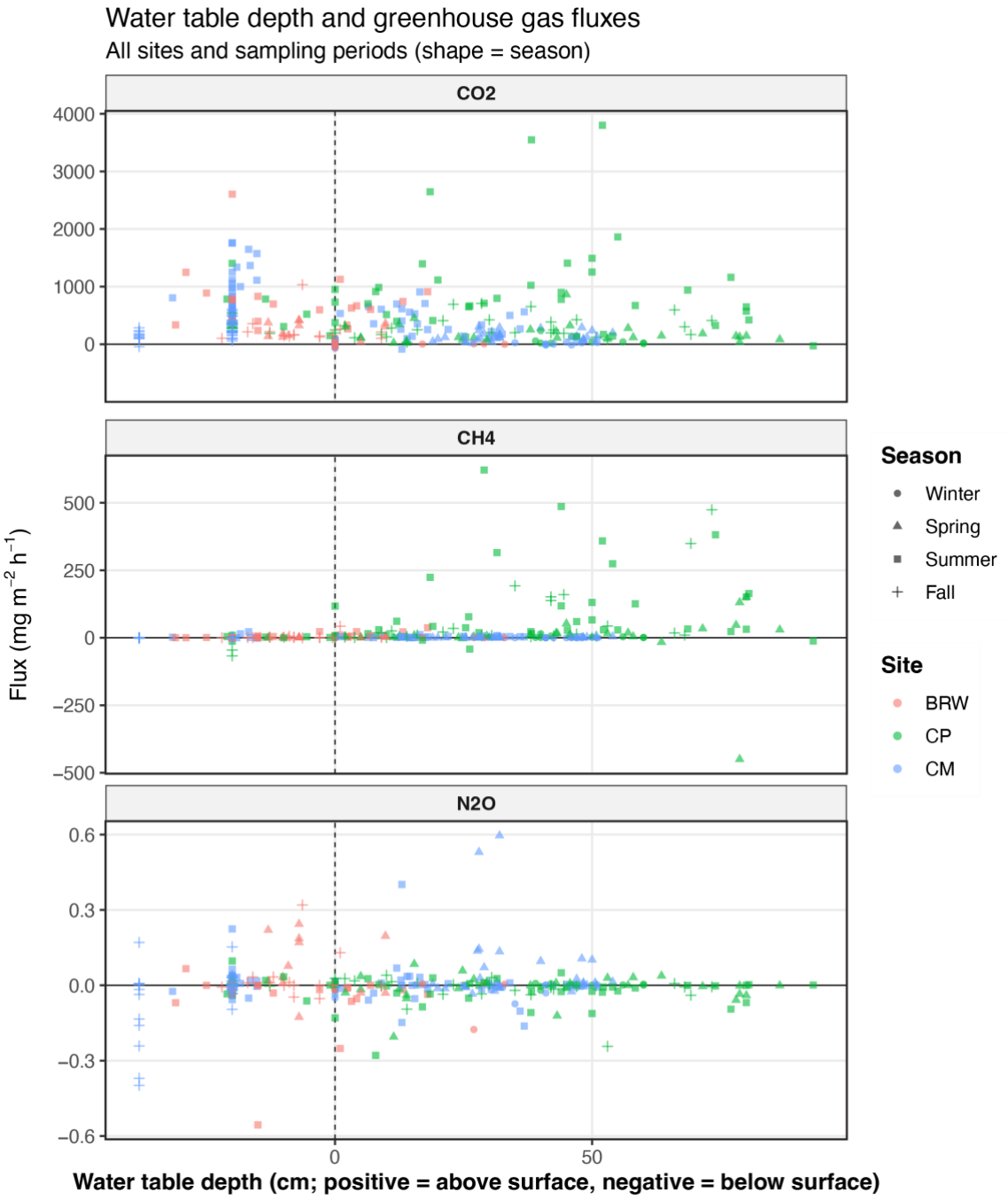

Figure 10. Relationship between water table depth and greenhouse gas fluxes across all sites and sampling periods. Points represent individual chamber measurements; colours indicate site and symbols indicate season. The vertical dashed line denotes the soil surface (0 cm). This visualization complements the soil temperature–flux relationship (Fig. 9) and provides seasonal context for hydroperiod-GHG flux relationships.

2.3.6 Diurnal Variability (July 2025)

Diurnal measurements in July 2025 revealed within-day patterns for CO_2 and CH_4, while N_2O fluxes remained small and variable (Figure 11).

CO_2 fluxes increased from morning to afternoon and remained elevated into the night at all sites. Mean CO_2 fluxes were lowest at 08:00 and highest at 00:00, with intermediate values at 16:00 and increasing variability later in the day. This pattern is consistent with accumulated soil heat driving respiration through evening and nighttime periods and suggests that single midday measurements may underestimate daily CO_2 flux.

CH_4 fluxes exhibited clear diurnal variation only at the permanently flooded site (CP), where mean fluxes peaked in the afternoon (16:00) and declined by midnight. At CM, CH_4 remained near zero at all times of day, and BRW showed low, non-patterned CH_4 fluxes throughout the diurnal cycle. The restriction of a diurnal CH_4 signal to the permanently flooded site is consistent with temperature-driven amplification of plant-mediated gas transport under continuously anaerobic conditions—a pattern reported for *Typha*-dominated wetlands where aerenchymal transport is greatest during periods of active photosynthesis and highest temperatures (Bansal et al., 2020; Dušek et al., 2023).

N_2O fluxes showed no consistent diurnal structure at any site. Overall, diurnal variability was secondary to seasonal and site-level controls on GHG fluxes.

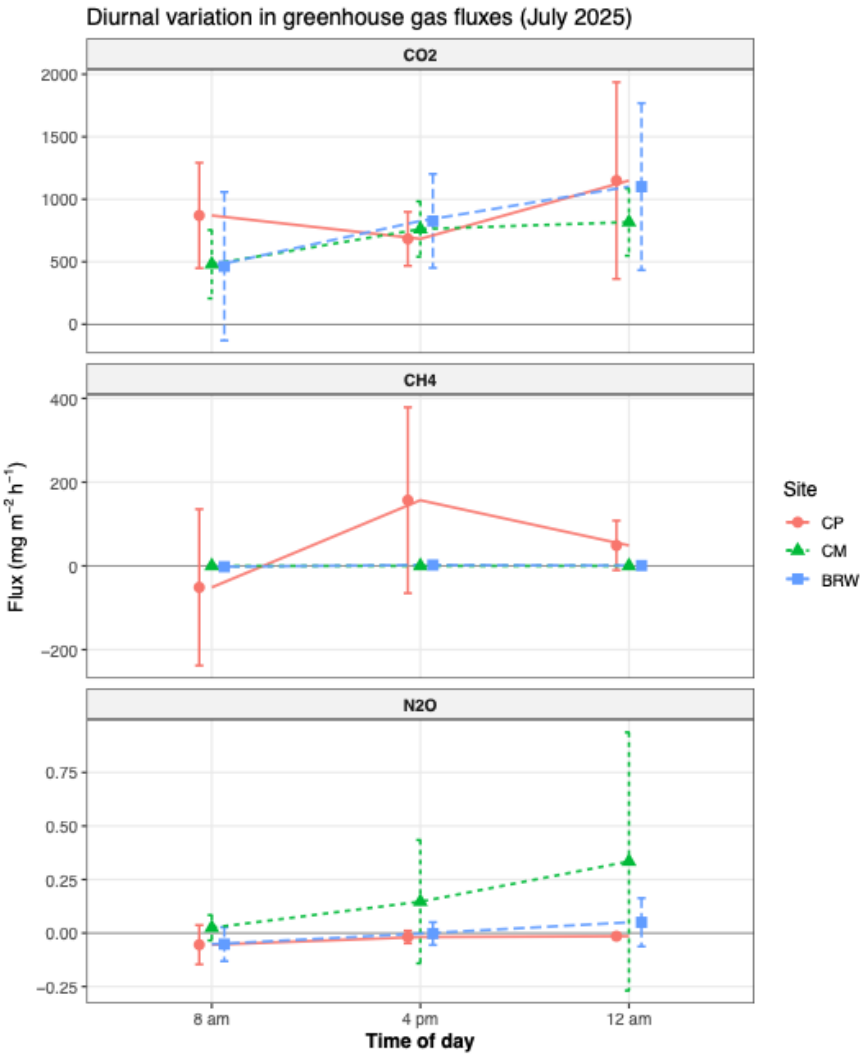

Figure 11. Diurnal variation in flux (mg m^{-2} h^{-1}) for CO_2, CH_4, and N_2O at 08:00, 16:00, and 00:00.

2.3.7 Integrated Warming Potential

Because fluxes were measured using dark static chambers, CO_2 fluxes represent ecosystem respiration rather than net ecosystem CO_2 exchange. The integrated metric presented here therefore reflects the warming potential of measured gaseous fluxes (ER + CH_4 + N_2O), not a net ecosystem climate balance.

Annual mean fluxes were converted to CO_2-equivalent fluxes (mg CO_2e m^{-2} h^{-1}) using GWP_{100} values from IPCC AR6 (Table 1). The permanently flooded constructed wetland (CP) exhibited the highest CO_2-equivalent flux in all three years (1,963, 1,165, and 2,318 mg CO_2e m^{-2} h^{-1} in 2023, 2024, and 2025, respectively). Methane accounted for 56–82% of total forcing at this site, indicating that CH_4 dominated the climatic impact despite lower mass flux relative to CO_2.

The seasonally flooded constructed wetland (CM) consistently exhibited the lowest CO_2-equivalent flux (342–405 mg CO_2e m^{-2} h^{-1}), with CH_4 contributing only 5–16% of total forcing. The natural comparison wetland (BRW) showed intermediate values (409–770 mg CO_2e m^{-2} h^{-1}), with CH_4 contributing 11–37% depending on year. Notably, BRW's intermediate position occurred despite its organic-rich substrate (~37% OC), which would be expected to support higher methanogenic activity than the mineral soils at CP and CM; the lower CH_4 contribution at BRW relative to CP is therefore attributable to shallower and more variable inundation rather than substrate limitation. Across all sites and years, variation in CH_4 emissions explained most of the difference in integrated climatic forcing, whereas N_2O contributions were negligible.

Table 1. Integrated sustained-flux global warming potential (GWP_{100}) by site and year.

Year	Site	CO_2e (mg m^{-2} h^{-1})
2023	Beaver River	770
2023	Cawthra Mulock	342
2023	Circle Park	1,963
2024	Beaver River	497
2024	Cawthra Mulock	357
2024	Circle Park	1,165
2025	Beaver River	409
2025	Cawthra Mulock	405
2025	Circle Park	2,318

2.4 Discussion

2.4.1 Hydrologic Regime as the Dominant Control on Methane Emissions

Across three years of measurements, hydrologic regime emerged as the primary determinant of CH_4 emissions, overriding differences in both wetland origin and substrate type. Permanently flooded conditions at Circle Park—a young, constructed wetland on mineral soil—supported sustained positive CH_4 fluxes across all seasons, including winter and early spring, and produced substantially higher annual CH_4 emissions than either the seasonally flooded constructed wetland (Cawthra Mulock) or the natural comparison marsh (Beaver River). The suppression of CH_4 at CM was consistent and robust, persisting even during peak summer temperatures. This strong separation among sites was preserved across seasonal aggregation, interannual comparisons, and diurnal analyses. Although the full mixed-effects model explained a modest fraction of total CH_4 variance (marginal $R^2 = 0.243$), this is consistent with the characteristically high spatial and temporal heterogeneity of wetland methane emissions (Bridgham et al., 2013). Critically, the evidence for hydrologic dominance rests not on any single-model R^2 but on the convergence of multiple independent lines of evidence: the three-year consistency of site-level contrasts, the suppression of CH_4 at CM despite comparable summer temperatures, and the presence of winter CH_4 emissions exclusively at the permanently flooded site.

To evaluate whether measured hydrologic conditions mediate the among-site contrast in CH_4 flux, we compared nested mixed-effects models. A site-only model confirmed that sites differed significantly in CH_4 emissions ($F(2, 21) = 7.73$, $p = 0.003$; marginal $R^2 = 0.106$). When instantaneous water table depth was added, the site effect was attenuated—the Circle Park coefficient declined by 33% (from 62.2 to 41.6 mg m^{-2} h^{-1} relative to BRW)—and water table depth was a significant predictor ($\beta = 16.4$, $p = 0.033$), though the site effect remained significant ($p = 0.009$). A water-depth-only model was also significant ($p < 0.001$; marginal $R^2 = 0.077$), but

adding site improved it significantly (likelihood ratio $\chi^2 = 5.72$, $p = 0.017$), indicating that site identity carries information beyond instantaneous water depth. This pattern is consistent with partial mediation: instantaneous water table depth accounts for a substantial portion of the among-site CH_4 contrast, but the residual site effect likely reflects cumulative hydrologic regime properties—such as the permanence and stability of inundation—that single-point water depth measurements cannot fully capture. This distinction between instantaneous water level and hydrologic regime reinforces the central thesis that it is the depth and duration of inundation, not merely water level at any given moment, that governs CH_4 dynamics in these systems.

These results are consistent with well-established mechanistic understanding of wetland methane dynamics. Sustained inundation maintains anaerobic conditions that favor methanogenesis while limiting methane oxidation at the soil–water interface (Segers, 1998; Bridgham et al., 2006). Periodic drying, in contrast, increases oxygen penetration into surface soils, stimulating methanotrophy and disrupting methanogenic communities (Le Mer & Roger, 2001; Reddy et al., 2022). The near-zero CH_4 fluxes at Cawthra Mulock during summer, despite soil temperatures exceeding 20°C, provide particularly compelling evidence for the primacy of hydrologic over thermal controls.

The dominance of hydrology over temperature in structuring CH_4 emissions aligns with findings from temperate mineral-soil wetlands elsewhere. In the Canadian Prairie Pothole Region, Pennock et al. (2010) found that landscape position and associated water table dynamics explained more variance in CH_4 flux than temperature, and Creed et al. (2013) demonstrated that hydrologic profiling could predict greenhouse gas efflux patterns in freshwater mineral-soil wetlands. Similarly, Mander et al. (2011) showed that pulsing hydrology and fluctuating water

tables were key regulators of CH_4 emissions in constructed systems, consistent with the strong site-level contrasts observed here.

Winter CH_4 fluxes at Circle Park deserve particular attention. They were measurable and, in some months, comparable in magnitude to summer CH_4 fluxes at the seasonally flooded site. Many temperate wetland studies omit cold-season sampling, implicitly assuming negligible methane production during winter. However, growing evidence indicates that CH_4 production and release can persist under ice-covered or near-freezing conditions when soils remain saturated (Wik et al., 2016; Turetsky et al., 2014). Our results reinforce this view and demonstrate that exclusion of cold-season fluxes may lead to underestimation of annual methane budgets in permanently inundated systems.

2.4.2 Temperature as a Seasonal Modulator of CO_2 but Insufficient to Explain CH_4 Contrasts

Soil temperature was positively associated with CO_2 fluxes across all sites, consistent with established temperature sensitivity of soil and ecosystem respiration (Davidson & Janssens, 2006). Seasonal increases in CO_2 flux from winter through summer tracked rising soil temperatures, and diurnal measurements revealed higher CO_2 emissions during warmer afternoon and nighttime periods.

However, correlations between soil temperature and CH_4 fluxes were weak and site-specific. At the permanently flooded wetland, warmer temperatures amplified CH_4 emissions during summer, but at the seasonally flooded wetland, elevated temperatures did not produce corresponding increases in methane flux. This decoupling confirms that while temperature modulates methane production under anoxic conditions, it cannot override hydrologic suppression where oxygen

periodically penetrates soils. Similar findings have been reported across both restored and natural mineral-soil wetlands, where water table position frequently explains greater variance in CH_4 flux than temperature alone (Knox et al., 2015; Bridgham et al., 2006; Pennock et al., 2010). Temperature thus operates as a secondary control whose effect is contingent upon hydrologic state.

N_2O fluxes showed weak and inconsistent relationships with both temperature and hydrology, reflecting the episodic and transient nature of nitrification–denitrification dynamics in wetland soils (Reddy et al., 2022). The absence of sustained N_2O emissions at any site is consistent with the generally low nitrate availability in these non-nutrient-enriched systems, which contrasts with the elevated N_2O fluxes often reported from wastewater treatment constructed wetlands receiving high nitrogen loads (Mander et al., 2014).

Overall, our results support a hierarchical control framework in which hydrology governs redox conditions and CH_4 production potential, while temperature modulates the rate of CH_4 and CO_2 flux within hydrologic constraints.

2.4.3 Hydrologic Regime Overrides Substrate Type and Wetland Origin

A notable finding of this study is that a young, constructed wetland on mineral soil (Circle Park) produced substantially higher CH_4 emissions and integrated warming potential than a mature natural marsh on organic soil (Beaver River), despite the expectation that organic-rich substrates would support greater methanogenic activity. This comparison involves a single site per category, and the two systems differ not only in substrate but also in hydrologic regulation (engineered vs. river-driven) and wetland origin, so the inference requires validation across additional sites. Nonetheless, the pattern is consistent across all three years of measurement.

Beaver River's soil contains approximately 37% organic carbon—lower than typical peatlands but substantially higher than the mineral soils at both constructed sites—and thus provides ample labile carbon to sustain methanogenesis (Segers, 1998; Tangen & Bansal, 2020). Yet CH_4 fluxes at BRW were intermediate between the two constructed sites and far below those at CP in every year of the study.

This pattern challenges the assumption, supported by some comparative studies, that high organic carbon availability drives elevated CH_4 emissions largely irrespective of other site conditions (Mitsch et al., 2013). However, the systems examined in such studies are often peat-dominated wetlands with deep and stable water tables that consistently maintain the anaerobic conditions needed for methanogenesis. At Beaver River, permanent but relatively shallow inundation with greater water-level variability in response to river hydrology appears to limit the extent and persistence of anaerobic conditions relative to the deeply and consistently flooded mineral-soil system at Circle Park. Greater water-level fluctuation can enhance oxygen penetration into surface soils—even in organic substrates—stimulating methanotrophy and periodically disrupting methanogenic microbial communities (Le Mer & Roger, 2001; Reddy et al., 2022).

These results suggest that in *Typha*-dominated wetlands, the depth and stability of inundation may be more important determinants of CH_4 flux than either substrate organic carbon content or wetland origin. This conclusion has direct implications for how constructed wetlands are evaluated as climate-relevant nature-based solutions (Villa & Bernal, 2018). Habitat-oriented constructed wetlands on mineral soils should not be assessed using emission factors derived from wastewater treatment systems, which experience fundamentally different biogeochemical regimes with GHG emissions 2–10 times higher than natural systems (Mander et al., 2014). Nor

should they be compared primarily to peatland benchmarks, which reflect different substrate characteristics. Instead, their GHG performance should be evaluated in the context of their specific hydrologic design—particularly the depth and duration of inundation.

The role of *Typha latifolia* in mediating gas transport further underscores this point. *Typha* possesses well-developed aerenchymal tissue that facilitates both oxygen transport to the rhizosphere and CH_4 transport to the atmosphere, effectively bypassing the oxidation zone at the soil–water interface (Bansal et al., 2020). Under permanently flooded conditions, this plant-mediated pathway can represent the dominant route for CH_4 release. Conversely, in seasonally dry systems, the collapse of the water table limits the production of CH_4 that plants could transport. The consistently low CH_4 fluxes at CM, despite its dominantly *Typha* cover, illustrate that aerenchymal transport is inconsequential in the absence of sustained methanogenesis. At BRW, the combination of organic substrate and permanent but shallow inundation sustained modest CH_4 fluxes—higher than the seasonally flooded CM but far below CP—consistent with intermediate redox conditions that support some methanogenesis but also allow partial methane oxidation.

2.4.4 Integrated Warming Potential and Climate Trade-offs

Although CO_2 dominated mass fluxes at all sites, CH_4 exerted a disproportionate influence on integrated warming potential due to its higher radiative efficiency (IPCC, 2021). At the permanently flooded site, CH_4 contributed 56–82% of total CO_2-equivalent flux depending on year—a proportion consistent with findings from other temperate freshwater wetlands where CH_4 accounts for more than half of global warming potential under sustained inundation (Ma et al., 2024). In contrast, CH_4 contributed less than 15% of total forcing at the seasonally flooded site, where the climate impact was dominated by respiratory CO_2. The natural comparison marsh

on organic soil occupied an intermediate position (11–37%), reflecting its intermediate hydrologic regime rather than its higher substrate carbon content. An important caveat applies to these estimates: because fluxes were measured using opaque static chambers, the CO_2 component represents ecosystem respiration only and excludes photosynthetic CO_2 uptake. The SFGWP values reported here therefore represent the warming potential of measured gaseous effluxes (ER + CH_4 + N_2O), not a net ecosystem radiative balance. Preliminary biomass data collected at these sites as part of a companion study (Pendea, unpublished data) indicate substantial aboveground and belowground carbon assimilation by *Typha* stands at all three sites, with multiannual dry biomass at BRW of 6935 g m^{-2} CO_2-equivalent, and values at CP and CM of 2,805 and 1, 427 g m^{-2} CO_2-equivalent, respectively. The magnitude of this vegetative carbon uptake suggests that the net radiative balance at these sites may differ substantially from the emission-side estimates presented here, particularly at sites combining high biomass productivity with low CH_4 emissions. A full accounting of the net ecosystem climate balance—integrating both photosynthetic uptake and gaseous effluxes—requires transparent chamber or eddy covariance measurements and is beyond the scope of this study but would likely reduce the apparent climatic cost at all sites and could alter the relative ranking among them.

This divergence underscores a critical climate trade-off in wetland design. Permanent deep inundation maximizes the provision of open-water habitat and may enhance certain ecosystem services (e.g., waterfowl habitat, stormwater retention), but it also maximizes methane-related warming potential. Seasonal drawdown, by contrast, may reduce habitat quality for some obligate wetland species but substantially reduces integrated climatic impact. Ma et al. (2024) reached a similar conclusion using process-based modeling, finding that the net climate benefit

of temperate mineral-soil wetlands is highly sensitive to hydroperiod when evaluated using sustained-flux metrics.

The presence of measurable winter CH_4 emissions at Circle Park further implies that annual GHG budgets for permanently flooded systems cannot be estimated from growing-season data alone particularly for regions with long winters such as central Ontario. Omitting cold-season fluxes would underestimate the annual CH_4 contribution—and therefore the integrated warming potential - of such systems. This finding has practical implications for monitoring protocols used to verify wetland carbon credits and to evaluate the climate performance of constructed wetlands within NbCS frameworks.

Adaptive management of hydroperiod—for example, through controlled seasonal drawdown—may represent a practical mechanism to balance ecosystem service delivery with climate performance (Villa & Bernal, 2018). Such approaches are already discussed in the context of peatland rewetting and rice paddy management but remain underexplored for habitat-oriented constructed wetlands on mineral soils. Our results suggest that even modest reductions in the depth or duration of inundation could substantially reduce CH_4 contributions to integrated warming potential without necessarily eliminating the wetland functions that depend on seasonal flooding.

2.4.5 Contextualizing Emissions Within the Temperate Wetland Literature

To situate these findings within the broader literature, we compared our flux measurements against published values from five temperate wetland studies spanning natural marshes, created riverine wetlands, European constructed wetlands, and prairie agricultural waterbodies (Bonneville, 2006; Nahlik & Mitsch, 2010; Søvik et al., 2006; Maucieri et al., 2017; Jensen, 2023). All CH_4 fluxes were harmonized to mg CH_4 m^{-2} h^{-1} for direct comparison.

Circle Park's median CH_4 flux (~23.6 mg m^{-2} h^{-1}, PRIME 2025) places it among the higher-emitting temperate wetland systems in the literature. It substantially exceeds the planted and self-colonized created wetlands in central Ohio (equivalent to ~1 and ~3.8 mg m^{-2} h^{-1} respectively; Nahlik & Mitsch, 2010), all four European CW types studied by Søvik et al. (2006; summer means of 6–17 mg CH_4 m^{-2} h^{-1}), Saskatchewan agricultural reservoirs and natural wetland ponds (~2.1–2.3 mg m^{-2} h^{-1}; Jensen, 2023), and T. domingensis marshes in Florida (127–297 mg m^{-2} d^{-1}, or ~5.3–12.4 mg m^{-2} h^{-1}; Chanton et al., 1993). However, Circle Park falls within—rather than above—the range of previously reported Typha latifolia systems. Yavitt and Knapp (1995), measuring CH_4 emission directly through T. latifolia leaves across nine wetlands spanning 21° of latitude in the United States, reported a ground-area mean of 940 mg CH_4 m^{-2} d^{-1} (~39.2 mg m^{-2} h^{-1}) with individual site rates ranging from 43 to as high as 6,000 mg m^{-2} d^{-1}. They proposed that plant age, stomatal conductance, and sediment CH_4 concentration interact hierarchically to control emission rates, with older plants being more efficient conduits. Kim et al. (1999) similarly reported 40–650 mg m^{-2} d^{-1} (~1.7–27.1 mg m^{-2} h^{-1}) from a temperate Phragmites marsh, with Circle Park's values falling in the upper portion of that range. Circle Park remains substantially below the area-weighted mean of the Mer Bleue cattail marsh (~52.7 mg m^{-2} h^{-1}; Bonneville, 2006), a mature natural Typha angustifolia system near Ottawa that produced 275 g CH_4 m^{-2} yr^{-1} and whose plant-mediated fluxes were 2.7 times higher than open-water diffusion. Together, these comparisons indicate that Circle Park's emissions, while high for a constructed wetland, are well within the envelope reported for cattail-dominated temperate marshes and consistent with the mechanistic framework linking Typha aerenchyma, sustained inundation, and elevated methanogenesis (Yavitt & Knapp, 1995; Bonneville, 2006; Maucieri et al., 2017).

Cawthra Mulock (~0.85 mg m^{-2} h^{-1}) and Beaver River (~1.3 mg m^{-2} h^{-1})—the latter a natural marsh—fell within the lower end of the European CW range and were comparable to Saskatchewan prairie waterbodies and mid-boreal marshes (4–350 mg m^{-2} d^{-1}; Bubier et al., 1993). The Maucieri et al. (2017) meta-analysis of 224 studies confirmed that FWS constructed wetlands produce significantly higher CH_4 than subsurface-flow systems, and that CH_4 emissions increase with CW age—both factors consistent with Circle Park's elevated fluxes relative to the other two sites.

CO_2 fluxes from dark chambers at our sites (median ~300–420 mg m^{-2} h^{-1}) represent ecosystem respiration and fall within the range reported for European CWs (Søvik et al., 2006). Bonneville (2006) measured a net annual CO_2 sink of 264 g C m^{-2} yr^{-1} at the Mer Bleue cattail marsh via eddy covariance, demonstrating that productive Typha stands can achieve substantial net CO_2 uptake that our dark-chamber methodology cannot capture. Maucieri et al. (2017) similarly concluded that vegetated CWs generally act as net CO_2(eq) sinks when photosynthetic uptake is included in the balance.

N_2O fluxes near zero to slightly negative at all three sites are consistent with the lowest values from European FWS CWs (Søvik et al., 2006) and with Jensen's (2023) finding of persistent N_2O undersaturation in 95% of Saskatchewan natural wetland ponds. This emerging pattern suggests that saturated FWS marshes in cold-temperate Canada commonly function as minor N_2O sinks, confirming that the GHG footprint of these systems is governed almost entirely by the CH_4–CO_2 balance.

Together, this contextualisation reinforces that site-specific factors—particularly Typha dominance, prolonged inundation, and organic matter accumulation (Maucieri et al., 2017; Nahlik & Mitsch, 2010)—drive CH_4 emission variability far more than N_2O or CO_2 respiration in

cold-temperate FWS systems, and that Circle Park's emissions, while high, are well within the envelope of published values for cattail-dominated temperate marshes.

INTEGRATION BETWEEN CHAPTER 2 AND 3

Chapter 2 established that hydrologic regime is the primary control on methane emissions in mineral-soil constructed wetlands, overriding substrate type and wetland origin, with permanently flooded conditions sustaining elevated CH_4 fluxes across all seasons. However, environmental measurements alone—water table depth, soil temperature—explained only a fraction of the observed variance in CH_4 flux (marginal $R^2 = 0.243$), leaving substantial variability unaccounted for. This gap motivates the question of whether biological community structure can provide complementary information about the biogeochemical conditions that underlie greenhouse gas dynamics. Soil microbiota integrates overlapping environmental gradients over ecologically relevant timescales, potentially capturing aspects of ecosystem state—such as cumulative redox history, carbon availability, and microbial food-web interactions—that instantaneous physicochemical measurements cannot. Heterotrophic protists and phototrophic microbiota are well-established bioindicators in wetland systems, and recent peatland research suggests that protist community structure may align with methane cycling at ecosystem scales (Davies et al., 2021; Frésard et al., 2023). Whether such relationships extend to mineral-soil constructed wetlands—systems with fundamentally different substrate composition and hydrologic regulation—remains unknown. Chapter 3 therefore asks whether cross-assemblage microbial community structure correlates with greenhouse gas fluxes and environmental drivers in the same mineral-soil wetlands examined in Chapter 2 and evaluates whether microbial communities could serve as integrative bioindicators of methane-relevant biogeochemical state in these systems.

CHAPTER 3: EXPLORATORY EVIDENCE FOR CROSS-ASSEMBLAGE CONVERGENCE OF SOIL PROTIST AND PHOTOTROPHIC MICROBIOTA ALONG METHANE-ASSOCIATED GRADIENTS IN MINERAL-SOIL CONSTRUCTED WETLANDS

3.1 Introduction

Wetlands regulate carbon and nutrient cycling at global scales, functioning simultaneously as long-term carbon sinks and significant sources of greenhouse gases, particularly methane (Bridgham et al., 2013; Whalen, 2005). Constructed wetlands, designed primarily for wastewater polishing and stormwater retention, enhance nutrient removal through engineered hydrologic and vegetation features (Vymazal, 2007; Kadlec and Wallace, 2009). However, the same anaerobic conditions that promote denitrification and nutrient sequestration also favour methanogenesis, creating a management tension between water-quality objectives and greenhouse gas mitigation (Mander et al., 2014). Predicting gas fluxes from environmental measurements alone remains challenging because hydrologic variability, substrate chemistry, and redox conditions interact in non-linear ways to determine rates of methanogenesis, methanotrophy, nitrification, and denitrification (Segers, 1998).

Soil microbiota communities integrate these overlapping environmental gradients over time and may provide complementary information about biogeochemical state. Protists, algae, cyanobacteria, and associated microbiota respond sensitively to nutrient availability, redox conditions, and hydrologic regime (Geisen et al., 2018; Mitchell et al., 2008). Testate amoebae—the dominant heterotrophic protist group in many wetland soils—occupy central positions in microbial food webs, grazing on bacteria and modulating microbial biomass turnover (Wilkinson

and Mitchell, 2010; Jassey et al., 2013). Phototrophic microorganisms, including diatoms, green algae, and cyanobacteria, contribute to primary production, oxygen dynamics, and substrate supply at the soil–water interface (Stevenson et al., 1996; Van Dam et al., 1994). Together, these assemblages reflect the ecological state of wetland soils and the biogeochemical processes operating within them.

Recent peatland research has generated growing evidence that protist community composition may align with methane cycling. Jassey et al. (2015) demonstrated that mixotrophic testate amoebae can meaningfully modulate peatland carbon-cycle responses under warming conditions. Proof-of-concept work has further suggested that methane emissions may be inferable from testate amoeba assemblages preserved in peat archives, implying a strong ecological linkage between protist community structure and methane expression at ecosystem scales (Davies et al., 2021; Frésard et al., 2023). These findings raise the possibility that microbiota community structure can serve as an integrative proxy for methane-relevant biogeochemical conditions. However, most evidence to date derives from organic peatland systems. Mineral-soil wetlands differ fundamentally in substrate composition, hydrologic regulation, and microbial habitat structure. Whether cross-assemblage microbial gradients in constructed wetlands align with greenhouse gas fluxes remains largely unexplored. Moreover, prior work has focused primarily on individual assemblages rather than examining convergence across functionally distinct microbial groups.

3.2 Materials and Methods

3.2.1 Study Sites

The study was conducted at two constructed wetlands (Cawthra Mulock and Circle Park, hereafter CM and CP respectively) and one comparison *Typha latifolia*-dominated organic

wetland (Beaver River Wetland, hereafter BRW) located in Southern Ontario, Canada. CM (n = 11 chambers) and CP (n = 9 chambers) were established on mineral substrates in 2021 and feature multiple seasonally flooded excavated basins colonized by *Typha latifolia.*, mixed invasive and ruderal vegetation (CM) and a permanently flooded *Typha*-dominated stormwater wetland (CP). BRW (n = 4 chambers) is a naturally developed organic system characterized by persistent *Typha* spp. cover and peat accumulation.

Regional climate is classified as Köppen *Dfb*, with a mean annual temperature of 9 °C and mean annual precipitation of approximately ~800 mm (Environment and Climate Change Canada, n.d.). Water levels in the constructed wetlands fluctuate seasonally in response to precipitation and stormwater inputs, whereas BRW maintains a relatively stable hydroperiod. The lower replication at BRW (n = 4) relative to CM and CP reflects site access constraints and increases uncertainty in site-level estimates; this imbalance is considered when interpreting multivariate and correlative results. Additional site characteristics are provided in Table 2.

3.2.2 Soil Surface Microbiota Sampling and Identification

A surface soil sample approximately 0.3 cm thick (volume ≈ 2 cm^3) was collected from each of 24 permanent chamber collars distributed across the three sites during the 2025 sampling season. Samples integrate cumulative community composition—including deposited plankton and biofilms containing benthic diatoms, green algae, and cyanobacteria—across the April–October growing season, corresponding to the temporal window of atmospheric flux measurements. Surface samples received minimal processing to preserve taxonomic diversity. Samples were gently heated in a water bath at 95°C for 15 minutes, then wet-sieved through a 300 µm mesh to remove coarse particles. The retained fraction was washed over a 7 µm mesh sieve to remove

clay particles and fine organic detritus. This protocol minimizes loss or deterioration of most microorganisms, although diatoms smaller than 7 µm were likely underrepresented. Specimens were identified using *Testate amoebae as paleohydrological proxies in peatlands* (Booth, R. K., & Sullivan, M. E. 2007), *An atlas of freshwater testate amoebae* (Ogden, G. G., & Hedley, R. H., 1980), *Microworld, world of amoeboid organisms* (Siemensma, F. J., 2019) and *Freshwater algae of North America: ecology and classification* (Wehr et al., 2015). Taxa were assigned to two assemblage groups based on dominant ecological strategy. The heterotrophic protist assemblage (hereafter protist assemblage) included testate amoebae (50 taxa; Figure 12; 1-5, 9-15, 17-18). Although some testate amoeba genera harbour endosymbiotic algae and exhibit facultative mixotrophy (Jassey et al., 2015), the taxa dominating our samples—including *Centropyxis*, *Difflugia*, *Arcella*, *Trinema*, and *Phryganella*—are predominantly heterotrophic bacterivores (Wilkinson and Mitchell, 2010). The phototrophic assemblage (hereafter phototroph assemblage) included diatoms, green algae, cyanobacteria, and xanthophytes (20 taxa; Figure 12; 6-8, 16). These groupings capture dominant ecological tendencies; they do not imply strict trophic exclusivity.

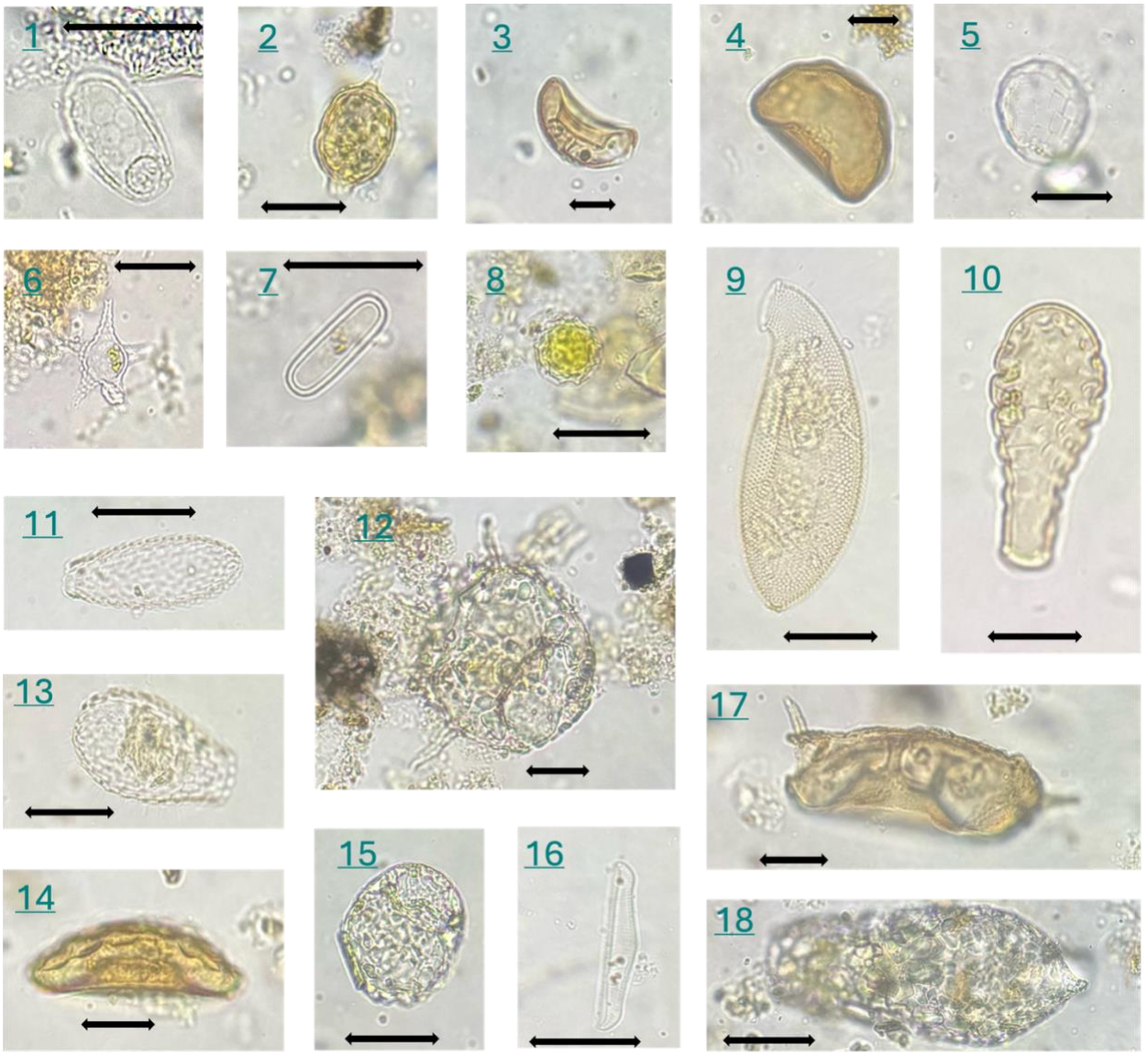

Figure 12. Plates of some testate amoebae, green algae and diatoms observed across sites. (1) *Trinema* spp. type (2) *Ditrema mikrous* (3) *Arcella discoides* type (4) *Arcella hemisphaerica* (5) *Paraquadrula irregularis* (6) *Staurastrum* spp. (7) Mesotaeniaceae (8) *Trochiscia reticularis* (9) *Cyphoderia ampull*a (10) *Hyalospenia elegans* (11) *Euglypha rotunda* (12) *Centropyxis aculeata* (13) *Euglypha spinosa* (14) *Galeripora catinus* (15) *Centropyxis cassis* (16) *Rhopalodia* spp. (diatom) (17) *Centropyxis discoides* (18) *Difflugia umbilicate.* Scale bar=20 microns.

3.2.3 Environmental Predictors

Environmental predictors included dissolved methane, carbon dioxide, and nitrous oxide concentrations (µmol L^{-1}); dissolved organic carbon (DOC; mg L^{-1}); dissolved nitrogen (DN; mg L^{-1}); seasonal water-table variability (standard deviation of water-table position; April–October;

cm); and pH. All variables represent growing season means corresponding to the microbiota sampling window. For variation partitioning, predictors were grouped into three ecologically distinct categories: dissolved gases (CH_4, CO_2, N_2O), dissolved carbon/nitrogen pools (DOC, DN), and hydrologic variability (water-table SD).

3.2.4 Field Methods

3.2.4.1 Water table measurements and sample collection

Water table gages made from PVC pipes perforated at one end were installed in advance. These were inserted 30 cm into the soil and 10 cm away from the collars facing N. The water table gage is at least 50 cm above the highest water level and graduated (cm) so that it is available to use as a collar and water level marker during winter when the wetlands are frozen, and the collar is inaccessible. When the water table was above the ground surface, depth was measured by placing a metre stick along the sediment surface beside the water table gauge and recording the height of the water level relative to the gauge itself. When the water table was below the ground surface, a vinyl tube was inserted into the PVC pipe well and air was gently blown through the tube until bubbling was detected. The length of tubing inserted into the PVC well was then measured, and the water table depth was calculated by subtracting the height of the PVC pipe above the ground surface. To collect water samples, a vinyl tube attached to a stopcock and a 100ml syringe was inserted into the PVC pipe. For dissolved organic C (DOC) and dissolved nitrogen (DN) analyses, 50ml conical tubes were filled and processed within 2 hours of the sampling event.

3.2.4.2 Water samples for dissolved gas

To collect samples for dissolved gas, a 100ml syringe was attached to a 3-way stopcock and a 10in 14gauge needle to prevent contamination. 30ml of headspace air was drawn into the syringe

from above the water surface, then the needle was placed underwater and 70ml of water was collected. The stopcock was closed, needle removed, and the syringe was shaken lightly for two minutes being held along where the plunge enters so to not influence the temperature of the sample. Then a 30ml transfer syringe was attached to the side port of the 3-way stopcock and the plunger of the 100ml syringe was depressed filling the 30ml transfer syringe with the dissolved gas sample ensuring that no water entered the transfer syringe. Lastly, the 100ml syringe and stopcock were removed and a 27gauge needle was attached to the transfer syringe where the 30ml dissolved gas sample was pushed into a pre-evacuated Exetainer© vial.

3.2.5 Laboratory Methods

3.2.5.1 Dissolved organic C (DOC) and dissolved nitrogen (DN) analyses

Before processing, the water samples pH was measured using a VWR SP70P Symphony portable pH metre. Water samples (40 ml) were filtered through a vacuum pump and a 0.45 μm fiberglass filter. They were then acidified with 1 N HCl to a pH of 2 and analyzed for DOC and DN concentration by a Shimadzu 5050 Analyzer.

3.2.5.2 Gas chromatograph measurements and calculations of dissolved gas concentrations

Gas samples were analyzed on a gas chromatograph (GC-14, Shimadzu, Kyoto, Japan) fitted with a methanizer to convert CO_2 to CH_4, a flame ionization detector (FID) for CH_4, and an electron capture detector (ECD) for N_2O. The FID operated at 250°C and the ECD at 325°C. Standards of N_2O (21.9 ppm), CH_4 (5.1 ppm), and CO_2 (5,000 ppm) yielded accuracies and precisions of ±0.3 ppm, ±0.4 ppm, and ±78 ppm, respectively. Headspace gas concentrations were converted to mass fluxes (mg m^{-2} h^{-1}) using the ideal gas law, chamber volume, and incubation time.

Dissolved concentrations of CO_2, CH_4, and N_2O were determined using a headspace equilibration method following gas chromatography (GC) analysis. Gas concentrations measured in the sample headspace (ppm) were converted to partial pressures using atmospheric pressure. The number of moles of gas in the headspace was calculated using the ideal gas law:

$$n_{air} = P_{gas}V_{air}/RT$$

where P_{gas} is the partial pressure of the gas, V_{air} is the headspace volume, R is the universal gas constant, and T is temperature in kelvin. The concentration of gas remaining dissolved in the water phase was calculated using Henry's Law:

$$C_{water} = k_H P_{gas}$$

where k_H is the temperature-specific Henry's law constant. Total gas content was calculated as the sum of gas in the headspace and dissolved in the water, converted to mass using gas-specific molar masses, and normalized to water volume to obtain concentrations (mg L^{-1}).

3.2.6 Atmospheric Gas Fluxes

Atmospheric CO_2, CH_4, and N_2O fluxes (mg m^{-2} h^{-1}) were measured using static chamber methods as described in Chapter 2 (Haak, 2026; Magenheimer et al., 1996; Chmura et al., 2016). Flux values represent growing season mean rates for each chamber. Standard deviations were retained for descriptive purposes but were not incorporated into regression models.

3.2.7 Statistical Workflow and Data Preparation

To address the objectives of this chapter, a structured statistical workflow was implemented, integrating data preparation, multivariate ordination, and regression-based analyses to link microbial community structure, environmental gradients, and greenhouse gas fluxes (Figure 13).

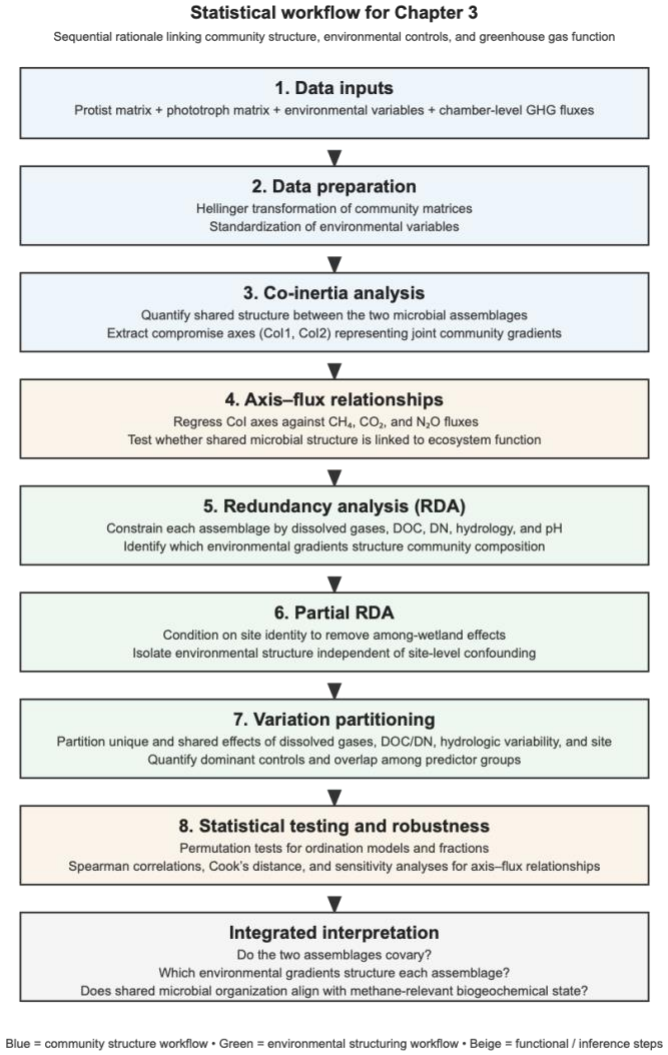

Figure 13. Statistical workflow used in Chapter 3. Community matrices were first transformed and analyzed using co-inertia analysis to quantify shared structure between heterotrophic protist and phototrophic assemblages. Compromise axes were then related to greenhouse gas fluxes to test functional relevance. Redundancy analysis and partial redundancy analysis were used to identify environmental gradients structuring each assemblage, while variation partitioning quantified the unique and shared contributions of dissolved gases, dissolved carbon/nitrogen pools, hydrologic variability, and site identity. Permutation tests and sensitivity analyses were used to evaluate robustness throughout the workflow.

3.2.8 Data Transformation

Community abundance matrices were Hellinger-transformed prior to ordination (Legendre and Gallagher, 2001). This transformation divides each species count by the row total and takes the square root, reducing the influence of highly abundant taxa and yielding Euclidean distances that approximate the Hellinger distance.

3.2.9 Redundancy Analysis

Partial redundancy analysis (RDA) was used to evaluate relationships between each assemblage and the environmental predictor set, with site identity included as a conditioning variable to remove among-wetland effects (Legendre and Legendre, 2012). Significance of constrained axes was assessed by permutation (9,999 permutations restricted within site blocks). Marginal (Type II) tests evaluated the contribution of individual predictors after accounting for all others. Variance inflation factors (VIF) were calculated to assess multicollinearity. DOC (VIF = 16.4) and DN (VIF = 10.5) exceeded conventional thresholds; individual predictor vectors involving these variables are therefore interpreted cautiously, although their collinearity does not affect the group-level variation partitioning. Analyses were performed using the *vegan* package in R (Oksanen et al., 2022).

3.2.10 Variation Partitioning

Variation partitioning (Borcard et al., 1992; Peres-Neto et al., 2006) was used to quantify unique and shared contributions of four predictor groups to community structure: (X1) dissolved gases, (X2) dissolved carbon/nitrogen pools, (X3) hydrologic variability, and (X4) site identity. DOC and DN were grouped into a single predictor set (X2) in part to mitigate the elevated collinearity between these variables (VIF = 16.4 and 10.5, respectively); grouping ensures that their shared variance is partitioned collectively rather than attributed to either variable alone, and the

collinearity does not affect group-level fractions. This four-way partition yields 15 fractions plus residuals. Adjusted R^2 values were used to avoid overestimation of explained variance. Unique fractions (each group conditioned on all others) were tested for significance by permutation (9,999 permutations). pH and maximum water-table depths were excluded from this analysis because they were non-significant in marginal tests for both assemblages and contributed to collinearity.

3.2.11 Co-inertia Analysis

Co-inertia analysis (Dolédec and Chessel, 1994) was used to quantify shared multivariate structure between the protist and phototroph assemblages. This method finds pairs of axes that maximize covariance between two multivariate datasets, providing a measure of cross-table coupling unconstrained by environmental predictors. The RV coefficient (Robert and Escoufier, 1976) was calculated to measure overall coupling strength, with significance assessed by 9,999 permutations restricted within site blocks. Compromise axis scores (CoI1 and CoI2) were retained for subsequent analyses. Within-site correlations between compromise axes and environmental variables were tested using blocked Spearman permutation tests.

3.2.12 Axis–Flux Relationships

Multiple linear regression was used to test associations between compromise axes (CoI1 and CoI2 as joint predictors) and atmospheric fluxes (CO_2, CH_4, N_2O). Model fit was assessed using R^2, adjusted R^2, F-statistics, and p-values. Spearman rank correlations were computed to evaluate monotonic relationships independent of distributional assumptions. Influence diagnostics were conducted using Cook's distance (threshold = 4/n; Cook, 1977). Sensitivity analyses were performed by refitting models after excluding influential observations. Given the modest sample size (n = 24, df = 21 for two-predictor models), we emphasize effect direction, consistency

across parametric and non-parametric frameworks, and sensitivity to influential points. All analyses were conducted in R v. 4.5.2 (R Core Team, 2026) using RStudio (Posit Team, 2025).

3.3 Results

3.3.1 Site Characteristics

Environmental conditions differed substantially among sites (Table 2). Circle Park exhibited the highest dissolved CH_4 (13.3 ± 13.8 µmol L^{-1}) and highest atmospheric CH_4 flux (79.5 ± 106.3 mg m^{-2} h^{-1}). Cawthra Mulock had the lowest dissolved CH_4 (1.7 ± 0.9 µmol L^{-1}) and negligible atmospheric CH_4 flux (1.3 ± 2.1 mg m^{-2} h^{-1}). Beaver River had the highest dissolved CO_2 and DOC concentrations and showed moderate mean CH_4 flux (31.4 ± 58.4 mg m^{-2} h^{-1}), though with high among-chamber variability. Hydrologic variability was greatest at Cawthra Mulock (WT SD = 27.3 ± 5.8 cm) and lowest at Beaver River (9.5 ± 2.4 cm). CO_2 fluxes were broadly similar across sites (337–463 mg m^{-2} h^{-1}). N_2O fluxes were near zero across all sites.

Table 2. Site characteristics and environmental summary. Values are mean ± SD across chambers within each site.

Variable	Cawthra Mulock (n = 11)	Circle Park (n = 9)	BRW (n = 4)
Dissolved CH_4 (µmol/L)	1.69 ± 0.88	13.26 ± 13.84	6.64 ± 4.57
Dissolved CO_2 (µmol/L)	94.2 ± 31.9	245.2 ± 161.3	345.7 ± 124.5
Dissolved N_2O (µmol/L)	0.012 ± 0.002	0.013 ± 0.003	0.012 ± 0.002
DOC (mg/L)	8.14 ± 1.22	11.77 ± 2.20	18.11 ± 2.27
DN (mg/L)	0.41 ± 0.07	0.49 ± 0.06	0.68 ± 0.19
Water table SD (cm)	27.3 ± 5.8	16.0 ± 2.7	9.5 ± 2.4
pH	7.27 ± 0.14	7.28 ± 0.18	6.93 ± 0.27
CO_2 flux (mg/m²/h)	403.7 ± 138.0	462.6 ± 227.8	336.4 ± 386.7

CH_4 flux (mg/m²/h)	1.28 ± 2.07	79.51 ± 106.32	31.4 ± 58.4
N_2O flux (mg/m²/h)	0.042 ± 0.098	−0.021 ± 0.033	−0.048 ± 0.123

3.3.2 Environmental Structuring of Individual Assemblages

Partial RDA, conditioned on site, revealed significant overall environmental structuring of both assemblage groups (Table 3; Figure 14 and 15). The protist assemblage model explained significant constrained variation (F = 1.449, p = 0.028), as did the phototroph assemblage model (F = 1.638, p = 0.034).

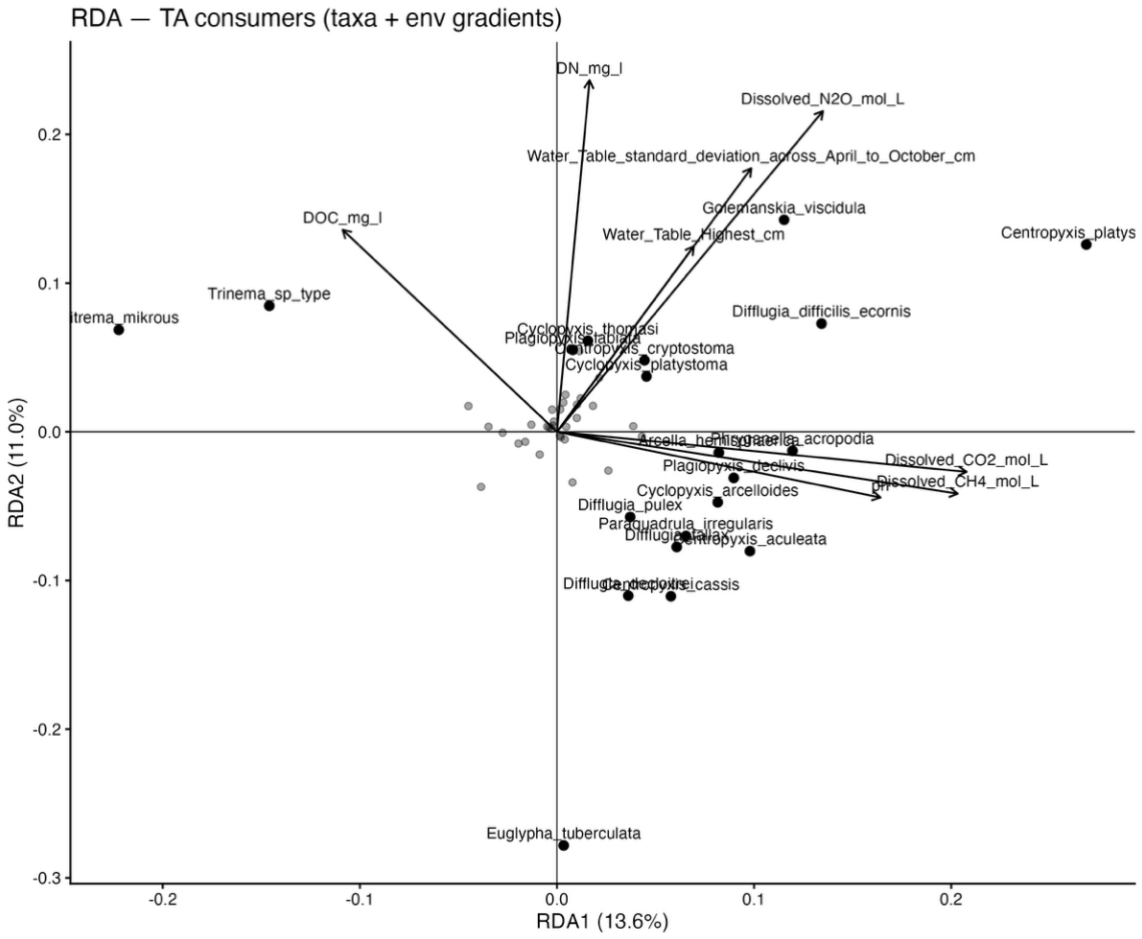

Figure 14. Partial redundancy analysis (RDA) biplot of the heterotrophic protist assemblage, conditioned on site identity. Points represent taxa (top 20 by vector length labeled); arrows represent environmental predictor gradients (scaling 2). RDA1 and RDA2 explain 13.6% and 11.0% of constrained variation,

respectively. Dissolved CH_4 and CO_2 project strongly along the primary axis, with large-bodied testate amoeba taxa (*Centropyxis platystoma*, *Difflugia difficilis ecornis*, *Phryganella acropodia*) oriented toward elevated dissolved gas conditions, and *Ditrema mikrous* and *Trinema* sp. in the opposing direction. DOC projects opposite to dissolved gases along RDA1, while DN and dissolved N_2O load on RDA2. Arrow direction and length indicate each predictor's correlation with the constrained axes — not its unique statistical contribution.

Variation partitioning (Table 4) indicates that the dissolved gas gradient visible in Figure 14 is largely confounded with site identity (unique fraction: adj. $R^2 = 0.002$, $p = 0.431$); the alignment of taxa with dissolved gas conditions may therefore reflect among-site compositional differences rather than independent within-site responses. The global model was significant ($F = 1.449$, $p = 0.028$), but no individual predictor reached significance in marginal tests (Table 3).

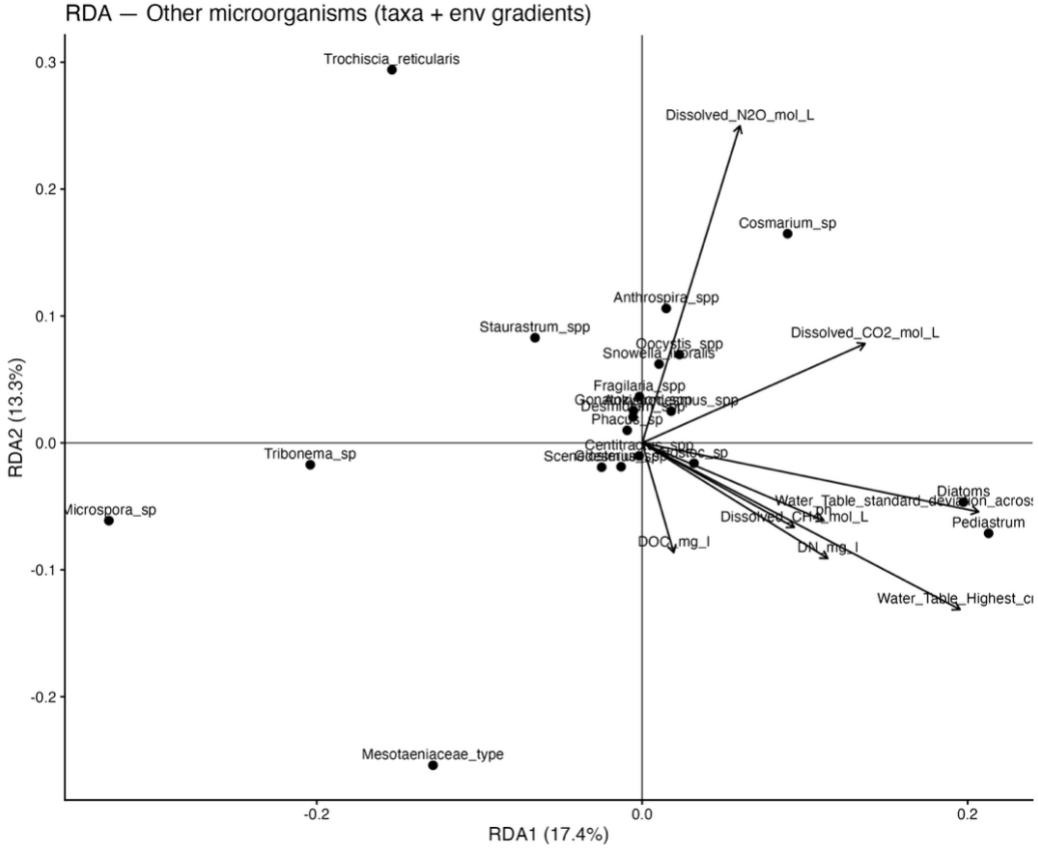

Figure 15. Partial redundancy analysis (RDA) biplot of the phototrophic assemblage, conditioned on site identity. Hydrologic predictors (water-table SD and water-table maximum) project prominently along the

primary axis, with dissolved N_2O loading strongly on the secondary axis. *Pediastrum* and diatoms are associated with higher water-table conditions; *Microspora* sp. and *Tribonema* sp. orient in the opposing direction, and *Trochiscia reticularis* loads on the N_2O-associated secondary axis.

However, marginal tests—which evaluate each predictor's unique contribution after accounting for all others—revealed that no individual predictor was statistically significant for the protist assemblage (all $p > 0.05$; Table 3). For the phototroph assemblage, dissolved CO_2 ($F = 1.729$, $p = 0.031$) and dissolved N_2O ($F = 2.020$, $p = 0.050$) were the only individually significant marginal terms. This indicates that the environmental signal in the protist assemblage is collective rather than attributable to any single predictor, whereas the phototroph assemblage shows more specific responses to individual dissolved gas gradients.

In the protist RDA biplot, dissolved CH_4 and CO_2 projected strongly along the primary constrained axis, with taxa such as *Centropyxis platystoma*, *Difflugia difficilis ecornis*, *Phryganella acropodia*, and *Golemanskia viscidula* aligned with elevated dissolved gas conditions (Figure 14). *Ditrema mikrous* and *Trinema* sp. oriented toward lower dissolved gas conditions. In the phototroph biplot, hydrologic variability and water-table position contributed prominently to axis structure, with *Pediastrum* and *Cosmarium* sp. associated with higher water-table conditions and *Microspora* sp. and *Tribonema* sp. in the opposing direction (Figure 15)

Table 3. Partial RDA summary statistics. Global model tests and marginal (Type II) tests for individual predictors, with variance inflation factors (VIF). Models conditioned on site identity. Significance: * $p < 0.05$.

	Df	**Var.**	**F**	**p**	**Var.**	**F**	**p**	**VIF**
		Protist			Phototroph			
Global model	8	0.114	1.449	0.028*	0.076	1.638	0.034*	—
Dissolved CH_4	1	0.011	1.073	0.388	0.006	0.983	0.465	6.3
Dissolved CO_2	1	0.009	0.930	0.510	0.010	1.729	0.031*	6.5

Dissolved N_2O	1	0.011	1.072	0.396	0.012	2.020	0.050*	1.8
DOC	1	0.013	1.272	0.260	0.009	1.520	0.216	16.4
DN	1	0.008	0.837	0.647	0.005	0.934	0.440	10.5
WT max	1	0.016	1.627	0.162	0.006	0.989	0.495	4.9
WT SD	1	0.016	1.583	0.096	0.008	1.328	0.272	4.7
pH	1	0.010	1.003	0.458	0.005	0.820	0.574	2.6
Residual	13	0.128			0.075			

3.3.3 Variation Partitioning

Four-way variation partitioning (dissolved gases, DOC/DN, hydrologic variability, and site identity) revealed contrasting patterns between the two assemblages (Table 4; Figure 16 and 17).

For the protist assemblage, unique environmental fractions were uniformly small: dissolved gases explained 0.2% ($p = 0.431$), DOC/DN 1.4% ($p = 0.218$), and hydrologic variability 1.9% ($p = 0.077$) of variation after controlling for all other groups and site. Site identity accounted for the largest unique fraction (16.1%). Substantial shared fractions between environmental groups and site (particularly gases×site = 9.1% and a three-way gas×DOC/DN×site fraction of 9.7%) indicate that the protist assemblage's environmental signal is largely confounded with site identity.

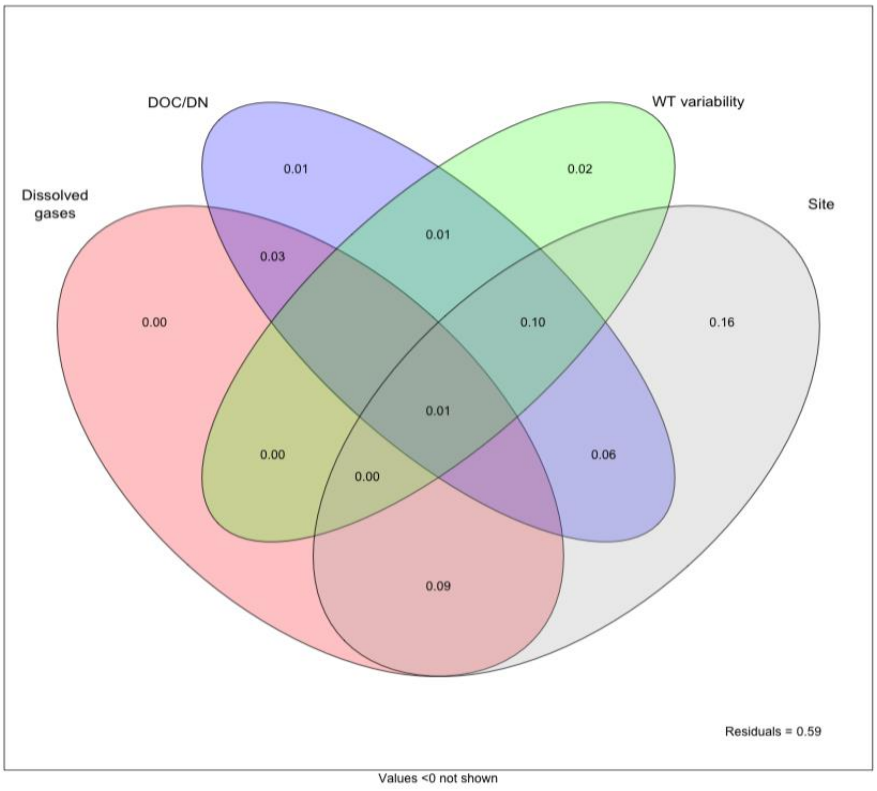

Figure 16. Four-way variation partitioning of the heterotrophic protist assemblage. Venn diagram shows adjusted R^2 fractions for dissolved gases (CH_4, CO_2, N_2O), dissolved carbon/nitrogen pools (DOC, DN), hydrologic variability (water-table SD), and site identity. Values < 0 not shown. Unique environmental fractions are uniformly small (dissolved gases: 0.00; DOC/DN: 0.01; WT variability: 0.02; nonsignificant at $p < 0.05$). The largest fractions are unique site (0.16) and shared environment × site intersections (dissolved gases × site = 0.09; dissolved gases × DOC/DN × site = 0.10). Residuals = 0.59.

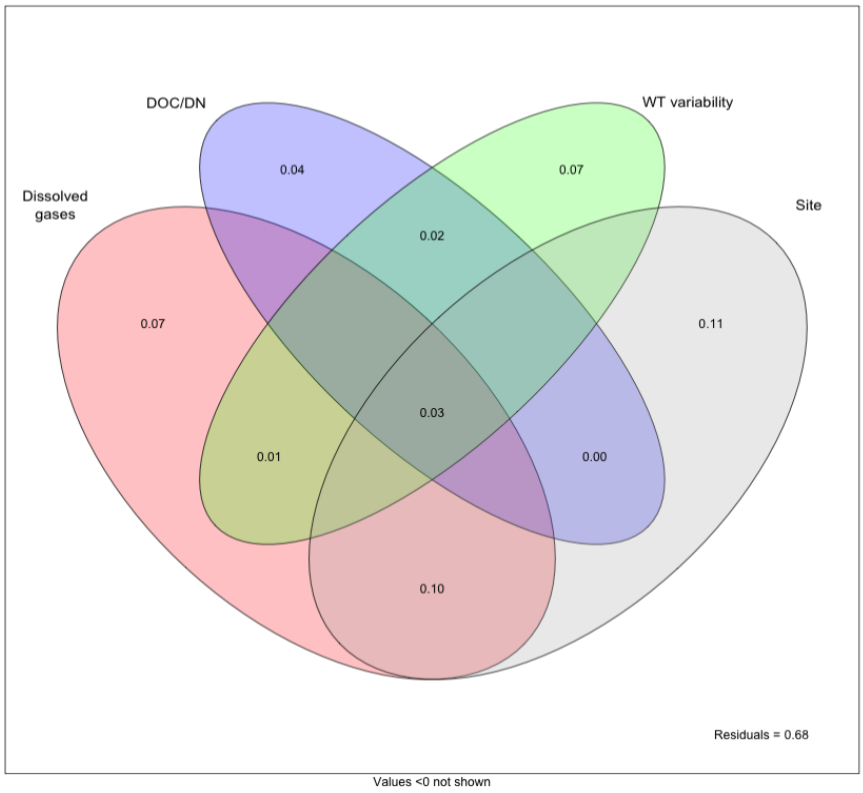

Figure 17. Four-way variation partitioning of the phototrophic assemblage. Unique environmental fractions are larger and more evenly distributed than for the protist assemblage: dissolved gases = 0.07 (p = 0.066), WT variability = 0.07 (p = 0.015), DOC/DN = 0.04 (p = 0.140). Residuals = 0.68.

For the phototroph assemblage, unique environmental fractions were larger and more evenly distributed. Dissolved gases explained 7.2% of unique variation (p = 0.066, borderline), and hydrologic variability explained 7.0% (p = 0.015, significant). DOC/DN contributed 3.7% (p = 0.140). Site accounted for 11.2% of unique variation, with smaller shared fractions than observed for the protist assemblage. The significant unique contribution of hydrologic variability indicates that phototroph community structure responds to water-table dynamics independently of dissolved gas gradients and site identity.

Table 4. Unique fractions from four-way variation partitioning (dissolved gases, DOC/DN, hydrologic variability, and site identity). Adjusted R^2 values shown. Unique fractions tested by permutation (9,999 permutations). Significance: * $p < 0.05$; † $p < 0.10$.

Predictor group	Adj. R^2	F	p	Adj. R^2	F	p
	Protist			Phototroph		
Dissolved gases	0.002	1.020	0.431	0.072	1.635	0.066†
DOC / DN	0.014	1.198	0.218	0.037	1.460	0.140
WT variability	0.019	1.520	0.077†	0.070	2.643	0.015*
Site	0.161	—	—	0.112	—	—
Residual	0.592			0.683		

3.3.4 Cross-Assemblage Coupling

Co-inertia analysis yielded an RV coefficient of 0.644 ($p = 0.008$; 9,999 permutations restricted within site blocks), indicating strong shared structure between the two community matrices. The first compromise axis (CoI1) separated CP (Circle Park) chambers (positive scores) from CM (Cawthra Mulock) and BRW (Beaver River) chambers (negative scores); the second axis (CoI2) further distinguished Beaver River from the two constructed wetlands. Within-site blocked permutation tests identified a significant positive association between CoI1 and dissolved organic carbon (Spearman $r = 0.36$, $p = 0.034$; Table 5). No other environmental variable exhibited a statistically significant within-site association with either compromise axis, although several showed moderate non-significant correlations (e.g., CoI1 vs. dissolved CH_4: $r = 0.42$, $p = 0.832$; CoI2 vs. DOC: $r = -0.82$, $p = 0.118$).

Table 5. Spearman correlations between co-inertia compromise axes and environmental variables. P-values from within-site blocked permutation tests (9,999 permutations). Significance: * $p < 0.05$.

Variable	CoI1 r	p	CoI2 r	p	n
DOC (mg/L)	0.360	0.034*	−0.817	0.118	24

Dissolved CH_4	0.423	0.832	−0.640	0.336	24
Dissolved CO_2	0.313	0.512	−0.743	0.146	24
DN (mg/L)	0.210	0.341	−0.673	0.107	24
Dissolved N_2O	0.136	0.309	−0.119	0.347	24
WT max (cm)	0.214	0.562	0.277	0.798	24
WT SD (cm)	−0.228	0.840	0.690	0.914	24
pH	0.060	0.984	0.217	0.315	24

3.3.5 Hydrologic Subset Analysis

Coupling strength differed numerically between hydrologic subsets: RV = 0.581 (wet, n = 12) versus RV = 0.840 (dry, n = 12), but the difference was not statistically significant (permutation test, p = 0.130). Given that all BRW (Beaver River) chambers fell within the dry group, this contrast is partially confounded with site identity.

3.3.6 Compromise Axis–Flux Relationships

Results from regression and correlation analyses linking compromise axes to atmospheric fluxes are summarized in Table 6.

Table 6. Compromise axis–atmospheric flux relationships. Multiple linear regression (Flux ~ CoI1 + CoI2) and Spearman rank correlations. Sensitivity models exclude chambers exceeding Cook's distance threshold (4/n). Significance: *p < 0.05;* * p < 0.01.

Gas	n	R^2	Adj R^2	F (2,21)	p	Signif. axis	ρ CoI1	p	ρ CoI2	Sensitivity
CH_4	24	0.217	0.143	2.918	0.076	CoI1 (p = 0.026)	0.57	0.005**	−0.31	n = 22: p = 0.056
CO_2	24	0.038	−0.054	0.411	0.668	—	0.15	0.494	−0.01	—

N_2O	24	0.364	0.303	6.007	0.009**	CoI2 (p = 0.003)	−0.10	0.653	0.12	n = 22: p = 0.428

Methane (CH_4)

The parametric model was not significant at the conventional threshold ($p = 0.076$), although CoI1 was individually significant within the model ($\beta = 7.60 \pm 3.17$ SE; $p = 0.026$). The Spearman rank correlation revealed a significant positive monotonic association ($\rho = 0.57$, $p = 0.005$; Figure 18). This discrepancy between parametric and non-parametric results reflects the well-known spatial heterogeneity of wetland methane emissions: two high-flux CP chambers (CPGHG2 and CPGHG4; Cook's $D > 4/n$) create heteroscedasticity that weakens the linear fit. Importantly, the sensitivity analysis excluding these chambers improved the parametric model toward significance ($n = 22$, $R^2 = 0.262$, $p = 0.056$), confirming that the non-linearity of the response—not the absence of a relationship—drives the overall parametric non-significance. The strong Spearman result, which is robust to such distributional effects, provides the most reliable evidence for the CH_4–CoI1 association. To further assess the robustness of this relationship across analytical frameworks, the model was evaluated using log-transformed OLS, robust regression (Huber M-estimator), and Spearman rank correlation alongside the original parametric model. Log-transformation required a shift constant of 18.3 to accommodate one chamber with net negative mean CH_4 flux and did not improve model fit or residual normality ($F(2, 21) = 1.32$, $p = 0.289$; Shapiro–Wilk $W = 0.73$, $p < 0.001$), indicating that this transformation is inappropriate for the strongly right-skewed and zero-inflated distribution of wetland CH_4 emissions. However, robust regression—which downweighs high-leverage observations rather than transforming the response—confirmed a highly significant CoI1 effect ($t = 7.60$, $p < 0.001$),

and the Spearman rank correlation was significant ($\rho = 0.57$, $p = 0.005$). Within the original OLS framework, CoI1 was individually significant ($\beta = 7.60$, $p = 0.026$) despite the overall model not reaching conventional significance ($p = 0.076$). Together, these results indicate that the CH_4–CoI1 association is robust across non-parametric and robust-estimation frameworks and that the borderline overall parametric significance reflects distributional properties of wetland CH_4 emissions—specifically, high-leverage observations at the permanently flooded site—rather than the absence of a genuine community–flux relationship.

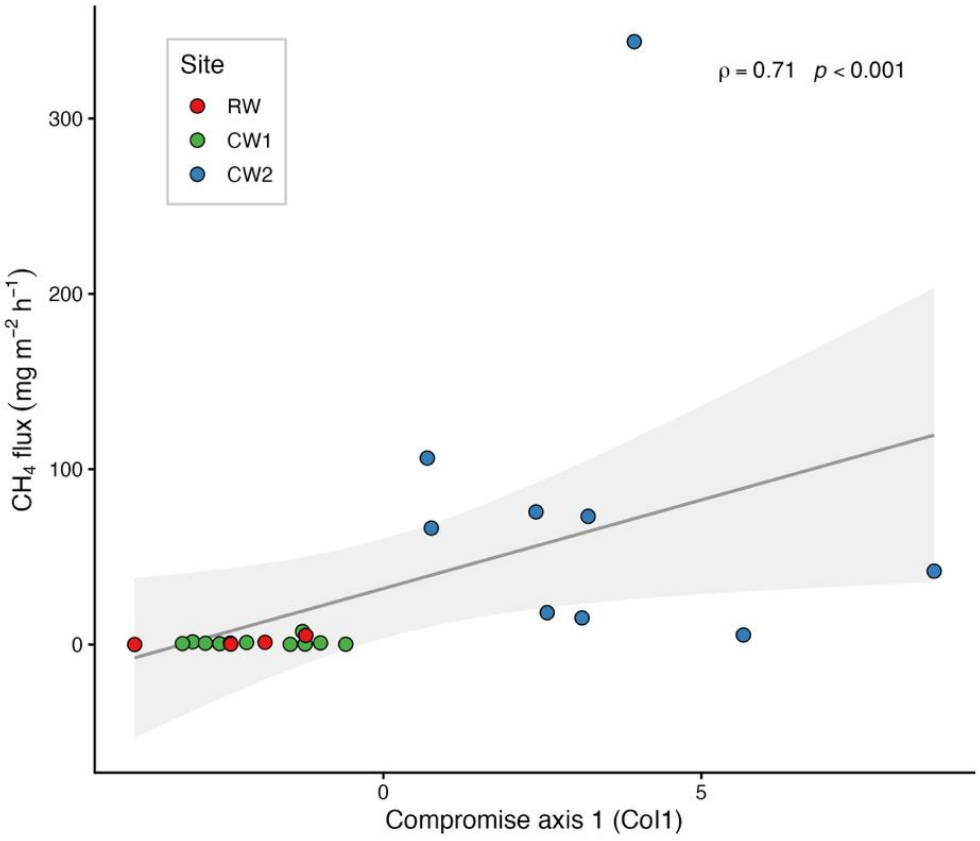

Figure 18. Relationship between the primary co-inertia compromise axis (CoI1) and atmospheric methane flux (growing season mean). Points are colored by site (CW1 = Cawthra Mulock, green; CW2 = Circle Park, blue; BRW = Beaver River, red). The line and shaded region show the linear regression fit ± 95% confidence interval. Spearman rank correlation confirmed a significant positive monotonic association ($\rho = 0.57$, $p = 0.005$). Note that CoI1 scores are derived entirely from community composition data via co-inertia analysis, independent of flux measurements, making this an unconstrained community–ecosystem association.

Carbon dioxide (CO_2)

The model was not significant ($R^2 = 0.038$, $p = 0.668$). Neither compromise axis predicted CO_2 flux, and Spearman correlations were non-significant. The near-zero explained variance underscores the absence of any detectable community–CO_2 flux relationship.

Nitrous oxide (N_2O)

The parametric model was significant ($p = 0.009$), with CoI2 as the predictor ($\beta = 0.021 \pm 0.006$ SE; $p = 0.003$). However, this result failed both robustness checks: Spearman correlations for N_2O with both axes were non-significant, and excluding two high-leverage chambers collapsed the model ($n = 22$, $p = 0.428$). This association is not robust and likely reflects the influence of one or two site-specific chambers rather than a generalizable community–flux linkage.

3.4 Discussion

3.4.1 Cross-Assemblage Coupling and Shared Biogeochemical Organization

This study provides exploratory evidence that heterotrophic protist and phototrophic soil microbiota assemblages in mineral-soil wetlands are organized along shared environmental gradients (RV = 0.644, $p = 0.008$). The within-site association between the primary compromise axis and DOC suggests that this shared structure reflects biogeochemical state rather than site identity alone. In constructed wetland systems, hydrologic regime, redox dynamics, and carbon availability are tightly interlinked (Kadlec and Wallace, 2009), and the co-inertia results indicate that both assemblage groups respond to these integrated gradients.

3.4.2 Asymmetric Environmental Structuring

A central finding of this study is that the two assemblage groups differ in how cleanly their environmental signals can be separated from site identity. Variation partitioning revealed that the protist assemblage's environmental signal is largely confounded with site: unique environmental fractions were negligible (dissolved gases: adj. $R^2 = 0.002$; DOC/DN: 0.014; hydrologic variability: 0.019), while large, shared fractions between environment and site indicate that these influences cannot be disentangled. This does not mean that protist communities are unresponsive to environmental conditions; rather, the environmental gradients that structure protists covary tightly with among-site differences at the spatial scale of this study.

The phototroph assemblage, by contrast, showed a cleaner environmental signal. Hydrologic variability emerged as a statistically significant unique predictor (adj. $R^2 = 0.070$, $p = 0.015$), and dissolved gases were borderline significant (adj. $R^2 = 0.072$, $p = 0.066$). These results indicate that phototroph community structure responds to water-table dynamics and dissolved gas gradients independently of site identity. Ecologically, diatoms, green algae, and cyanobacteria respond to light penetration, nutrient availability, and hydroperiod stability (Stevenson et al., 1996; Van Dam et al., 1994), factors that vary within as well as among sites.

The marginal RDA tests further reinforced this asymmetry: dissolved CO_2 and N_2O were individually significant for phototrophs but not for protists. The collective significance of the protist model ($p = 0.028$) despite no individually significant predictors suggests that multiple correlated gradients act in concert, consistent with testate amoebae responding to composite sediment conditions rather than any single environmental driver (Mitchell et al., 2008).

3.4.3 Methane Flux Aligns with Shared Community Structure

The most notable ecosystem-level result was the strong association between CoI1 and atmospheric methane flux, confirmed across multiple analytical frameworks. The Spearman rank correlation was significant ($\rho = 0.57$, $p = 0.005$), and robust regression (Huber M-estimator)—which downweights high-leverage observations without distributional assumptions—yielded the strongest evidence of all ($t = 7.60$, $p < 0.001$). Within the original OLS framework, CoI1 was individually significant ($\beta = 7.60$, $p = 0.026$) despite the overall model not reaching conventional significance ($p = 0.076$), and the sensitivity analysis excluding two high-leverage chambers improved the parametric fit ($p = 0.056$). Log-transformation was inappropriate for these data due to negative flux values requiring a large shift constant. The convergence of non-parametric, robust, and within-model parametric evidence indicates a genuine monotonic relationship that is obscured in the standard linear framework by the characteristically right-skewed and heteroscedastic distribution of methane flux in spatially heterogeneous wetlands (Bridgham et al., 2013).

Critically, CoI1 was derived from community data without reference to flux measurements. That a community-derived axis captures substantial variation in an independent biogeochemical response variable suggests that cross-assemblage microbial structure may encode information about methane-relevant ecosystem state. Because CoI1 captures the convergence between protist and phototroph assemblages, the methane signal appears to emerge from system-wide structural organization rather than from either assemblage alone.

CO_2 flux showed no detectable relationship with compromise axes ($R^2 = 0.038$). This clean separation between CH_4 and CO_2 responses is consistent with the distinct biogeochemical controls on these gases: methane production is tightly constrained by anaerobic redox conditions and labile carbon availability, whereas CO_2 integrates autotrophic uptake, heterotrophic

respiration, root respiration, and physical gas exchange (Segers, 1998; Bridgham et al., 2013). Methane may therefore represent a more specific atmospheric expression of the biogeochemical state captured by cross-assemblage community structure.

3.4.4 Extending Protist–Methane Frameworks Beyond Peatlands

These findings support the broader concept that protist assemblages track methane-relevant biogeochemical state. In Sphagnum peatlands, Jassey et al. (2015) showed that shifts in mixotrophic testate amoebae modulate carbon-cycle responses under warming, and transfer-function work has linked peat-archive testate amoeba assemblages to methane emissions (Davies et al., 2021; Fresard et al., 2023)**.** Our findings extend this framework into mineral-soil constructed wetlands and, importantly, show that cross-assemblage convergence—not individual assemblage composition alone—may carry the informative signal.

We emphasize that this analysis is exploratory and correlative. The variation partitioning results caution that protist–environment relationships are strongly confounded with site identity in this dataset. The methane–community link is mediated through a shared gradient that integrates information from both assemblages, making it robust to the limitations of either one in isolation—as evidenced by the strong Spearman association ($\rho = 0.57$, $p = 0.005$) and highly significant robust regression ($t = 7.60$, $p < 0.001$). Nonetheless, targeted functional measurements—including methanogenesis (*mcrA*) and methanotrophy (*pmoA*) molecular markers, bacterial prey field characterization, and protist grazing experiments—are needed to test causal pathways.

3.4.5 Nitrous Oxide: An Inconclusive Association

The parametric N_2O model was significant but failed both non-parametric confirmation and leverage stability. N_2O production involves complex, spatially heterogeneous nitrification–denitrification dynamics (Butterbach-Bahl et al., 2013). Given the limited sample size and uneven site representation, this result is inconclusive and likely reflects the influence of one or two site-specific chambers.

3.4.6 Hydrologic Modulation of Coupling Strength

Coupling strength was numerically higher under drier conditions (RV = 0.840 vs. 0.581), though not significantly so and partially confounded by site representation. Transitional redox states may amplify cross-assemblage responses by simultaneously influencing oxygen penetration, carbon mineralization, and microbial turnover (Mitchell et al., 2008). Balanced hydrologic replication across sites would be needed to evaluate this hypothesis.

3.4.7 Implications for Constructed Wetland Monitoring

These findings suggest that cross-assemblage microbial structure may offer an integrative indicator of methane-linked biogeochemical state. Conventional monitoring captures instantaneous physicochemical conditions, whereas microbial assemblages integrate environmental conditions over ecologically relevant timescales (Mitchell et al., 2008; Geisen et al., 2018). The asymmetry between CH_4 and CO_2 associations underscores that not all greenhouse gases respond equivalently to microbial structural gradients, and predictive frameworks should account for this gas-specific heterogeneity (Mander et al., 2014).

3.4.8 Limitations and Future Directions

Several limitations constrain inference. First, three wetlands and 24 chambers within a single season limit power and increase sensitivity to influential observations. Second, the protist

assemblage's environmental signal is confounded with site identity, precluding definitive attribution of community structure to specific environmental drivers. Third, DOC and DN showed elevated collinearity (VIF > 10), requiring cautious interpretation of their individual contributions. Fourth, time-integrated community samples preclude assessment of seasonal dynamics.

Future studies should incorporate: (a) multi-year sampling across additional sites to disentangle site from environment; (b) molecular functional markers (*mcrA*, *pmoA*) to test mechanistic pathways; (c) balanced hydrologic replication; (d) experimental water-level manipulation; and (e) bacterial community profiling to characterize the prey fields linking protist assemblages to methane-producing networks. Despite these limitations, the methane–CoI1 association, confirmed across Spearman rank correlation ($\rho = 0.57$, $p = 0.005$) and robust regression ($t = 7.60$, $p < 0.001$), supports further investigation of cross-assemblage microbial structure as an integrative indicator of wetland greenhouse gas dynamics.

CHAPTER 4: CONCLUSIONS

4.1 Chapter 2 Conclusions

This study suggests that hydrologic regime exerts dominant control over methane emissions and integrated climatic forcing in wetlands with emergent *Typha* vegetation, overriding the effects of both wetland origin (constructed versus natural) and substrate type (mineral versus organic soil). Permanently flooded conditions on mineral soil supported sustained CH_4 emissions across all seasons, including winter, with methane contributing up to 82% of total CO_2-equivalent forcing. In contrast, seasonal drawdown on mineral soil substantially suppressed CH_4 emissions despite

comparable summer temperatures, and a natural marsh on organic soil (~37% OC) produced only intermediate CH_4 fluxes under shallower and more variable inundation.

CO_2 fluxes were strongly modulated by soil temperature and exhibited clear seasonal and diurnal structure, but temperature alone did not explain site-level differences in CH_4 emissions. Instead, CH_4 fluxes were contingent upon hydrologic state, reinforcing a hierarchical control framework in which hydrology governs redox conditions and methanogenic potential while temperature modulates flux magnitude. N_2O fluxes were consistently small and episodic, contributing negligibly to integrated forcing.

These findings have direct relevance for the assessment and design of constructed mineral-soil wetlands as nature-based climate solutions. Emission factors derived from wastewater treatment constructed wetlands or peatlands are unlikely to be appropriate for habitat-oriented systems on mineral soils, whose GHG dynamics are governed primarily by hydroperiod. The depth and duration of inundation—not substrate carbon content or construction history—emerged as the strongest predictor of methane emissions and integrated warming potential. The presence of measurable winter CH_4 emissions at permanently flooded sites highlights the importance of year-round monitoring and cautions against reliance on growing-season-only sampling for annual budget estimation. Because fluxes were measured using opaque chambers, the CO_2-equivalent values reported here represent the warming potential of gaseous effluxes (ecosystem respiration + CH_4 + N_2O) and do not constitute a net ecosystem radiative balance. Preliminary biomass data from these sites (Pendea, unpublished data) indicate that all three wetlands support substantial vegetative carbon assimilation by *Typha* stands, with multiannual dry biomass reaching ~6,900 g m^{-2} CO_2-equivalent at BRW, 2,800 g m^{-2} CO_2-equivalent at CP, and 1,400 g m^{-2} CO_2-equivalent at CM. This means that the net climatic impact is less than the emission-side estimates alone

imply. A complete assessment integrating photosynthetic uptake with gaseous effluxes—using transparent chambers or eddy covariance—is an important next step. Overall, these findings suggest that hydrologic design—particularly decisions regarding water-level management—should be central to climate-informed wetland construction and management in temperate regions. When contextualized against the temperate wetland literature, Circle Park's CH_4 emissions place it among the higher-emitting cattail-dominated systems, exceeding most published values for created and European CWs but remaining below the natural Mer Bleue cattail marsh (Bonneville, 2006), while Cawthra Mulock and Beaver River align with the lower end of reported values for freshwater wetland systems and prairie waterbodies.

4.2 Chapter 3 Conclusions

This exploratory study supports the interpretation that heterotrophic protist and phototrophic microbial assemblages in mineral-soil constructed wetlands converge along shared environmental gradients, and that this convergence aligns with atmospheric methane flux. The association between the primary compromise axis and CH_4 emission was confirmed across multiple analytical frameworks, including Spearman rank correlation ($\rho = 0.57$, $p = 0.005$), robust regression ($t = 7.60$, $p < 0.001$), and within-model parametric significance of CoI1 ($p = 0.026$), establishing this as the most robust ecosystem-level relationship detected. Carbon dioxide showed no detectable association ($R^2 = 0.038$), and a parametric N_2O result was not robust to diagnostics.

Variation partitioning revealed that environmental structuring differs between assemblages: phototroph communities show significant unique responses to hydrologic variability and borderline responses to dissolved gases, whereas protist environmental signals are confounded with site identity at this spatial scale. The methane signal emerges from cross-assemblage

convergence rather than from either group alone, suggesting that multivariate microbial community metrics may capture biogeochemical information that individual assemblages or individual predictors cannot.

While correlative, these findings extend protist–methane frameworks from peatlands into engineered mineral-soil systems and provide a foundation for targeted mechanistic studies of microbial community–greenhouse gas linkages in constructed wetlands.

4.3 Thesis Conclusions

Across both chapters, this research supports the interpretation that hydrologic regime is the primary driver in constructed and natural mineral-soil wetlands, shaping not only greenhouse gas emissions but also the structure and functional convergence of microbial communities associated with methane gradients.

Greenhouse gas measurements show that methane emissions are governed primarily by hydrologic state rather than wetland origin or substrate type. Permanently flooded mineral-soil wetlands sustained methane emissions across seasons, whereas seasonal drawdown substantially reduced methane flux despite comparable summer temperatures. Carbon dioxide exchange followed expected temperature-driven seasonal and diurnal patterns but did not explain site-level variability in methane emissions, reinforcing a hierarchical control structure in which hydrology regulates redox conditions and methanogenic potential.

Complementary microbial analyses revealed that heterotrophic protist and phototrophic microbial assemblages converge along shared environmental gradients that align with

methane flux, indicating that biological community structure reflects the same environmental controls governing greenhouse gas dynamics. The strongest ecosystem-level relationship detected was between microbial community convergence and methane emission—confirmed across Spearman rank correlation, robust regression, and within-model parametric tests—whereas carbon dioxide and nitrous oxide showed no robust associations. Environmental partitioning further suggested that phototrophic communities respond directly to hydrologic variability and dissolved gas conditions, while protist assemblages are more strongly structured by site identity at this spatial scale. The methane signal therefore emerges not from individual microbial groups alone, but from cross-assemblage convergence, implying that multivariate community metrics can capture integrated biogeochemical signals that single predictors or assemblages cannot. Together, these findings indicate that hydrology simultaneously regulates wetland greenhouse gas emissions, and the microbial community structure associated with methane cycling, linking physical wetland design to ecosystem-scale climate outcomes. For mineral-soil constructed wetlands developed as nature-based solutions, the depth and duration of inundation emerge as primary determinants of methane emissions and associated microbial dynamics, whereas substrate carbon content and construction history play secondary roles. The presence of sustained methane emissions under permanent inundation—including during winter—underscores the importance of year-round monitoring and highlights the need for hydrologically informed wetland design and management. It should be noted that the CO_2-equivalent estimates reported here reflect the warming potential of gaseous effluxes only and do not include photosynthetic carbon

uptake. Preliminary biomass data from these sites (Pendea, unpublished data) indicate that all three wetlands support substantial vegetative carbon assimilation by Typha stands, with multiannual dry biomass reaching ~6,900 g m^{-2} CO_2-equivalent at BRW, 2,800 g m^{-2} CO_2-equivalent at CP, and 1,400 g m^{-2} CO_2-equivalent at CM. The magnitude of this uptake suggests that the net ecosystem radiative balance may differ substantially from emission-side estimates alone, particularly at sites where high biomass productivity is combined with low methane emissions. A full integration of carbon uptake and gaseous effluxes remains an important direction for future work.

Collectively, this work supports the interpretation that integrating hydrologic controls with microbial community perspectives provides a more complete framework for understanding and predicting greenhouse gas dynamics, advancing both ecological understanding and the climatic impact of mineral-soil wetland construction as nature-based climate solutions in temperate regions.

References

Ansola, G., Arroyo, P., & de Miera, L. E. S. (2014). Characterisation of the soil bacterial community structure and composition of natural and constructed wetlands. *Science of the Total Environment*, *473*, 63-71.

Astuti, S. P., Hashmi, Z., Bilad, M. R., Payus, C. M., Affandi, M., & Soegianto, A. (2026). Freshwater Microalgae as Bioindicators: A Review of Trait-Based Advances, Ecosystem Insights, and Biomonitoring Innovations. *Environmental Challenges*, 101428.

Bansal, S., Johnson, O. F., Harber, J., & Chimner, R. A. (2020). Vegetation affects timing and location of wetland methane emissions. *Journal of Geophysical Research: Biogeosciences*, *125*(9), e2020JG005777. https://doi.org/10.1029/2020JG005777

Barman, A., Rajak, F., & Jha, R. (2024). Integrating Wetlands as Nature-Based Solutions for Sustainable Built Environments: A Comprehensive Review. *Engineering, Technology & Applied Science Research*, *14*(6), 18670-18680.

Bates, D., Maechler, M., Bolker, B., & Walker, S. (2023). *lme4: Linear mixed-effects models using Eigen and S4* (R package version). https://CRAN.R-project.org/package=lme4

Bellinger, E. G., & Sigee, D. C. (2015). *Freshwater algae: identification, enumeration and use as bioindicators*. John Wiley & Sons.

Berhongaray, G., Cotrufo, F. M., Janssens, I. A., & Ceulemans, R. (2019). Below-ground carbon inputs contribute more than above-ground inputs to soil carbon accrual in a bioenergy poplar plantation. *Plant and soil*, *434*, 363-378.

Bolker, B., & Robinson, D. (2023). *broom.mixed: Tidying methods for mixed models* (R package version). https://CRAN.R-project.org/package=broom.mixed

Bonneville, M. C. (2006). Measurement and modeling of surface-atmosphere exchange of carbon dioxide and methane in a cattail marsh in Eastern Ontario. M.Sc. thesis, McGill University.

Boon, P. I., & Mitchell, A. (1995). Methanogenesis in the sediments of an Australian freshwater wetland: Comparison with aerobic decay, and factors controlling methanogenesis. *FEMS Microbiology Ecology*, *18*(3), 175-190.

Booth, R. K., & Sullivan, M. E. (2007). Testate amoebae as paleohydrological proxies in peatlands. In *A workshop focused on testate amoeba identification, ecology, and their use in paleoenvironmental reconstruction*. Université du Québec à Montréal & McGill University.

Borcard, D., Legendre, P., & Drapeau, P. (1992). Partialling out the spatial component of ecological variation. *Ecology, 73*, 1045–1055.

Bridgham, S. D., Megonigal, J. P., Keller, J. K., Bliss, N. B., & Trettin, C. (2006). The carbon balance of North American wetlands. *Wetlands*, *26*(4), 889–916.

Bridgham, S. D., Cadillo-Quiroz, H., Keller, J. K., & Zhuang, Q. (2013). Methane emissions from wetlands: Biogeochemical, microbial, and modeling perspectives from local to global scales. *Global Change Biology, 19*, 1325–1346.

Bredariol, J. V., de Matos, M. H. D. O., Souza-Silva, A. C., Meira, B. R., Lansac-Tôha, F. A., & Velho, L. F. M. (2026). Rethinking aquatic bioindicators: testate amoebae versus metazoans in plankton samples for assessing anthropogenic impacts on freshwater ecosystems. *Environmental Monitoring and Assessment*, *198*(3), 261.

Bruland, G. L., & Richardson, C. J. (2006). Comparison of soil organic matter in created, restored and paired natural wetlands in North Carolina. *Wetlands Ecology and Management*, *14*(3), 245-251.

Bubier, J. L., Moore, T. R., & Roulet, N. T. (1993). Methane emissions from wetlands in the midboreal region of northern Ontario, Canada. *Ecology*, *74*(8), 2240-2254.

Butterbach-Bahl, K., Baggs, E. M., Dannenmann, M., Kiese, R., & Zechmeister-Boltenstern, S. (2013). Nitrous oxide emissions from soils: How well do we understand the processes and their controls? *Philosophical Transactions of the Royal Society B: Biological Sciences, 368*, 20130122.

Chanton, J. P., Whiting, G. J., Happell, J. D., & Gerard, G. (1993). Contrasting rates and diurnal patterns of methane emission from emergent aquatic macrophytes. *Aquatic botany*, *46*(2), 111-128.

Chmura, G. L., Kellman, L., Van Ardenne, L., & Guntenspergen, G. R. (2016). Greenhouse gas fluxes from salt marshes exposed to chronic nutrient enrichment. *PLoS ONE*, *11*(2), e0149937.

Cook, R. D. (1977). Detection of influential observation in linear regression. *Technometrics, 19*, 15–18.

Creed, I. F., Miller, J., Aldred, D., Adams, J. K., Spitale, S., & Bourbonniere, R. A. (2013). Hydrologic profiling for greenhouse gas effluxes from natural grasslands in the prairie pothole region of Canada. *Journal of Geophysical Research: Biogeosciences*, *118*(2), 680–697.

Creed, I. F., Badiou, P., Enanga, E., Lobb, D. A., Pattison-Williams, J. K., Lloyd-Smith, P., & Gloutney, M. (2022). Can restoration of freshwater mineral soil wetlands deliver nature-based climate solutions to agricultural landscapes? *Frontiers in Ecology and Evolution*, *10*, 932415.

Davidson, E. A., & Janssens, I. A. (2006). Temperature sensitivity of soil carbon decomposition and feedbacks to climate change. *Nature*, *440*(7081), 165–173. https://doi.org/10.1038/nature04514

Davies, M. A., McLaughlin, J. W., Packalen, M. S., & Finkelstein, S. A. (2021). Using water table depths inferred from testate amoebae to estimate Holocene methane emissions from

the Hudson Bay Lowlands, Canada. *Journal of Geophysical Research: Biogeosciences, 126*(2), e2020JG005969.

Dolédec, S., & Chessel, D. (1994). Co-inertia analysis: An alternative method for studying species–environment relationships. *Freshwater Biology, 31*, 277–294.

Dray, S., Dufour, A.-B., & Chessel, D. (2007). The ade4 package – II: Two-table and K-table methods. *R News, 7*, 47–52.

Drever, C. R., Cook-Patton, S. C., Akhter, F., Badiou, P. H., Chmura, G. L., Davidson, S. J., … & Kurz, W. A. (2021). Natural climate solutions for Canada. *Science Advances*, *7*(23), eabd6034.

Dušek, J., Faußer, A., Stellner, S., & Kazda, M. (2023). Stems of *Phragmites australis* are buffering methane and carbon dioxide emissions. *Science of The Total Environment*, *882*, 163493.

Environment and Climate Change Canada. (n.d.). *Canadian climate normals 1991–2020: Toronto Pearson International Airport, Ontario*. Government of Canada. https://climate.weather.gc.ca/climate_normals/results_1991_2020_e.html

Filonchyk, M., Peterson, M. P., Zhang, L., Hurynovich, V., & He, Y. (2024). Greenhouse gases emissions and global climate change: Examining the influence of CO2, CH4, and N2O. *Science of The Total Environment*, 173359.

Firke, S. (2023). *janitor: Simple tools for examining and cleaning dirty data* (R package version). https://CRAN.R-project.org/package=janitor

Forfora, N., Azuaje, I., Vivas, K. A., Vera, R. E., Brito, A., Venditti, R., ... & Gonzalez, R. (2024). Evaluating biomass sustainability: Why below-ground carbon sequestration matters. *Journal of Cleaner Production*, *439*, 140677.

Frau, D., & Pineda, A. (2024). Phytoplankton species and traits response to a gradient of urbanization in subtropical lowland streams. *Ecohydrology*, *17*(6), e2675.

Frésard, A., Mulot, M., Bertrand, G., Lhosmot, A., Gandois, L., Tuittila, E. S., & Mitchell, E. A. D. (2023). Inferring northern peatland methane emissions from testate amoebae: A proof-of-concept study. *Mires and Peat, 29*, 20. https://doi.org/10.19189/MaP.2022.OMB.Sc.2089688

Geisen, S., Mitchell, E. A. D., Adl, S., Bonkowski, M., et al. (2018). Soil protists: A fertile frontier in soil biology research. *FEMS Microbiology Reviews, 42*, 293–323.

Haak, A. (2026). *Hydrologic regime controls greenhouse gas emissions in constructed mineral-soil wetlands dominated by emergent vegetation* (Unpublished manuscript, Chapter 2 of MSc thesis). Lakehead University.

Hassett, E., Bohrer, G., Kinsman-Costello, L., Onyango, Y., Pope, T., Smith, C., ... & Morin, T. (2024). Changes in inundation drive carbon dioxide and methane fluxes in a temperate wetland. *Science of the Total Environment*, *915*, 170089.

Ingrao, C., Failla, S., & Arcidiacono, C. (2020). A comprehensive review of environmental and operational issues of constructed wetland systems. *Current Opinion in Environmental Science & Health*, *13*, 35-45.

IPCC. (2021). *Climate Change 2021: The Physical Science Basis. Contribution of Working Group I to the Sixth Assessment Report of the Intergovernmental Panel on Climate Change* [Masson-Delmotte, V., P. Zhai, A. Pirani, S. L. Connors, C. Péan, S. Berger, N. Caud, Y. Chen, L. Goldfarb, M. I. Gomis, M. Huang, K. Leitzell, E. Lonnoy, J. B. R. Matthews, T. K. Maycock, T. Waterfield, O. Yelekçi, R. Yu, and B. Zhou (eds.)]. Cambridge University Press, Cambridge, United Kingdom and New York, NY, USA. doi:10.1017/9781009157896.

Jassey, V. E. J., Chiapusio, G., Binet, P., et al. (2013). Above- and belowground linkages in Sphagnum peatlands: Climate warming affects plant–microbial interactions. *Global Change Biology, 19*, 811–823.

Jassey, V. E. J., Signarbieux, C., Hättenschwiler, S., et al. (2015). An unexpected role of mixotrophs in the response of peatland carbon cycling to climate warming. *Scientific Reports, 5*, 16931.

Jensen, S., Whitfield, C. J., Bortolotti, L. E., Leavitt, P. R., Simpson, G. L., Badiou, P., & Finlay, K. (2023). Differential controls of greenhouse gas (CO_2, CH_4, and N_2O) concentrations in natural wetland ponds and agricultural reservoirs in the northern Great Plains. *Journal of Geophysical Research: Biogeosciences, 128*(4). https://doi.org/10.1029/2022JG007261

Kadlec, R. H., & Wallace, S. D. (2009). *Treatment wetlands* (2nd ed.). CRC Press.

Keller, J. K. (2011). Wetlands and the global carbon cycle: what might the simulated past tell us about the future?. *The New Phytologist*, *192*(4), 789-792.

Kim, J., Verma, S. B., & Billesbach, D. P. (1999). Seasonal variation in methane emission from a temperate *Phragmites*-dominated marsh: Effect of growth stage and plant-mediated transport. *Global Change Biology, 5*(4), 433–440. https://doi.org/10.1046/j.1365-2486.1999.00237.x

Knox, S. H., Sturtevant, C., Matthes, J. H., Koteen, L., Verfaillie, J., & Baldocchi, D. (2015). Agricultural peatland restoration: effects of land-use change on greenhouse gas (CO_2 and CH_4) fluxes in the Sacramento–San Joaquin Delta. *Global Change Biology*, *21*(2), 750–765. https://doi.org/10.1111/gcb.12745

Kuznetsova, A., Brockhoff, P. B., & Christensen, R. H. B. (2023). *lmerTest: Tests in linear mixed effects models* (R package version). https://CRAN.R-project.org/package=lmerTest

Legendre, P., & Gallagher, E. D. (2001). Ecologically meaningful transformations for ordination of species data. *Oecologia, 129*, 271–280.

Legendre, P., & Legendre, L. (2012). *Numerical ecology* (3rd English ed.). Elsevier.

Le Mer, J., & Roger, P. (2001). Production, oxidation, emission and consumption of methane by soils: a review. *European Journal of Soil Biology*, *37*(1), 25–50.

Lüdecke, D., Ben-Shachar, M. S., Patil, I., Waggoner, P., & Makowski, D. (2023). *performance: Assessment of regression models performance* (R package version). https://CRAN.R-project.org/package=performance

Ma, S., Creed, I. F., & Badiou, P. (2024). New perspectives on temperate inland wetlands as natural climate solutions under different CO_2-equivalent metrics. *npj Climate and Atmospheric Science*, *7*(1), 222.

Magenheimer, J. F., Moore, T. R., Chmura, G. L., & Daoust, R. J. (1996). Methane and carbon dioxide flux from a macrotidal salt marsh, Bay of Fundy, New Brunswick. *Estuaries*, *19*(1), 139–145. https://doi.org/10.2307/1352658

Mander, Ü., Maddison, M., Soosaar, K., & Karabelnik, K. (2011). The impact of pulsing hydrology and fluctuating water table on greenhouse gas emissions from constructed wetlands. *Wetlands*, *31*, 1023–1032.

Mander, Ü., Dotro, G., Ebie, Y., Towprayoon, S., Chiemchaisri, C., Nogueira, S. F., … & Mitsch, W. J. (2014). Greenhouse gas emission in constructed wetlands for wastewater treatment: a review. *Ecological Engineering*, *66*, 19–35.

Maucieri, C., Barbera, A. C., Vymazal, J. & Borin, M. (2017). *A review on the main factors affecting greenhouse gas emissions in constructed wetlands*. *Agricultural and Forest Meteorology, 236*, 175–193. https://doi.org/10.1016/j.agrformet.2017.01.006

Mitchell, E. A. D., Charman, D. J., & Warner, B. G. (2008). Testate amoebae analysis in ecological and paleoecological studies of wetlands: Past, present and future. *Biodiversity and Conservation, 17*, 2115–2137.

Mitsch, W. J., Bernal, B., Nahlik, A. M., Mander, Ü., Zhang, L., Anderson, C. J., … & Brix, H. (2013). Wetlands, carbon, and climate change. *Landscape Ecology*, *28*(4), 583–597.

Müller, K., & Wickham, H. (2023). *tibble: Simple data frames* (R package version). https://CRAN.R-project.org/package=tibble

Muñoz, I., Schmidt, J., & Weidema, B. P. (2024). The indirect global warming potential of methane oxidation in the IPCC's sixth assessment report. *Environmental Research Letters*, *19*(12), 121002.

Nahlik, A. M., & Mitsch, W. J. (2010). Methane emissions from created riverine wetlands. *Wetlands*, *30*(4), 783–793. https://doi.org/10.1007/s13157-010-0038-6

Neubauer, S. C., & Megonigal, J. P. (2015). Moving beyond global warming potentials to quantify the climatic role of ecosystems. *Ecosystems*, *18*, 1000–1013. https://doi.org/10.1007/s10021-015-9879-4

Ogden, G. G., & Hedley, R. H. (1980). An atlas of freshwater testate amoebae. *Soil Science*, *130*(3), 176.

OpenAI. (2024). *ChatGPT* (v.5.2) [Large language model]. https://chatgpt.com

Oksanen, L. (2001). Logic of experiments in ecology: Is pseudoreplication a pseudoissue? *Oikos, 94*, 27–38.

Oksanen, J., Simpson, G. L., Blanchet, F. G., et al. (2022). *vegan: Community ecology package* (R package version 2.6-4).

Paul, E., & Frey, S. (Eds.). (2023). *Soil microbiology, ecology and biochemistry*. Elsevier.

Pennock, D., Yates, T., Bedard-Haughn, A., Phipps, K., Farrell, R., & McDougal, R. (2010). Landscape controls on N_2O and CH_4 emissions from freshwater mineral soil wetlands of the Canadian Prairie Pothole region. *Geoderma*, *155*(3–4), 308–319.

Peres-Neto, P. R., Legendre, P., Dray, S., & Borcard, D. (2006). Variation partitioning of species data matrices: Estimation and comparison of fractions. *Ecology, 87*, 2614–2625.

Posit Team. (2025). *RStudio: Integrated development environment for R* [Computer software]. Posit Software, PBC. https://posit.co/

Poulter, B., Fluet-Chouinard, E., Hugelius, G., Koven, C., Fatoyinbo, L., Page, S. E., ... & Wijedasa, L. S. (2021). A review of global wetland carbon stocks and management challenges. *Wetland carbon and environmental management*, 1-20.

R Core Team. (2023). *grid: The grid graphics package* (R package version). https://CRAN.R-project.org

R Core Team. (2026). *R: A language and environment for statistical computing* (Version 4.5.2) [Computer software]. R Foundation for Statistical Computing. https://www.r-project.org/

Reay, D. S., Smith, P., Christensen, T. R., James, R. H., & Clark, H. (2018). Methane and global environmental change. *Annual Review of Environment and Resources*, *43*(1), 165–192.

Reddy, K. R., DeLaune, R. D., & Inglett, P. W. (2022). *Biogeochemistry of Wetlands: Science and Applications*. CRC Press.

Robert, P., & Escoufier, Y. (1976). A unifying tool for linear multivariate statistical methods: The RV-coefficient. *Journal of the Royal Statistical Society: Series C (Applied Statistics), 25*, 257–265.

Schauberger, P., & Walker, A. (2023). *openxlsx: Read, write and edit xlsx files* (R package version). https://CRAN.R-project.org/package=openxlsx

Schuster, L., Taillardat, P., Macreadie, P. I., & Malerba, M. E. (2024). Freshwater wetland restoration and conservation are long-term natural climate solutions. *Science of The Total Environment*, *922*, 171218.

Sebacher, D. I., Harriss, R. C., & Bartlett, K. B. (1985). Methane emissions to the atmosphere through aquatic plants (Vol. 14, No. 1, pp. 40-46). American Society of Agronomy, Crop Science Society of America, and Soil Science Society of America.

Segers, R. (1998). Methane production and methane consumption: a review of processes underlying wetland methane fluxes. *Biogeochemistry*, *41*, 23–51. https://doi.org/10.1023/A:1005929032764

Siemensma, F. J. (n.d.). *Microworld: World of amoeboid organisms*. https://arcella.nl/

Silva, Y. G. D., Sampaio, G. S., Ramos, B. R. D. O., Freitas, Y. D. G. C., Nascimento, L., Branco, C. W. C., & Miranda, V. B. D. S. (2022). Testate amoebae (Amorphea, Amoebozoa, Cercozoa) as bioindicators: a scientometric review. *Acta Limnologica Brasiliensia*, *34*, e20.

Simpson, G. L. (2023). *permute: Functions for generating restricted permutations of data* (R package version). https://CRAN.R-project.org/package=permute

Søvik, A. K., Augustin, J., Heikkinen, K., Huttunen, J. T., Necki, J. M., Karjalainen, S. M., Kløve, B., Liikanen, A., Mander, Ü., Puustinen, M., Teiter, S., & Wachniew, P. (2006). *Emission of the greenhouse gases nitrous oxide and methane from constructed wetlands in Europe*. *Journal of Environmental Quality, 35*(6), 2360–2373. https://doi.org/10.2134/jeq2006.0038

Stevenson, R. J., Bothwell, M. L., & Lowe, R. L. (Eds.). (1996). *Algal ecology: Freshwater benthic ecosystems*. Academic Press.

Sundquist, E. T., Ackerman, K. V., Parker, L., Huntzinger, D. N., & McPherson, B. J. (2009). An Introduction to Global Carbon Cycle Management. In Carbon Sequestration and Its Role in the Global Carbon Cycle (Vol. 183, pp. 1–23). *American Geophysical Union.* https://doi.org/10.1029/2009GM000914

Tangen, B. A., & Bansal, S. (2020). Soil organic carbon stocks and sequestration rates of inland, freshwater wetlands: Sources of variability and uncertainty. *Science of the Total Environment*, *749*, 141444.

Trettin, C. C., Kolka, R. K., Marsh, A. S., Bansal, S., Lilleskov, E. A., Megonigal, P., … & Gries, J. (2020). Wetland and hydric soils. In *Forest and Rangeland Soils of the United States under Changing Conditions: A Comprehensive Science Synthesis* (pp. 99–126).

Turetsky, M. R., Kotowska, A., Bubier, J., Dise, N. B., Crill, P., Hornibrook, E. R., … & Wilmking, M. (2014). A synthesis of methane emissions from 71 northern, temperate, and subtropical wetlands. *Global Change Biology*, *20*(7), 2183–2197. https://doi.org/10.1111/gcb.12580

US Department of Energy. (1985). the Global Carbon Cycle. *Atmospheric carbon dioxide and the global carbon cycle* (DOE/ER-0239). Washington, DC.

Van Amstel, A. (2012). Methane: A review. *Journal of Integrative Environmental Sciences*, *9*(sup1), 5–30. https://doi.org/10.1080/1943815X.2012.694892

Van Cleemput, O., Boeckx, P., Lindgren, P. E., & Tonderski, K. (2007). Denitrification in wetlands. In *Biology of the nitrogen cycle* (pp. 359-367). Elsevier.Van Dam, H., Mertens, A., & Sinkeldam, J. (1994). A coded checklist and ecological indicator values of freshwater diatoms from The Netherlands. *Netherlands Journal of Aquatic Ecology, 28*, 117–133.

Venables, W. N., & Ripley, B. D. (2002). *MASS: Support functions and datasets for Venables and Ripley's MASS* (R package version). https://CRAN.R-project.org/package=MASS

Villa, J. A., & Bernal, B. (2018). Carbon sequestration in wetlands, from science to practice: An overview of the biogeochemical process, measurement methods, and policy framework. *Ecological Engineering*, *114*, 115–128.

Vymazal, J. (2007). Removal of nutrients in various types of constructed wetlands. *Science of the Total Environment, 380*, 48–65.

Wallace, J., Champagne, P., Hall, G., Yin, Z., & Liu, X. (2015). Determination of algae and macrophyte species distribution in three wastewater stabilization ponds using metagenomics analysis. *Water*, *7*(7), 3225-3242.

Wanner, M., Birkhofer, K., Fischer, T., Shimizu, M., Shimano, S., & Puppe, D. (2020). Soil testate amoebae and diatoms as bioindicators of an old heavy metal contaminated floodplain in Japan. *Microbial ecology*, *79(1),* 123-133.

Wehr, J. D., Sheath, R. G., & Kociolek, J. P. (Eds.). (2015). Freshwater algae of North America: Ecology and classification (2nd ed.). *Elsevier*.

Whalen, S. C. (2005). Biogeochemistry of methane exchange between natural wetlands and the atmosphere. *Environmental Engineering Science, 22*, 73–94.

Wickham, H. (2016). *ggplot2: Elegant graphics for data analysis* (R package version). https://CRAN.R-project.org/package=ggplot2

Wickham, H. (2023). *stringr: Simple, consistent wrappers for common string operations* (R package version). https://CRAN.R-project.org/package=stringr

Wickham, H. (2023). *forcats: Tools for working with categorical variables (factors)* (R package version). https://CRAN.R-project.org/package=forcats

Wickham, H., Bryan, J., & RStudio Team. (2023). *readxl: Read Excel files* (R package version). https://CRAN.R-project.org/package=readxl

Wickham, H., François, R., Henry, L., & Müller, K. (2023). *dplyr: A grammar of data manipulation* (R package version). https://CRAN.R-project.org/package=dplyr

Wickham, H., & Girlich, M. (2023). *tidyr: Tidy messy data* (R package version). https://CRAN.R-project.org/package=tidyr

Wickham, H., Hester, J., & Bryan, J. (2023). *readr: Read rectangular text data* (R package version). https://CRAN.R-project.org/package=readr

Wik, M., Varner, R. K., Anthony, K. W., MacIntyre, S., & Bastviken, D. (2016). Climate-sensitive northern lakes and ponds are critical components of methane release. *Nature Geoscience*, *9*(2), 99–105.

Wilkinson, D. M., & Mitchell, E. A. D. (2010). Testate amoebae and nutrient cycling with particular reference to soils. *Geomicrobiology Journal, 27*, 520–527.

Yavitt, J. B., & Knapp, A. K. (1995). Methane emission to the atmosphere through emergent cattail (Typha latifolia L.) plants. *Tellus B: Chemical and Physical Meteorology, 47*(5), 521–534.

Zhi, W., & Ji, G. (2012). Constructed wetlands, 1991–2011: A review of research development, current trends, and future directions. *Science of the Total Environment*, *441*, 19-27.

Appendices

Appendix 1 Soil Temperature and Water Depth Table

Site	Year	Month	Chamber ID	Soil Temperature (Celsius)	Water Table Depth (cm)
Circle Park	2023	July	CPGHG1	23	10
Circle Park	2023	July	CPGHG2	22	28
Circle Park	2023	July	CPGHG3	21.2	38.2
Circle Park	2023	July	CPGHG4	22.4	55
Circle Park	2023	July	CPGHG5	21.9	0
Circle Park	2023	July	CPGHG6	20.9	-20
Circle Park	2023	July	CPGHG7	20.3	50
Circle Park	2023	July	CPGHG8	20.3	80
Circle Park	2023	July	CPGHG9	20.3	77
Cawthra Mulock	2023	July	CMGHG1	21	32.5
Cawthra Mulock	2023	July	CMGHG2	20.5	36.8
Cawthra Mulock	2023	July	CMGHG3	20.7	30.4
Cawthra Mulock	2023	July	CMGHG4	20.6	36
Cawthra Mulock	2023	July	CMGHG5	20.7	15.5
Cawthra Mulock	2023	July	CMGHG6	19.8	17.5
Cawthra Mulock	2023	July	CMGHG7	19.9	12
Cawthra Mulock	2023	July	CMGHG8	18.5	6.5
Cawthra Mulock	2023	July	CMGHG9	18.5	12.8

Cawthra Mulock	2023	July	CMGHG10	18.7	9
Cawthra Mulock	2023	July	CMGHG11	18.4	16.5
Beaver River	2023	July	BRWGHG1	16.5	3.2
Beaver River	2023	July	BRWGHG2	15.9	18
Beaver River	2023	July	BRWGHG3	16.1	1
Beaver River	2023	July	BRWGHG4	16.4	4.2
Circle Park	2023	October	CPGHG1	12.2	10
Circle Park	2023	October	CPGHG2	12.9	16
Circle Park	2023	October	CPGHG3	13.2	28.5
Circle Park	2023	October	CPGHG4	13	47
Circle Park	2023	October	CPGHG5	11.9	0
Circle Park	2023	October	CPGHG6	12	3.8
Circle Park	2023	October	CPGHG7	11.2	42.5
Circle Park	2023	October	CPGHG8	11.2	68
Circle Park	2023	October	CPGHG9	11.2	73.3
Cawthra Mulock	2023	October	CMGHG1	11.8	-20
Cawthra Mulock	2023	October	CMGHG2	12.8	-20
Cawthra Mulock	2023	October	CMGHG3	11.7	-20
Cawthra Mulock	2023	October	CMGHG4	12	-20
Cawthra Mulock	2023	October	CMGHG5	12.3	-20
Cawthra Mulock	2023	October	CMGHG6	12.1	-20
Cawthra Mulock	2023	October	CMGHG7	11.9	-20
Cawthra Mulock	2023	October	CMGHG8	11.9	-20
Cawthra Mulock	2023	October	CMGHG9	12.4	-20
Cawthra Mulock	2023	October	CMGHG10	11.4	-20
Cawthra Mulock	2023	October	CMGHG11	11.6	-20
Beaver River	2023	October	BRWGHG1	8.1	-3
Beaver River	2023	October	BRWGHG2	10.1	9
Beaver River	2023	October	BRWGHG3	10.1	-9.9
Beaver River	2023	October	BRWGHG4	9.9	-8
Circle Park	2024	February	CPGHG1	n/a	0

Circle Park	2024	February	CPGHG2	n/a	0
Circle Park	2024	February	CPGHG3	n/a	0
Circle Park	2024	February	CPGHG4	n/a	0
Circle Park	2024	February	CPGHG5	n/a	0
Circle Park	2024	February	CPGHG6	n/a	0
Circle Park	2024	February	CPGHG7	n/a	0
Circle Park	2024	February	CPGHG8	n/a	0
Circle Park	2024	February	CPGHG9	n/a	0
Cawthra Mulock	2024	February	CMGHG1	n/a	0
Cawthra Mulock	2024	February	CMGHG2	n/a	0
Cawthra Mulock	2024	February	CMGHG3	n/a	0
Cawthra Mulock	2024	February	CMGHG4	n/a	0
Cawthra Mulock	2024	February	CMGHG5	n/a	0
Cawthra Mulock	2024	February	CMGHG6	n/a	0
Cawthra Mulock	2024	February	CMGHG7	n/a	0
Cawthra Mulock	2024	February	CMGHG8	n/a	0
Cawthra Mulock	2024	February	CMGHG9	n/a	0
Cawthra Mulock	2024	February	CMGHG10	n/a	0
Cawthra Mulock	2024	February	CMGHG11	n/a	0
Beaver River	2024	February	BRWGHG1	n/a	0
Beaver River	2024	February	BRWGHG2	n/a	0
Beaver River	2024	February	BRWGHG3	n/a	0
Beaver River	2024	February	BRWGHG4	n/a	0
Circle Park	2024	April	CPGHG1	9	24
Circle Park	2024	April	CPGHG2	9.6	27
Circle Park	2024	April	CPGHG3	11.5	38
Circle Park	2024	April	CPGHG4	11.5	53
Circle Park	2024	April	CPGHG5	10.2	13.9
Circle Park	2024	April	CPGHG6	10.5	5
Circle Park	2024	April	CPGHG7	9	45
Circle Park	2024	April	CPGHG8	12.5	78
Circle Park	2024	April	CPGHG9	11.1	80

Cawthra Mulock	2024	April	CMGHG1	10	48
Cawthra Mulock	2024	April	CMGHG2	10	40
Cawthra Mulock	2024	April	CMGHG3	10	50
Cawthra Mulock	2024	April	CMGHG4	10	47
Cawthra Mulock	2024	April	CMGHG5	10.2	32
Cawthra Mulock	2024	April	CMGHG6	10	32
Cawthra Mulock	2024	April	CMGHG7	9.6	30
Cawthra Mulock	2024	April	CMGHG8	9.1	20
Cawthra Mulock	2024	April	CMGHG9	9.1	28
Cawthra Mulock	2024	April	CMGHG10	9.2	30
Cawthra Mulock	2024	April	CMGHG11	9.3	29
Beaver River	2024	April	BRWGHG1	4	-7
Beaver River	2024	April	BRWGHG2	5.2	9.8
Beaver River	2024	April	BRWGHG3	3.9	-13
Beaver River	2024	April	BRWGHG4	5.7	-7
Circle Park	2024	July	CPGHG1	23	7.9
Circle Park	2024	July	CPGHG2	22	25.4
Circle Park	2024	July	CPGHG3	22.5	38.1
Circle Park	2024	July	CPGHG4	22	58.4
Circle Park	2024	July	CPGHG5	23	6.4
Circle Park	2024	July	CPGHG6	23.5	0
Circle Park	2024	July	CPGHG7	20	45.2
Circle Park	2024	July	CPGHG8	19.5	68.6
Circle Park	2024	July	CPGHG9	19.5	80
Cawthra Mulock	2024	July	CMGHG1	20	18
Cawthra Mulock	2024	July	CMGHG2	20	22
Cawthra Mulock	2024	July	CMGHG3	20	14
Cawthra Mulock	2024	July	CMGHG4	20	16

Cawthra Mulock	2024	July	CMGHG5	20	-16.5
Cawthra Mulock	2024	July	CMGHG6	20	-15.2
Cawthra Mulock	2024	July	CMGHG7	21.3	-15.2
Cawthra Mulock	2024	July	CMGHG8	20.1	-19.1
Cawthra Mulock	2024	July	CMGHG9	21	-31.6
Cawthra Mulock	2024	July	CMGHG10	20.5	-18.4
Cawthra Mulock	2024	July	CMGHG11	21.4	-16.8
Beaver River	2024	July	BRWGHG1	15.3	2.3
Beaver River	2024	July	BRWGHG2	15.3	13.2
Beaver River	2024	July	BRWGHG3	15.5	2.5
Beaver River	2024	July	BRWGHG4	16.7	6.9
Circle Park	2024	October	CPGHG1	7.8	-12.7
Circle Park	2024	October	CPGHG2	10	13.97
Circle Park	2024	October	CPGHG3	11	30.48
Circle Park	2024	October	CPGHG4	11	38.1
Circle Park	2024	October	CPGHG5	7.5	1.9
Circle Park	2024	October	CPGHG6	7.6	0
Circle Park	2024	October	CPGHG7	10	50.8
Circle Park	2024	October	CPGHG8	9.5	66.04
Circle Park	2024	October	CPGHG9	9.5	69.2
Cawthra Mulock	2024	October	CMGHG1	8.5	-38.1
Cawthra Mulock	2024	October	CMGHG2	9.2	-38.1
Cawthra Mulock	2024	October	CMGHG3	8.6	-38.1
Cawthra Mulock	2024	October	CMGHG4	9.2	-38.1
Cawthra Mulock	2024	October	CMGHG5	10.2	-38.1
Cawthra Mulock	2024	October	CMGHG6	10	-38.1
Cawthra Mulock	2024	October	CMGHG7	9.4	-38.1
Cawthra Mulock	2024	October	CMGHG8	9.3	-38.1

Cawthra Mulock	2024	October	CMGHG9	9.6	-38.1
Cawthra Mulock	2024	October	CMGHG10	9	-38.1
Cawthra Mulock	2024	October	CMGHG11	8.7	-38.1
Beaver River	2024	October	BRWGHG1	7.4	-6.35
Beaver River	2024	October	BRWGHG2	7.7	1
Beaver River	2024	October	BRWGHG3	8.4	-12.7
Beaver River	2024	October	BRWGHG4	8	-8.89
Circle Park	2025	February	CPGHG1	n/a	46
Circle Park	2025	February	CPGHG2	n/a	40
Circle Park	2025	February	CPGHG3	n/a	60
Circle Park	2025	February	CPGHG4	n/a	50
Circle Park	2025	February	CPGHG5	n/a	40
Circle Park	2025	February	CPGHG6	n/a	39
Circle Park	2025	February	CPGHG7	n/a	56
Circle Park	2025	February	CPGHG8	n/a	42
Circle Park	2025	February	CPGHG9	n/a	60
Cawthra Mulock	2025	February	CMGHG1	n/a	48
Cawthra Mulock	2025	February	CMGHG2	n/a	42.5
Cawthra Mulock	2025	February	CMGHG3	n/a	41
Cawthra Mulock	2025	February	CMGHG4	n/a	47
Cawthra Mulock	2025	February	CMGHG5	n/a	51
Cawthra Mulock	2025	February	CMGHG6	n/a	35
Cawthra Mulock	2025	February	CMGHG7	n/a	46
Cawthra Mulock	2025	February	CMGHG8	n/a	41
Cawthra Mulock	2025	February	CMGHG9	n/a	41
Cawthra Mulock	2025	February	CMGHG10	n/a	45
Cawthra Mulock	2025	February	CMGHG11	n/a	47
Beaver River	2025	February	BRWGHG1	n/a	17
Beaver River	2025	February	BRWGHG2	n/a	29
Beaver River	2025	February	BRWGHG3	n/a	27

Beaver River	2025	February	BRWGHG4	n/a	33
Circle Park	2025	April	CPGHG1	8.6	11.4
Circle Park	2025	April	CPGHG2	9.4	24.8
Circle Park	2025	April	CPGHG3	10.1	43.2
Circle Park	2025	April	CPGHG4	11.6	63.5
Circle Park	2025	April	CPGHG5	10.2	13.9
Circle Park	2025	April	CPGHG6	10.5	5
Circle Park	2025	April	CPGHG7	9	45.7
Circle Park	2025	April	CPGHG8	12.5	78.7
Circle Park	2025	April	CPGHG9	12.1	78.7
Cawthra Mulock	2025	April	CMGHG1	9.2	50.6
Cawthra Mulock	2025	April	CMGHG2	9	48.3
Cawthra Mulock	2025	April	CMGHG3	9	48.3
Cawthra Mulock	2025	April	CMGHG4	9	48.3
Cawthra Mulock	2025	April	CMGHG5	9.5	27.7
Cawthra Mulock	2025	April	CMGHG6	9.3	30.48
Cawthra Mulock	2025	April	CMGHG7	9.5	25.4
Cawthra Mulock	2025	April	CMGHG8	9.3	19
Cawthra Mulock	2025	April	CMGHG9	9.5	25.4
Cawthra Mulock	2025	April	CMGHG10	9.5	26.7
Cawthra Mulock	2025	April	CMGHG11	9.5	28.2
Beaver River	2025	April	BRWGHG1	4.6	5
Beaver River	2025	April	BRWGHG2	2.9	-10.16
Beaver River	2025	April	BRWGHG3	0.9	-9.1
Beaver River	2025	April	BRWGHG4	3.8	-10.16
Circle Park	2025	May	CPGHG1	14.9	12.5
Circle Park	2025	May	CPGHG2	15.7	29.5
Circle Park	2025	May	CPGHG3	15.9	43
Circle Park	2025	May	CPGHG4	15.2	58
Circle Park	2025	May	CPGHG5	15.9	15.4
Circle Park	2025	May	CPGHG6	17.6	2
Circle Park	2025	May	CPGHG7	15	57

Circle Park	2025	May	CPGHG8	14.7	71.5
Circle Park	2025	May	CPGHG9	14.9	86.5
Cawthra Mulock	2025	May	CMGHG1	15.9	51
Cawthra Mulock	2025	May	CMGHG2	15.4	54
Cawthra Mulock	2025	May	CMGHG3	15.6	46
Cawthra Mulock	2025	May	CMGHG4	14.8	49
Cawthra Mulock	2025	May	CMGHG5	15.7	32
Cawthra Mulock	2025	May	CMGHG6	14.6	32
Cawthra Mulock	2025	May	CMGHG7	16.1	31
Cawthra Mulock	2025	May	CMGHG8	13.3	21.4
Cawthra Mulock	2025	May	CMGHG9	13.9	28
Cawthra Mulock	2025	May	CMGHG10	13.8	32
Cawthra Mulock	2025	May	CMGHG11	14.6	31.5
Beaver River	2025	May	BRWGHG1	12.9	-7
Beaver River	2025	May	BRWGHG2	12.1	9.8
Beaver River	2025	May	BRWGHG3	11.1	-13
Beaver River	2025	May	BRWGHG4	11.5	-7
Circle Park	2025	June	CPGHG1	23.1	8.5
Circle Park	2025	June	CPGHG2	25.5	18.5
Circle Park	2025	June	CPGHG3	24.4	31.5
Circle Park	2025	June	CPGHG4	24.4	52.2
Circle Park	2025	June	CPGHG5	24	17
Circle Park	2025	June	CPGHG6	24	0
Circle Park	2025	June	CPGHG7	22.9	52
Circle Park	2025	June	CPGHG8	18.1	80.5
Circle Park	2025	June	CPGHG9	18.1	93
Cawthra Mulock	2025	June	CMGHG1	22.4	28.5
Cawthra Mulock	2025	June	CMGHG2	21.6	34
Cawthra Mulock	2025	June	CMGHG3	22.3	25

Cawthra Mulock	2025	June	CMGHG4	22.8	31.5
Cawthra Mulock	2025	June	CMGHG5	20.9	15
Cawthra Mulock	2025	June	CMGHG6	21.2	14.5
Cawthra Mulock	2025	June	CMGHG7	22.2	7.5
Cawthra Mulock	2025	June	CMGHG8	22.6	1
Cawthra Mulock	2025	June	CMGHG9	19.1	13
Cawthra Mulock	2025	June	CMGHG10	20.2	13
Cawthra Mulock	2025	June	CMGHG11	20.1	13
Beaver River	2025	June	BRWGHG1	18.5	-15
Beaver River	2025	June	BRWGHG2	17.3	-3
Beaver River	2025	June	BRWGHG3	17.2	-15
Beaver River	2025	June	BRWGHG4	18.1	-12
Circle Park	2025	July	CPGHG1	20.9	-13.5
Circle Park	2025	July	CPGHG2	21.2	12
Circle Park	2025	July	CPGHG3	22.5	26
Circle Park	2025	July	CPGHG4	22.5	44
Circle Park	2025	July	CPGHG5	21.6	-5.5
Circle Park	2025	July	CPGHG6	21.7	-21
Circle Park	2025	July	CPGHG7	19.1	44
Circle Park	2025	July	CPGHG8	19.1	50
Circle Park	2025	July	CPGHG9	18.9	74
Cawthra Mulock	2025	July	CMGHG1	21.6	-20
Cawthra Mulock	2025	July	CMGHG2	21.6	-20
Cawthra Mulock	2025	July	CMGHG3	21.6	-20
Cawthra Mulock	2025	July	CMGHG4	21.6	-20
Cawthra Mulock	2025	July	CMGHG5	19.4	-20
Cawthra Mulock	2025	July	CMGHG6	19.4	-20
Cawthra Mulock	2025	July	CMGHG7	19.4	-20

Cawthra Mulock	2025	July	CMGHG8	21.4	-20
Cawthra Mulock	2025	July	CMGHG9	21.4	-20
Cawthra Mulock	2025	July	CMGHG10	20.9	-20
Cawthra Mulock	2025	July	CMGHG11	20.9	-20
Beaver River	2025	July	BRWGHG1	15.5	-31
Beaver River	2025	July	BRWGHG2	19.7	-15
Beaver River	2025	July	BRWGHG3	19.3	-29
Beaver River	2025	July	BRWGHG4	20.1	-25
Circle Park	2025	August	CPGHG1	15.3	-10
Circle Park	2025	August	CPGHG2	15.5	-1
Circle Park	2025	August	CPGHG3	17	19
Circle Park	2025	August	CPGHG4	17.4	29
Circle Park	2025	August	CPGHG5	16.6	-20
Circle Park	2025	August	CPGHG6	17.5	-20
Circle Park	2025	August	CPGHG7	16.3	26.2
Circle Park	2025	August	CPGHG8	16.2	54
Circle Park	2025	August	CPGHG9	16	47
Cawthra Mulock	2025	August	CMGHG1	19.9	-20
Cawthra Mulock	2025	August	CMGHG2	20.1	-20
Cawthra Mulock	2025	August	CMGHG3	20.1	-20
Cawthra Mulock	2025	August	CMGHG4	20	-20
Cawthra Mulock	2025	August	CMGHG5	19.9	-20
Cawthra Mulock	2025	August	CMGHG6	19.9	-20
Cawthra Mulock	2025	August	CMGHG7	19.9	-20
Cawthra Mulock	2025	August	CMGHG8	20.2	-20
Cawthra Mulock	2025	August	CMGHG9	20.2	-20
Cawthra Mulock	2025	August	CMGHG10	20.2	-20
Cawthra Mulock	2025	August	CMGHG11	20.2	-20
Beaver River	2025	August	BRWGHG1	16.3	-20

Beaver River	2025	August	BRWGHG2	16.5	-20
Beaver River	2025	August	BRWGHG3	16.8	-20
Beaver River	2025	August	BRWGHG4	16.7	-20
Circle Park	2025	September	CPGHG1	14.7	-20
Circle Park	2025	September	CPGHG2	14.8	-20
Circle Park	2025	September	CPGHG3	15.9	11
Circle Park	2025	September	CPGHG4	17.1	35
Circle Park	2025	September	CPGHG5	14.8	-20
Circle Park	2025	September	CPGHG6	14.9	-20
Circle Park	2025	September	CPGHG7	16.3	23
Circle Park	2025	September	CPGHG8	15.9	42
Circle Park	2025	September	CPGHG9	15.9	42
Cawthra Mulock	2025	September	CMGHG1	13.8	-20
Cawthra Mulock	2025	September	CMGHG2	14.3	-20
Cawthra Mulock	2025	September	CMGHG3	15.7	-20
Cawthra Mulock	2025	September	CMGHG4	14.2	-20
Cawthra Mulock	2025	September	CMGHG5	14.3	-20
Cawthra Mulock	2025	September	CMGHG6	14.3	-20
Cawthra Mulock	2025	September	CMGHG7	14.3	-20
Cawthra Mulock	2025	September	CMGHG8	14.9	-20
Cawthra Mulock	2025	September	CMGHG9	14.6	-20
Cawthra Mulock	2025	September	CMGHG10	14.7	-20
Cawthra Mulock	2025	September	CMGHG11	14.8	-20
Beaver River	2025	September	BRWGHG1	10.6	-12
Beaver River	2025	September	BRWGHG2	11.2	-0.5
Beaver River	2025	September	BRWGHG3	10.7	-16
Beaver River	2025	September	BRWGHG4	10.9	-17
Circle Park	2025	October	CPGHG1	10.9	-20
Circle Park	2025	October	CPGHG2	10.1	-20
Circle Park	2025	October	CPGHG3	10.8	9
Circle Park	2025	October	CPGHG4	12.3	30
Circle Park	2025	October	CPGHG5	12.4	-20

Circle Park	2025	October	CPGHG6	11.2	-20
Circle Park	2025	October	CPGHG7	11.2	21
Circle Park	2025	October	CPGHG8	11.8	44.5
Circle Park	2025	October	CPGHG9	11.8	53
Cawthra Mulock	2025	October	CMGHG1	9.5	-20
Cawthra Mulock	2025	October	CMGHG2	9.6	-20
Cawthra Mulock	2025	October	CMGHG3	9.6	-20
Cawthra Mulock	2025	October	CMGHG4	10.3	-20
Cawthra Mulock	2025	October	CMGHG5	11.7	-20
Cawthra Mulock	2025	October	CMGHG6	12.7	-20
Cawthra Mulock	2025	October	CMGHG7	12.1	-20
Cawthra Mulock	2025	October	CMGHG8	11.7	-20
Cawthra Mulock	2025	October	CMGHG9	11.8	-20
Cawthra Mulock	2025	October	CMGHG10	11.5	-20
Cawthra Mulock	2025	October	CMGHG11	10.6	-20
Beaver River	2025	October	BRWGHG1	9.6	-22
Beaver River	2025	October	BRWGHG2	9.1	9
Beaver River	2025	October	BRWGHG3	9.5	-8
Beaver River	2025	October	BRWGHG4	9.5	-3

Appendix 2 Greenhouse Gas Flux Summary Table

	Mean Flux ($mg\ m^{-2}\ h^{-1}$)	**StdDev of Flux ($mg\ m^{-2}\ h^{-1}$)**	**Min of Flux ($mg\ m^{-2}\ h^{-1}$)**	**Max of Flux ($mg\ m^{-2}\ h^{-1}$)**
2023				
July				
CO2				
Beaver River	833.157343	232.472558	628.3531096	1126.715895
Cawthra Mulock	507.9870624	241.2461227	176.2905865	907.6092251
Circle Park	1410.561383	902.7490499	514.8389321	3547.412439

CH4				
Beaver River	18.98725165	13.89553542	6.18087776	36.91884771
Cawthra Mulock	3.62189134	3.343429471	0.739394644	11.75270436
Circle Park	23.01392223	18.63450637	4.959685565	66.27412133
N2O				
Beaver River	-0.098182638	0.102886957	-0.25146481	-0.035932575
Cawthra Mulock	-0.024977705	0.063598336	-0.162148871	0.061694011
Circle Park	-0.027761789	0.064657918	-0.112341652	0.082189237
October				
CO2				
Beaver River	165.7028455	30.0290104	143.9870501	209.6608916
Cawthra Mulock	105.2411977	405.2216936	-1059.843698	498.6797698
Circle Park	316.7392136	180.3708281	126.4711849	709.121598
CH4				
Beaver River	2.17607343	1.112470876	1.094073691	3.684382579
Cawthra Mulock	-0.094622194	0.479133531	-1.372935349	0.481088636
Circle Park	55.79033063	149.2345696	-0.101040998	453.5435206
N2O				
Beaver River	-0.024498358	0.027113242	-0.0532626	0.002018875
Cawthra Mulock	-0.010417508	0.031753325	-0.095741202	0.029526957
Circle Park	-0.002070264	0.024014504	-0.046606517	0.040078104
2024				
February				
CO2				
Beaver River	-7.155294756	47.64668041	-54.5837534	45.68180447
Cawthra Mulock	24.60623361	67.20552251	-64.26391701	100.8590255
Circle Park	31.04802489	40.07999421	-23.91710883	101.8915356
CH4				
Beaver River	0.191274429	0.185998295	-0.064372317	0.342930148
Cawthra Mulock	0.081232447	0.109995399	-0.069848713	0.324134125
Circle Park	1.80549166	1.857335343	-0.048506388	5.172674592
N2O				
Beaver River	-0.008438563	0.011603009	-0.02078054	0.003640452
Cawthra Mulock	-0.002624672	0.019527031	-0.040349802	0.015183235
Circle Park	0.000988388	0.012992724	-0.019908678	0.015115627
April				
CO2				
Beaver River	389.4004933	24.61698148	361.6846027	412.3502781
Cawthra Mulock	166.5698731	102.2114988	10.94071349	290.6963114

Circle Park	203.6970541	254.8367476	11.81452032	861.9500466
CH4				
Beaver River	0.975783385	0.695643095	0.555244816	2.015301163
Cawthra Mulock	0.96297585	1.120344458	-0.18486093	3.526989285
Circle Park	29.18875802	44.7607366	-0.03827512	136.3820875
N2O				
Beaver River	0.200359261	0.031409635	0.176775201	0.243770475
Cawthra Mulock	0.044891646	0.064573413	-0.041962431	0.132478235
Circle Park	-0.014932918	0.030819979	-0.059951838	0.025420554
July				
CO2				
Beaver River	485.687867	224.727377	266.2096821	741.4042669
Cawthra Mulock	891.1300826	570.6057659	97.83462223	1647.3571
Circle Park	787.2549286	351.754947	123.1212852	1406.775518
CH4				
Beaver River	8.958169891	9.003629017	1.912098089	22.02854154
Cawthra Mulock	4.972058022	7.070478108	0.251645643	22.32384065
Circle Park	47.63563777	52.90467232	7.683731964	151.2069027
N2O				
Beaver River	-0.015201652	0.013307917	-0.02719945	0.00135121
Cawthra Mulock	0.007686786	0.037218483	-0.062506647	0.084321404
Circle Park	-0.046336855	0.095599358	-0.278876941	0.022782309
October				
CO2				
Beaver River	415.8713593	414.3976663	151.2496594	1033.785542
Cawthra Mulock	160.999214	79.31096044	-10.64930312	285.7484655
Circle Park	275.1758063	212.6346074	34.69328088	654.0470803
CH4				
Beaver River	10.99876232	18.32686413	-1.65612801	38.07869844
Cawthra Mulock	-0.271843273	0.567655434	-1.657976475	0.568410436
Circle Park	43.99882537	114.6457718	0.94640335	349.430804
N2O				
Beaver River	0.112028528	0.124333679	0.018141162	0.281239633
Cawthra Mulock	-0.093731084	0.183403116	-0.398502773	0.254748036
Circle Park	-0.011115197	0.0568892	-0.094832785	0.094668065
2025				
February				
CO2				
Beaver River	8.314216675	18.94322006	-9.804127644	34.83239186

Cawthra Mulock	22.08289611	41.89918261	-7.361965406	139.0820543
Circle Park	64.56753719	75.04114259	11.31084865	236.8610309

CH4

Beaver River	0.167179869	0.144917425	0.042033308	0.358086287
Cawthra Mulock	-0.02037802	0.030270072	-0.075758625	0.012162054
Circle Park	3.724647998	4.637906922	0.738218314	15.10334505

N2O

Beaver River	-0.040445648	0.090340149	-0.175948905	0.005952898
Cawthra Mulock	-0.009105656	0.023018543	-0.07375234	0.006993429
Circle Park	-0.000872355	0.008152224	-0.019545068	0.007502244

April

CO2

Beaver River	125.9481675	59.58840389	44.42249193	184.5245439
Cawthra Mulock	56.6344612	29.06907318	21.5831872	112.3793589
Circle Park	111.224887	90.57815831	24.52337924	324.3982515

CH4

Beaver River	0.555659652	0.610035655	0.109266049	1.41796987
Cawthra Mulock	0.007027053	0.093199933	-0.146008716	0.18489116
Circle Park	-37.13238314	158.7635438	-450.1085504	103.8281891

N2O

Beaver River	0.023414713	0.04408868	-0.029456051	0.076733814
Cawthra Mulock	0.009355693	0.041003616	-0.038260651	0.10704395
Circle Park	-0.027983983	0.084162607	-0.205118608	0.068391303

May

CO2

Beaver River	154.3062491	219.445608	-149.9823708	324.1967635
Cawthra Mulock	153.0045167	47.95809538	82.34477374	241.0311285
Circle Park	226.1426199	132.9104256	44.8612854	452.7470929

CH4

Beaver River	1.250445879	1.668014494	-0.364305035	3.563247905
Cawthra Mulock	1.340803127	1.185948826	0.268386501	4.16401187
Circle Park	14.17488559	11.22292385	4.207770736	33.88760683

N2O

Beaver River	-0.22319485	0.549785501	-1.039197839	0.158529728
Cawthra Mulock	0.075870116	0.226821618	-0.170606379	0.556151217
Circle Park	-0.023241096	0.053088183	-0.140415121	0.031475417

June

CO2

Beaver River	482.4443295	205.1190349	237.9512048	697.447529

Cawthra Mulock	317.2140265	244.3164571	-180.4897946	614.349268
Circle Park	1173.928109	1271.934068	-27.08263141	3799.903183

CH4

Beaver River	6.990380375	10.12884863	-1.394328379	21.70869922
Cawthra Mulock	7.500135844	13.5917819	0.169699158	47.77180247
Circle Park	135.5833588	139.206074	-11.96655464	358.7320276

N2O

Beaver River	-0.141464666	0.249468431	-0.515343468	-0.005054123
Cawthra Mulock	0.104463298	0.434175366	-0.195618037	1.401242964
Circle Park	-0.000628115	0.051784577	-0.068809659	0.121097063

July

CO2

Beaver River	826.3457249	375.506357	336.2627302	1249.23904
Cawthra Mulock	951.6818591	453.3711904	442.3111052	1761.68355
Circle Park	710.5596497	280.9310346	325.0555806	1252.760852

CH4

Beaver River	2.145710405	3.223528745	0.256355008	6.960035389
Cawthra Mulock	0.05729788	0.14121158	-0.275140625	0.264177365
Circle Park	140.6696283	174.9115429	2.381234026	486.2004874

N2O

Beaver River	-0.002443541	0.053227183	-0.069235281	0.05944445
Cawthra Mulock	0.051483635	0.17633	-0.038539445	0.577335389
Circle Park	-0.073405099	0.192282549	-0.580432336	0.044945652

August

CO2

Beaver River	1141.079009	990.9855712	407.1867331	2604.443056
Cawthra Mulock	664.4737745	251.5467453	395.7760532	1251.525582
Circle Park	377.5557159	219.9715048	134.269971	710.3690406

CH4

Beaver River	0.613982665	0.435372242	0.036510025	1.00791394
Cawthra Mulock	0.042601486	0.197385727	-0.398081435	0.268447106
Circle Park	100.0869551	198.2004548	-33.18416769	567.9456716

N2O

Beaver River	-0.01019603	0.016886308	-0.033976267	0.004770561
Cawthra Mulock	0.010716939	0.030476584	-0.057191089	0.048048423
Circle Park	0.006228188	0.022404284	-0.039979683	0.030202288

September

CO2

Beaver River	203.216259	114.600547	89.52236507	357.1870341

Cawthra Mulock	412.5657364	91.51242543	330.9591313	605.8839926
Circle Park	377.6006655	158.3453558	197.3889997	692.5632576
CH4				
Beaver River	-0.6235411	2.58530751	-4.495352148	0.872723953
Cawthra Mulock	0.074074827	0.195150594	-0.196861211	0.350888023
Circle Park	56.95630046	84.53896117	-41.41355986	201.8794789
N2O				
Beaver River	0.019376421	0.012172832	0.007740812	0.029933915
Cawthra Mulock	0.007458667	0.021555839	-0.029085565	0.039470131
Circle Park	0.000537578	0.009787248	-0.018162121	0.013020741
October				
CO2				
Beaver River	124.8777552	29.78299002	102.6622469	166.1230261
Cawthra Mulock	270.6320625	134.8119474	62.10419364	577.8631926
Circle Park	261.1466321	109.9995752	83.05662813	423.9273681
CH4				
Beaver River	0.858384891	0.513360715	0.269104263	1.35219225
Cawthra Mulock	-0.049727413	0.108478098	-0.198930151	0.194581072
Circle Park	146.2039329	374.7161387	-60.94541844	1132.995058
N2O				
Beaver River	-0.000378257	0.006374699	-0.006878334	0.005096146
Cawthra Mulock	0.036460767	0.14761591	-0.030545128	0.479536089
Circle Park	-0.025768236	0.075963799	-0.224830258	0.015079472

Appendix 3 Diurnal flux means and SD for CO_2, CH_4, and N_2O

Time/Gas	Circle Park (mg m^{-2} h^{-1})	Cawthra Mulock (mg m^{-2} h^{-1})	Beaver River (mg m^{-2} h^{-1})
8:00 CO_2 flux	707 ± 402	480 ± 273	464 ± 594
16:00 CO_2 flux	683 ± 216	761 ± 221	826 ± 376
00:00 CO_2 flux	1149 ± 787	817 ± 269	1101 ± 668
8:00 CH_4 flux	156 ± 315	-0.04 ± 0.41	-2.02 ± 4.96
16:00 CH_4 flux	158 ± 225	0.03 ± 0.08	2.15 ± 3.22
00:00 CH_4 flux	48.9 ± 59.3	-0.02 ± 0.18	0.84 ± 0.38
8:00 N_2O flux	-0.05 ± 0.09	0.02 ± 0.06	-0.05 ± 0.08
16:00 N_2O flux	-0.02 ± 0.03	0.15 ± 0.29	0.00 ± 0.05
00:00 N_2O flux	-0.02 ± 0.01	0.34 ± 0.60	0.05 ± 0.11

Appendix 4 Protist Assemblage Counts

Species	CP1	CP2	CP3	CP4	CP5	CP6	CP7	CP8	CP9	CM1	CM2	CM3	CM4	CM5	CM6	CM7	CM8	CM9	CM10	CM11	BRW1	BRW2	BRW3	BRW4
Trinema sp. type	75	57	120	86	94	27	70	45	25	3	23	9	4	51	33	29	4	10	5	8	12	20	19	40
Ditrema mikrous	13	8	19	39	0	0	2	5	0	0	0	0	0	0	0	0	0	0	0	0	0	0	0	0
Trigonopyxis arcula	5	7	0	0	0	1	0	0	0	0	0	0	0	0	0	0	0	0	0	0	0	0	0	0
Euglypha tuberculata	3	4	0	0	3	15	4	2	2	0	2	0	0	2	0	0	6	12	31	19	14	20	7	6
Cyclopyxis platystoma	3	3	0	0	0	6	0	0	1	2	0	1	1	0	0	0	0	0	0	0	7	3	5	0
Centropyxis aculeata	1	4	1	0	0	20	9	10	5	0	3	5	10	2	0	3	8	4	5	7	13	1	3	9
Cylindrifflugia acuminata	1	0	0	0	0	0	0	0	0	0	1	0	0	0	0	0	0	0	0	0	0	0	0	0
Difflugia fusiforma	14	5	5	0	12	0	0	1	0	0	0	0	0	0	0	0	0	0	0	0	0	2	0	0
Cyclopyxis arcelloides	26	19	0	0	4	2	4	8	6	6	12	16	4	7	10	9	6	10	7	8	7	1	2	3
Hyalosphenia minuta	3	0	0	0	0	0	0	0	0	0	0	0	0	0	0	0	0	0	0	0	0	0	0	0
Euglypha capsiosa	5	4	0	1	0	1	0	0	0	0	0	0	0	0	0	0	0	0	0	0	0	0	0	0
Nebela vitraeae	1	4	0	1	0	2	0	0	0	4	0	2	0	0	0	0	0	0	0	0	0	1	0	0
Arcella discoides type	0	3	0	4	1	2	4	0	4	0	0	0	0	0	0	0	0	0	0	0	1	0	0	0
Lecythium spp.	0	23	3	12	6	1	5	5	0	0	0	0	0	0	0	0	0	0	0	0	0	5	2	0
Euglypha acanthophora	0	0	0	0	0	0	2	0	0	0	0	0	0	0	0	0	0	0	0	0	0	0	0	0
Difflugia acuminate	0	2	0	0	0	0	0	0	0	0	0	0	0	0	0	0	0	0	0	0	0	0	0	0
Arcella hemisphaerica	0	2	0	0	2	6	1	0	2	0	0	0	0	0	4	2	0	0	0	0	0	0	0	0
Difflugia perfilievi	0	1	0	0	0	0	0	0	0	0	0	0	0	0	0	0	0	0	0	0	0	0	0	0
Difflugia umbilicate	0	2	0	1	0	0	0	0	4	2	0	0	0	0	0	0	0	0	0	0	1	0	0	0
Golemanskia viscidula	0	4	0	2	5	4	0	0	6	5	9	8	1	0	0	0	0	0	1	0	0	0	0	1

Difflugia bipartis	0	2	1	0	1	1	0	0	0	0	1	0	0	0	0	0	0	0	0	0	0	0	0	0	0
Arcella artocrea	0	0	1	5	0	0	3	6	0	0	0	0	0	0	0	0	0	0	0	0	1	3	2	0	
Paraquadrula irregularis	0	0	0	0	0	2	0	1	2	10	2	3	25	7	8	15	10	18	7	11	23	16	2	2	
Centropyxis cryptostoma	0	0	0	1	0	3	0	0	1	2	0	2	0	0	0	0	0	0	0	0	0	0	0	0	
Plagiopyxis declivis	0	0	1	0	3	9	0	0	4	2	1	3	1	4	10	7	0	4	2	6	1	2	0	0	
Difflugia difficilis ecornis	0	0	0	0	3	8	0	0	3	9	4	5	4	1	4	3	0	3	4	2	0	0	0	1	
Centropyxis platystoma	0	0	0	0	8	21	1	4	15	20	6	28	14	11	7	8	2	5	2	0	0	2	1	1	
Difflugia pulex	0	0	0	0	10	3	0	0	0	1	0	0	0	0	0	0	4	0	0	2	1	0	2	1	
Centropyxis cassis	0	0	0	0	0	5	1	0	13	1	4	1	6	7	8	11	14	12	7	4	10	9	13	2	
Difflugia fallax	0	0	0	0	0	6	0	1	2	6	6	0	8	3	5	5	11	8	6	11	0	0	0	0	
Phryganella acropodia	0	0	0	0	2	5	1	5	3	8	9	2	10	2	6	4	7	2	4	9	21	7	10	5	
Centropyxis ecornis	0	0	0	0	0	0	1	0	0	0	0	2	0	0	0	0	0	0	0	0	1	0	1	0	
Cylindrifflugia elegans	0	0	0	0	0	0	1	0	0	0	0	1	1	0	0	0	1	1	0	0	0	0	0	0	
Netzelia gramen	0	0	0	0	0	0	1	0	3	0	0	1	0	0	1	2	0	0	0	0	0	0	0	0	
Cryptodifflugia sacculus	0	0	0	0	0	0	0	3	0	0	0	0	0	0	0	0	0	0	0	0	2	2	3	0	
Difflugia decloitrei	0	0	0	0	0	0	0	6	0	9	6	10	0	4	8	6	16	9	12	5	0	0	0	1	
Cyphoderia ampulla	0	0	0	0	0	0	0	0	0	0	0	0	0	0	0	0	0	0	0	0	27	0	7	11	
Nebela collaris	0	0	0	0	0	0	0	0	0	0	0	2	0	0	0	0	0	0	0	0	3	0	0	0	
Euglypha rotunda	0	0	0	0	0	0	0	0	0	0	0	0	0	0	0	0	0	0	0	0	8	3	8	2	
Difflugia glans	0	0	0	0	0	0	0	0	0	5	2	2	7	0	4	3	9	4	2	5	4	7	2	2	
Hyalospenia elegans	0	0	0	0	0	0	0	0	0	0	0	0	0	0	0	0	0	0	0	0	2	1	0	1	
Padaungiella lageniformis	0	0	0	0	0	0	0	0	0	0	0	0	0	0	0	0	0	0	0	0	1	0	0	0	
Galeripora catinus	0	0	0	0	0	0	0	0	0	0	0	0	0	0	0	0	0	0	0	0	2	0	0	0	
Phryganella nidulus	0	0	0	0	0	0	0	0	0	1	0	0	0	0	0	0	0	0	0	0	1	0	0	0	

Centropyxis discoides	0	0	0	0	0	0	0	0	0	0	0	0	0	0	0	0	0	0	0	0	1	0	1	3
Centropyxis constricta	0	0	0	0	0	0	0	0	0	2	2	0	2	0	0	0	1	3	3	2	0	11	7	2
Euglypha spinosa	0	0	0	0	0	0	0	0	0	1	0	0	0	0	0	0	0	0	2	1	0	1	2	11
Plagiopyxis labiata	0	0	0	0	0	0	0	0	0	0	2	0	1	0	0	0	0	0	0	0	0	0	2	0
Centropyxis notonyx	0	0	0	0	0	0	0	0	0	5	4	0	0	0	0	0	2	0	1	3	0	0	0	0
Cyclopyxis thomasi	0	0	0	0	0	0	0	0	0	0	2	0	3	0	0	0	0	0	0	0	0	0	0	0

Appendix 5 Phototrophic Assemblage Counts

Species	CP 1	CP 2	CP 3	CP 4	CP 5	CP 6	CP 7	CP 8	CP 9	CM 1	CM 2	CM 3	CM 4	CM 5	CM 6	CM 7	CM 8	CM 9	CM 10	CM 11	BR W1	BR W2	BR W3	BR W4
Fungi	31	32	12	23	15	67	51	24	21	0	0	3	1	3	2	7	15	2	5	3	71	33	20	37
Diatoms	127	204	111	64	89	88	287	48	45	60	122	260	150	14	30	64	56	83	179	69	144	133	14	202
Phacus sp.	3	0	0	0	1	0	4	0	0	0	0	0	0	0	0	0	0	0	0	0	0	0	0	0
Cosmarium sp.	3	0	3	1	0	10	44	4	0	7	12	19	16	2	7	7	5	7	6	7	28	7	7	5
Scenedesmus sp.	5	0	0	0	0	0	0	0	0	0	0	0	0	0	0	0	0	0	0	0	0	0	0	0
Closterium sp.	1	2	0	0	0	0	0	0	0	0	0	0	0	0	0	0	0	0	0	0	0	0	0	0
Mesotaeniaceae type	0	191	64	55	0	7	9	2	0	11	3	50	15	2	3	7	46	21	43	8	0	0	0	0
Anthrospira spp.	0	2	0	0	6	2	13	1	0	0	1	0	0	1	0	0	1	0	0	0	0	0	0	0
Centitractus spp.	0	2	0	0	0	0	0	0	0	0	0	0	0	0	0	0	0	0	0	0	0	0	0	0
Desmidium spp.	0	2	0	0	0	1	0	0	0	0	0	0	0	0	0	0	0	0	0	0	0	0	0	0
Ankistrodesmus spp.	0	1	0	0	1	1	0	0	1	0	0	0	0	0	0	0	0	0	0	0	0	0	0	0
Staurastrum spp.	0	1	0	0	0	1	1	0	0	2	1	5	4	7	4	8	3	4	4	5	3	0	0	2
Snowella litoralis	0	0	0	0	6	1	0	0	0	0	0	0	0	0	0	0	0	0	0	0	0	0	0	0
Fragilaria spp.	0	0	0	0	0	1	1	0	0	0	0	0	0	0	0	0	0	0	0	0	0	0	0	0
Gymnodinium	0	0	0	0	0	21	4	0	0	0	0	0	0	0	0	0	0	0	0	0	0	0	0	0
Oocystis spp.	0	0	0	0	0	6	5	0	0	0	1	1	1	0	0	0	2	0	0	0	16	0	0	0
Gonatozygon spp.	0	0	1	0	0	1	2	0	0	0	0	0	0	0	0	0	0	0	0	0	0	0	0	0
Trochiscia reticularis	0	0	1	0	0	80	19	0	0	0	0	1	0	4	0	0	1	3	4	6	0	1	0	1
Pediastrum	0	0	0	0	0	0	1	1	1	17	2	5	1	0	0	0	1	0	0	0	4	0	0	1
Nostoc sp.	0	0	0	0	0	0	0	0	0	0	1	0	0	0	0	0	0	0	0	0	51	0	0	0
Microspora sp.	0	0	0	0	0	0	0	0	0	0	0	0	0	0	0	0	157	9	17	5	0	0	0	0

Tribonema sp.	0	0	0	0	0	0	0	0	0	0	0	0	0	0	0	0	32	15	4	8	0	0	0	0

Appendix 6 CO_2-equivalent — SGWP100 — Prime (CO_2 $R^2 \geq 0.7$)

SGWP100: CO_2=1, CH_4=45, N_2O=270 (Neubauer & Megonigal 2015, corrected 2019)

Median hourly flux (mg CO_2-eq m^{-2} h^{-1})								
Site	**Year**	**CO_2 component**	**CH_4 component**	**N_2O component**	**Total CO_2-eq**	**Q25 Total**	**Q75 Total**	**n chambers (per gas)**
Circle Park	2023	719.57	619.83	-1.93	1337.47	658.91	2016.03	17
Circle Park	2024	307.73	762.84	0.57	1065.6	357.13	1779.6	22
Circle Park	2025	373.02	1432.83	-0.7	943.75	340.58	2197.48	66
Cawthra Mulock	2023	378.52	59.38	-1.64	436.26	193.32	679.2	21
Cawthra Mulock	2024	377.22	45.39	5.43	248.22	152.04	524.23	28
Cawthra Mulock	2025	335.1	33.66	0.69	313	149.21	609.86	72
Beaver River	2023	471.68	413.72	-10.27	875.14	236.6	1513.67	8
Beaver River	2024	368.03	122.81	28.37	462.28	364.92	730.42	10
Beaver River	2025	410.64	52.73	1.16	362.03	186.59	734.83	27

2025 Time-weighted annual total								
Site	**Year**	**CO_2 (g CO_2-eq/m²/yr)**	**CH_4 (g CO_2-eq/m²/yr)**	**N_2O (g CO_2-eq/m²/yr)**	**Total (g CO_2-eq/m²/yr)**	**Q25 Total (g CO_2-eq/m²/yr)**	**Q75 Total (g CO_2-eq/m²/yr)**	**n chambers (per gas)**
Circle Park	2025	2484.51	9156.5	-2.06	11638.96	2922.69	26190.47	66
Cawthra Mulock	2025	2226.92	194.31	5.97	2427.2	1894.09	3347.46	72
Beaver River	2025	2202.03	298.88	5.94	2506.85	1864.66	3466.35	27

Appendix 7 CO_2-equivalent — SGWP100 — All Decent (CO_2 $R^2 \geq 0.3$)

SGWP100: CO_2=1, CH_4=45, N_2O=270 (Neubauer & Megonigal 2015, corrected 2019)

Median hourly flux (mg CO_2-eq m^{-2} h^{-1})								
Site	**Year**	**CO_2 component**	**CH_4 component**	**N_2O component**	**Total CO_2-eq**	**Q25 Total**	**Q75 Total**	**n chambers (per gas)**
Circle Park	2023	706.88	595.94	-1.86	1300.96	585.88	2016.03	18
Circle Park	2024	281.63	520.77	-1	546.28	347.05	1000.62	28
Circle Park	2025	372.51	1433.64	-1.03	943.75	340.91	2197.48	68
Cawthra Mulock	2023	359.81	59.76	-1.53	418.04	156.88	679.2	22
Cawthra Mulock	2024	379.7	42.65	5.19	250.54	128.03	550.06	35
Cawthra Mulock	2025	329.53	30.03	0.62	303.11	153.36	576.25	80
Beaver River	2023	471.68	413.72	-10.27	875.14	236.6	1513.67	8
Beaver River	2024	268.29	120.06	15.81	452.49	316.58	540.07	15
Beaver River	2025	398.69	50.48	0.33	256.88	186.59	734.83	28

2025 Time-weighted annual total

Site	Year	CO_2 (g CO_2-eq/m²/yr)	CH_4 (g CO_2-eq/m²/yr)	N_2O (g CO_2-eq/m²/yr)	Total (g CO_2-eq/m²/yr)	Q25 Total (g CO_2-eq/m²/yr)	Q75 Total (g CO_2-eq/m²/yr)	n chambers (per gas)
Circle Park	2025	2473.19	9174.01	-4.71	11642.49	2964.24	26029.41	68
Cawthra Mulock	2025	2170.73	171.86	4.1	2346.69	1725.88	3088.62	80
Beaver River	2025	2139.82	287.16	1.64	2428.62	1682.15	3435.6	28

Appendix 8 CO_2-equivalent — SGWP100 — All Decent + Dormant ($R^2 \geq 0.3$, plus all Feb/Apr)

SGWP100: CO_2=1, CH_4=45, N_2O=270 (Neubauer & Megonigal 2015, corrected 2019)

Median hourly flux (mg CO_2-eq m^{-2} h^{-1})								
Site	**Year**	**CO_2 component**	**CH_4 component**	**N_2O component**	**Total CO_2-eq**	**Q25 Total**	**Q75 Total**	**n chambers (per gas)**
Circle Park	2023	706.88	595.94	-1.86	1300.96	585.88	2016.03	18
Circle Park	2024	266.98	485.68	-1.13	470.16	335.24	886.44	35
Circle Park	2025	371.39	1432.1	-0.77	943.75	340.44	2197.48	71
Cawthra Mulock	2023	359.81	59.76	-1.53	418.04	156.88	679.2	22
Cawthra Mulock	2024	337.84	33.21	3.23	179.22	110.42	443.08	43
Cawthra Mulock	2025	328.29	29.96	0.56	303.11	153.36	576.25	86
Beaver River	2023	471.68	413.72	-10.27	875.14	236.6	1513.67	8
Beaver River	2024	273.92	119.35	16.4	452.49	322.08	540.07	16
Beaver River	2025	349.44	45.15	0.47	235.36	158.54	698.97	32

2025 Time-weighted annual total								
Site	**Year**	**CO_2 (g CO_2-eq/m²/yr)**	**CH_4 (g CO_2-eq/m²/yr)**	**N_2O (g CO_2-eq/m²/yr)**	**Total (g CO_2-eq/m²/yr)**	**Q25 Total (g CO_2-eq/m²/yr)**	**Q75 Total (g CO_2-eq/m²/yr)**	**n chambers (per gas)**
Circle Park	2025	2447.84	9139.41	-3.66	11583.6	2788.07	25671.06	71
Cawthra Mulock	2025	2142.03	170.28	2.84	2315.16	1626.77	3071.57	86
Beaver River	2025	2153.35	309.78	5.75	2468.88	1670.49	3493.38	32